

# **BAND GAP ENGINEERING AND CARRIER TRANSPORT IN $\text{TiO}_2$ FOR SOLAR ENERGY HARVESTING**

by

Mengjin Yang

ME, Tsinghua University, China, 2008

BE, Chongqing University, China, 2005

Submitted to the Graduate Faculty of  
the Swanson School of Engineering in partial fulfillment  
of the requirements for the degree of  
Doctor of Philosophy

University of Pittsburgh

2012

UNIVERSITY OF PITTSBURGH  
SWANSON SCHOOL OF ENGINEERING

This dissertation was presented

by

Mengjin Yang

It was defended on

March 20th, 2012

and approved by

Jung-Kun Lee, Ph.D., Assistant Professor, Department of Mechanical Engineering and Materials  
Science

David Waldeck, Ph.D., Professor, Department of Chemistry

John A. Barnard, Ph.D., Professor, Department of Mechanical Engineering and Materials Science

Ian Nettleship, Ph.D., Associate Professor, Department of Mechanical Engineering and Materials  
Science

Dissertation Director: Jung-Kun Lee, Ph.D., Assistant Professor,  
Department of Mechanical Engineering and Materials Science

Copyright © by Mengjin Yang

2012

# **BAND GAP ENGINEERING AND CARRIER TRANSPORT IN TiO<sub>2</sub> FOR SOLAR ENERGY HARVESTING**

Mengjin Yang, Ph.D.

University of Pittsburgh, 2012

TiO<sub>2</sub> has been used in photocatalysis and photovoltaics because of its comprehensive combination of energy band structure, carrier transport, and inertness. However, wide band gap and relative slow carrier transport limit its full potential in these applications. 3.2 eV band gap of anatase indicates its low efficiency of utilizing full spectrum of solar light, and, band gap engineering was employed to address this issue. Specifically, nitrogen doping, iron doping, and N/Fe codoping were investigated for their photocatalytic effect. Doping was carried out in hydrothermal reactor by adding aliovalent ions to TiO<sub>2</sub> precursor. Both N and Fe doping show the narrowing of band gap compared with the pristine TiO<sub>2</sub>. N-doping enhances its visible light photocatalytic performance, while Fe-doping and codoping result in a poor photocatalysis. Further low temperature fluorescence spectra indicate the high recombination in Fe-doped and co-doped samples. The next issue is the relatively slow carrier transport in TiO<sub>2</sub> nanoparticle-based dye sensitized solar cell (DSSC). Single crystalline rutile nanorod was studied in order to overcome this drawback. Synthesis was achieved with the assistance of microwave heating, and reaction rate was boosted due to this unique heating method. The carrier diffusion coefficient and lifetime of TiCl<sub>4</sub> treated nanorods were systematically measured, and surface diffusion model is proposed to interpret observed phenomena. Combining band gap engineering (doping) and carrier transport (nanorod) research, doped nanorods were investigated. It is found that Nb doped nanorods show a higher conductivity, a better back contact between FTO and nanorod, an easy

injection of electron from dye sensitizers to nanorods, and, consequently, a less recombination. The efficiency of solar cell from Nb doped nanorods increases by almost 80% comparing with pure nanorods. What's more, the conductive-AFM with nanoscale resolution provides an unprecedented image of current path in nanorod, which could verify carrier transport model and shed light on the engineering of nanostructure for a superior performance.

## TABLE OF CONTENTS

<b>PREFACE.....</b>	<b>XV</b>
<b>1.0 INTRODUCTION.....</b>	<b>1</b>
<b>1.1 TiO<sub>2</sub> POLYMORPHS.....</b>	<b>1</b>
<b>1.2 APPLICATIONS .....</b>	<b>4</b>
<b>1.2.1 Photocatalysis.....</b>	<b>4</b>
<b>1.2.2 Dye sensitized solar cell.....</b>	<b>9</b>
<b>1.2.3 Other applications .....</b>	<b>12</b>
<b>1.2.3.1 Lithium ion battery .....</b>	<b>12</b>
<b>1.2.3.2 Dilute magnetic semiconductor oxide .....</b>	<b>13</b>
<b>1.2.3.3 Memristor .....</b>	<b>14</b>
<b>1.3 CHALLENGES OF TiO<sub>2</sub> FOR ADVANCED APPLICATIONS.....</b>	<b>15</b>
<b>2.0 BAND GAP ENGINEERING OF TiO<sub>2</sub>.....</b>	<b>19</b>
<b>2.1 BACKGROUND AND APPROACH.....</b>	<b>19</b>
<b>2.1.1 Motivation .....</b>	<b>19</b>
<b>2.1.2 Fluorescence spectroscopy .....</b>	<b>21</b>
<b>2.1.3 X-ray Photoelectron spectroscopy (XPS) .....</b>	<b>24</b>
<b>2.2 DOPING EFFECTS OF NITROGEN, IRON, AND N/FE CODOPING.....</b>	<b>27</b>
<b>2.2.1 Sample preparation .....</b>	<b>27</b>

2.2.2	Characterization and measurement.....	28
2.2.3	Results and discussion.....	29
3.0	CARRIER TRANSPORT MANIPULATION .....	39
3.1	BACKGROUND .....	39
3.1.1	Motivation of 1-D nanostructure for photoanode .....	39
3.1.2	Carrier transport model in DSSC .....	42
3.1.3	SLIM-PCV method.....	47
3.2	SINGLE CRYSTALLINE RUTILE NANOROD ON FTO .....	50
3.2.1	Experiment .....	50
3.2.2	Synthesis of rutile nanorod on FTO.....	52
3.2.3	Carrier transport in $TiCl_4$ treated nanorods .....	58
4.0	DOPING IN NANOROD.....	66
4.1	BACKGROUND .....	66
4.1.1	Metal-Semiconductor contact.....	68
4.1.2	Electrochemical Impedance Spectroscopy .....	76
4.1.3	Mott-Schottky Plot .....	83
4.2	NIBIUM DOPING IN NANORODS.....	86
4.2.1	Experiment .....	86
4.2.2	Results and Analysis.....	88
4.2.3	Charge transport observation in nanorod via c-AFM .....	103
4.3	NITROGEN DOPING IN NANOROD .....	106
4.3.1	Experiment .....	106
4.3.2	Results and Discussion .....	107

<b>5.0</b>	<b>CONCLUSIONS AND FUTURE WORK .....</b>	<b>110</b>
<b>5.1</b>	<b>CONCLUSIONS .....</b>	<b>110</b>
<b>5.2</b>	<b>FUTURE WORK.....</b>	<b>112</b>
	<b>BIBLIOGRAPHY .....</b>	<b>116</b>



## LIST OF TABLES

Table 2-1 The relation between quantum number and XPS, X-ray notation <sup>77</sup> .....	24
Table 3-1 Summary of charge transport measurement techniques for DSSCs.....	47
Table 4-1 Basic ac electrical elements.....	78

## LIST OF FIGURES

Figure 1-1 Unit cells of TiO <sub>2</sub> polymorphs (a) rutile, (b) anatase, (c) brookite .....	2
Figure 1-2 Octahedra stacking of (a) rutile, (b) anatase, (c) brookite; (d) octahedral filament along [001] direction for rutile .....	3
Figure 1-3 Simplified diagram of heterogeneous photocatalytic process.....	5
Figure 1-4 Mechanism of TiO <sub>2</sub> photocatalytic water splitting for hydrogen production <sup>9</sup> .....	6
Figure 1-5 Band gap alignment of various semiconductor <sup>12,13</sup> .....	8
Figure 1-6 Schematics of dye-sensitized solar cell.....	10
Figure 1-7 (a) Memresistor configuration, (b) characteristic current voltage curve, (c) actual measured IV curve, (d) AFM diagram of a circuit with 17 memristors <sup>41</sup> .....	14
Figure 1-8 Solar light spectrum .....	16
Figure 1-9 Dynamics time scale in Dye-Sensitized Solar Cell <sup>31</sup> .....	17
Figure 2-1 Schematics of band gap alternations: a) pristine TiO <sub>2</sub> ; b) and c) phase mixing to lift VB or lower CB; d) creation of discrete band in band gap; e) discrete doping level; f) surface doping. <sup>45</sup> .....	20
Figure 2-2 Jablonski diagram for fluorescence, S <sub>0</sub> is ground state, S <sub>1</sub> and S <sub>2</sub> are excited singlet states, and T <sub>1</sub> is triplet state <sup>75</sup> .....	22
Figure 2-3 Absorption and emission spectra of anthracene, and its mirror-image can be interpreted as similar spacings of vibrational levels <sup>75</sup> .....	23
Figure 2-4 Schematics of XPS process of 1s signal (a) and the correlation between XPS spectra and energy orbitals (b) <sup>77</sup> .....	25
Figure 2-5 Effect of chemical state on XPS spectra, Fe 2p <sub>3/2</sub> and its satellite line shift at different chemical states (Fe <sup>2+</sup> , Fe <sup>3+</sup> ) <sup>78</sup> .....	26

Figure 2-6 (a) XRD pattern of doped TiO <sub>2</sub> (b) Raman spectra of doped TiO <sub>2</sub> , both show anatase phase for synthesized nanoparticles .....	29
Figure 2-7 TEM micrographs of (a) pure TiO <sub>2</sub> (b) Fe-doped TiO <sub>2</sub> (c) N-doped TiO <sub>2</sub> and (d) N/Fe-codoped TiO <sub>2</sub> .....	30
Figure 2-8 Absorption spectra of pure and doped TiO <sub>2</sub> .....	31
Figure 2-9 Relative concentration of Rh. B as a function of illumination time; (a) under UV light, (b) under simulated solar light (an inset shows a gradual change in absorption spectra of N-doped sample).....	32
Figure 2-10 TA fluorescence probe test; (a) luminescence spectra of TiO <sub>2</sub> dispersed TA solution under UV light, (b) change in the luminescence intensity of the solutions dispersed with four types of TiO <sub>2</sub> under UV light, (c) change in the luminescence intensity of the solutions dispersed with pure and N-doped TiO <sub>2</sub> under simulated solar light. ....	33
Figure 2-11 XPS spectra of N1s (a) and Fe2p (b) .....	35
Figure 2-12 Photoluminescence spectra of pure, N-doped, Fe-doped, and N/Fe codoped TiO <sub>2</sub> at 10K .....	37
Figure 3-1 Density of state function vs energy below conduction band.....	44
Figure 3-2 Schematics of multiple-trapping model .....	45
Figure 3-3 Schematics of hopping model .....	46
Figure 3-4 Configuration of SLIM-PCV measurement.....	48
Figure 3-5 Measurement of current (a) and voltage (b) transition under a small drop of light intensity .....	49
Figure 3-6 XRD diagram of TiO <sub>2</sub> nanorod on FTO substrate .....	52
Figure 3-7 TEM image of TiO <sub>2</sub> nanorod in a bright field mode; an inset shows the selected area diffraction pattern of the nanorod. ....	53
Figure 3-8 SEM image of TiO <sub>2</sub> nanorod at different reaction time (10 min, 30 min, 50 min, 100 min).....	54
Figure 3-9 Growth rate of TiO <sub>2</sub> nanorods during a microwave assisted hydrothermal reaction; an inset indicates the growth rate of a conventional hydrothermal reaction in literature. ....	54
Figure 3-10 XRD patterns of TiO <sub>2</sub> nanorod grown at 195°C for different reaction times (10 min, 30 min, 50 min, and 100 min) .....	55
Figure 3-11 SEM images of TiO <sub>2</sub> nanorod grown at different temperatures (155°C, 175°C, and 195°C) for 50 min.....	56

Figure 3-12 AFM images of (a) bare FTO and (b) TiO <sub>2</sub> polymeric sol coated FTO; the amplitude error images of (c) bare FTO and (d) TiO <sub>2</sub> polymeric sol coated FTO during AFM measurement.....	57
Figure 3-13 SEM images of the nanorods grown (a) on pure FTO and (b) on TiO <sub>2</sub> polymeric sol coated FTO.....	58
Figure 3-14 Performance of DSSCs using bare TiO <sub>2</sub> nanorods and TiO <sub>2</sub> nanorods treated with TiCl <sub>4</sub> solution for different times; (a) J-V curves and (b) IPCE spectra.....	59
Figure 3-15 Absorption spectra of dyes desorbed from DSSCs using bare, 30 min-TiCl <sub>4</sub> treated, and 120 min-TiCl <sub>4</sub> treated nanorods.....	61
Figure 3-16 (a) Diffusion coefficient and (b) lifetime of DSSCs employing bare nanorods, 30 min-TiCl <sub>4</sub> treated nanorods, 120 min-TiCl <sub>4</sub> treated nanorods, and rutile nanoparticles grown from TiCl <sub>4</sub> solution.....	62
Figure 3-17 Life time of DSSCs using bare nanorods and nanorod with a 3-nm thick passivation layer deposited by an ALD method.....	63
Figure 3-18 Raman spectra of nanorod, rutile nanoparticle, and TiCl <sub>4</sub> treated nanorod.....	64
Figure 4-1 Three types of metal-semiconductor contact, (a) accumulated, (b) neutral, (c) depleted <sup>163</sup> .....	69
Figure 4-2 Image charge and electric field distribution(a) and energy-band diagram with the influence of image-force (b) <sup>164</sup> .....	70
Figure 4-3 Detailed energy-band diagram of metal-n-semiconductor contact with a thin interfacial layer <sup>165</sup> .....	72
Figure 4-4 Electron transport at different doping level, (a) thermionic emission, (b) thermionic field emission, (c) field emission <sup>163</sup> .....	73
Figure 4-5 Typical I-V curve for a Schottky contact <sup>163</sup> .....	75
Figure 4-6 Derivation of series resistance in p-n junction using IdV/dI vs I plot <sup>167</sup> .....	75
Figure 4-7 Schematics of EIS measurement (a), a small amplitude sinusoidal oscillations with different frequencies are superimposed to a steady bias; DC solar cell equivalent circuit model (b), components of this model include current source, diode, shunt resistance, series resistance, and external load <sup>168</sup> .....	77
Figure 4-8 Equivalent circuit (a) and its corresponding spectroscopies, Z''-Z' Nyquist plot (b), Z'-frequency (c), and Phase-frequency Bode plot (d) <sup>168</sup> .....	79

Figure 4-9 Experimental EIS spectra of an ionic liquid DSSC (left) and simplified equivalent circuit model at different potential in the dark, (a) low potential; (b) intermediate potential; (c) high potential <sup>168</sup> .....	82
Figure 4-10 Band diagram of n-type semiconductor and electrolyte before contact (a), after contact (b), and at its flat band potential $V_{fb}$ <sup>169</sup> .....	84
Figure 4-11 Mott-Schottky plot of ZnO, slope and intercept can be used to determine donor concentration and flat band respectively <sup>169</sup> .....	85
Figure 4-12 Electrode capacity vs. log frequency plot, in 0.1 M NaCl electrolyte at two potential values, pH 4.7 and room temperature <sup>172</sup> .....	86
Figure 4-13 SEM morphology evolution at different Nb doping level .....	89
Figure 4-14 XRD pattern of Nb doped samples, rutile phase without Nb precipitate .....	90
Figure 4-15 UV-Visible spectroscopy measurement of dye-desorption for pure and doped nanorod.....	91
Figure 4-16 Current-voltage curves of Nb-doped nanorod.....	92
Figure 4-17 Mott-Schottky Plot of pure and Nb doped nanorod, showing a positive shift of flat band .....	93
Figure 4-18 Nyquist (a) and Bode Plot (b) of lightly doped nanorod, larger recombination resistance and longer lifetime after Nb doping .....	94
Figure 4-19 SLIM-PCV measurement, (a) diffusion coefficient, (b) lifetime.....	95
Figure 4-20 C-AFM measurement of Nb doped nanorod on top of FTO using boron-doped diamond probe (a) morphology and (b) current of pure nanorod, (c) morphology and (d) current of 0.25% Nb doped nanorod, current profiles of marked areas are illustrated in the insets (current signal has been multiplied by -1 so that larger the number indicates stronger current).....	97
Figure 4-21 C-AFM measurement of Nb doped nanorod on top of FTO, (a) schematics of measurement configuration; (b) I-V curve with Pt probe and Boron doped diamond probe; energy level alignment before contact (c) and after contact (d).....	98
Figure 4-22 I-V curve comparison of pure nanorod and Nb doped nanorod (a) and its repeatability test after 6 repeat cycles(b).....	100
Figure 4-23 Series resistance derivation (slope) of Nb doped nanorod (a) and I-V curve after subtracting series resistance (b).....	101
Figure 4-24 Proposed charge transport model in FTO and nanorod contact, thermoionic emission (a) and thermoionic field emission after Nb doping (b) .....	102

Figure 4-25 SEM microgram of 2% Nb doped nanorods, (a) top view; (b) cross-section view.	104
Figure 4-26 C-AFM measurement of 2% Nb doped nanorod after annealing at air (a), (b), $10^9$ gain; at forming gas (5% $H_2$ ) (c), (d), $10^6$ gain .....	105
Figure 4-27 Effect of temperature on DSSC performance after $NH_3$ post-treatment (a) I-V curve, (b) IPCE.....	107
Figure 4-28 Comparison between NR and N-doped NR in I-V curve and IPCE, the enhancement comes from increased absorption of nanorod as well as efficient electron injection .....	108
Figure 4-29 Absorption spectrum of N719 in acetonitrile solvent .....	109
Figure 5-1 Raman spectrum of anatase layer (~20nm) coated nanorod, and both rutile (marked in R) and anatase (marked in A) are observed .....	113
Figure 5-2 J-V curve and export power diagram of pure nanorod (with $TiCl_4$ treatment) based DSSC using high extinction dye C218.....	114

## PREFACE

This dissertation includes some contents published/submitted in peer reviewed journal papers, and a list of journal papers is as following:

Chap 1. J-K Lee, and M.J. Yang, Progress in light harvesting and charge injection of dye sensitized solar cell, Mater. Sci. & Eng. B, 176, 1142, 2011 (DOI: 10.1016/j.mseb.2011.06.018)

Chap 2. M.J. Yang, C. Hume, S.W. Lee, Y-H Son, and J-K Lee, Correlation between photocatalytic efficacy and electronic band structure in hydrothermally grown TiO<sub>2</sub> nanoparticles, J. Phys. Chem. C 114, 15292, 2010 (DOI: 10.1021/jp103764n)

Chap 3. M.J. Yang, B. Ding, S.W. Lee, and J-K Lee, Carrier transport in dye sensitized solar cells using single crystalline TiO<sub>2</sub> nanorod grown by a microwave assisted hydrothermal reaction, J. Phys. Chem. C, 115, 14534, 2011 (DOI: 10.1021/jp2025126)

Chap 4. M.J. Yang, B. Ding, and J-K Lee, Enhanced charge collection in Nb Doped nanorod for dye sensitized solar cell, submitted

During Ph.D period, lots of help and encouragement have been received. I would like to express my appreciation and acknowledgement during this wonderful journey.

First and foremost, I would like to thank my advisor Professor Jung-Kun Lee for his kind guidance during my Ph.D period. His diligent, passionate, critic-thinking, well-balanced style influences my research tremendously. I am impressed by his strong logic, breadth of knowledge, and creativity. Without his mentoring, it is impossible to finish my Ph.D study.

I would also like to take this opportunity to thank my other committee members, Professor David Waldeck, Professor John Barnard, Professor Ian Nettleship. Professor Waldeck has been very supportive for my research as well as my professional development. I have learned a lot from Professor Waldeck through the interaction with him and his vibrant research group. Professor Barnard is always very generous to provide valuable equipments (such as Veeco SPM system, drop shape analysis system, inkjet printer) for my research. The experience of these equipments benefits me greatly. Professor Nettleship provides me another perspective to look at my research, which leads to more profound investigation. He is also very kind to allow me to use his equipment.

I would like to acknowledge the fruitful collaboration and contributions from other great researchers: Dr. You-Hwan Son, Dr. Abhijit Roy, Sang Jae Chung, Dr. Fang-I Li, Dr. Andreas Kulovits, Dr. Long Li, Zhongfan Zhang, Dr. Gautam Reddy. With their assistance, research became much easier and more productive.

I am pleased to have great members in this dynamic group: Bo Ding, Youngsoo Jung, and Po-shun Huang. Here I would specially thank Bo for his great job on counter electrode preparation and other synergic work, which facilitate my research. Also I would like thank current/past undergraduate members in our group for their contribution to research, group culture, and diversity: Chad Hume, Travis Sefzik, Derrick AK, David Palm, and Eric Marksz.

Thanks should be extended to Materials Science Characterization Lab and nano-scale fabrication and characterization facility, and their helpful staffs: Albert Stewart, Cole Van Ormer, Dr. Shusheng Tan, and Mike McDonald.

I would like to thank great teachers I met during my Ph.D period. Thank you, Chris Ortiz, Bob, Janine Carlock, Prof. Jennifer Gray, Prof. Hong Koo Kim, Prof. Guangyong Li, Prof. Karl



Johnson, Prof. Smolinski, Prof. Clark, Prof. Guofeng Wang, Prof. Qing-Ming Wang, Prof. Sunil Saxena, Prof. Jorg Wiezorek, Prof. Giovanni Galdi, Prof. Peyman Givi, Prof. Lisa Porter, and all other teachers.

Finally, I want to express my gratitude from bottom of heart to my family, who supports me unconditionally and constantly. Their supports make my research possible. Special thanks should go to my wife Saimin Yang, who has done so much for my study. No words can express my heartfelt appreciation for her.

## 1.0 INTRODUCTION

TiO<sub>2</sub> is a versatile material, which is widely used in our daily life due to its numerous strengths, such as brightness, stability, and high refractive index. The traditional applications of TiO<sub>2</sub> include paint and coating (glazes, enamels), plastics, paper, inks, fibers, food, pharmaceuticals, toothpaste, and cosmetics. Recently, TiO<sub>2</sub> has been received considerable attention for the promising applications in environment, energy, information fields, such as photocatalysis, photovoltaics, batteries, data storage. For those applications especially photocatalysis and photovoltaics, widely used TiO<sub>2</sub> particles have its limitations, such as large band gap (3.2eV), slow carrier transport. Large band gap means inefficiency of utilizing solar light, and slow carrier transport increases the chance of recombination. My research topic will focus on band gap engineering and carrier transport in TiO<sub>2</sub> in order to tackle these issues. Effects of doping, morphology control, and surface treatment were systematically studied. Modified TiO<sub>2</sub> could be used in applications such as photocatalysis, solar cells (especially dye sensitized solar cells) more efficiently.

### 1.1 TiO<sub>2</sub> POLYMORPHS

Common polymorphs of TiO<sub>2</sub> are a rutile phase (tetragonal, space group P4<sub>2</sub>/mnm, E<sub>g</sub> ~ 3.05 eV), an anatase phase (tetragonal, I4<sub>1</sub>/amd, E<sub>g</sub> ~ 3.23 eV), and a brookite phase

(orthorhombic,  $Pbca$ ,  $E_g \sim 3.26 \text{ eV}$ )<sup>1-3</sup>. Crystal parameters are  $a=4.5937\text{\AA}$ ,  $c=2.9587\text{\AA}$  for rutile,  $a=3.7845\text{\AA}$ ,  $c=9.5143\text{\AA}$  for anatase,  $a=5.4558\text{\AA}$ ,  $b=9.1819\text{\AA}$ ,  $c=5.1429\text{\AA}$  for brookite, and their representative unit cells are illustrated in Figure 1-1. Rutile is a thermodynamically stable phase, which has 1.2-2.8 kcal/mole energy than anatase. Anatase is a metastable phase, and it shows superior photocatalysis performance because of fast carrier transport and less recombination. The metastable anatase transforms to rutile phase irreversibly at the temperature of  $700^\circ\text{C}\sim 1000^\circ\text{C}$ , which is determined by several factors including a crystallite size and an impurity level.

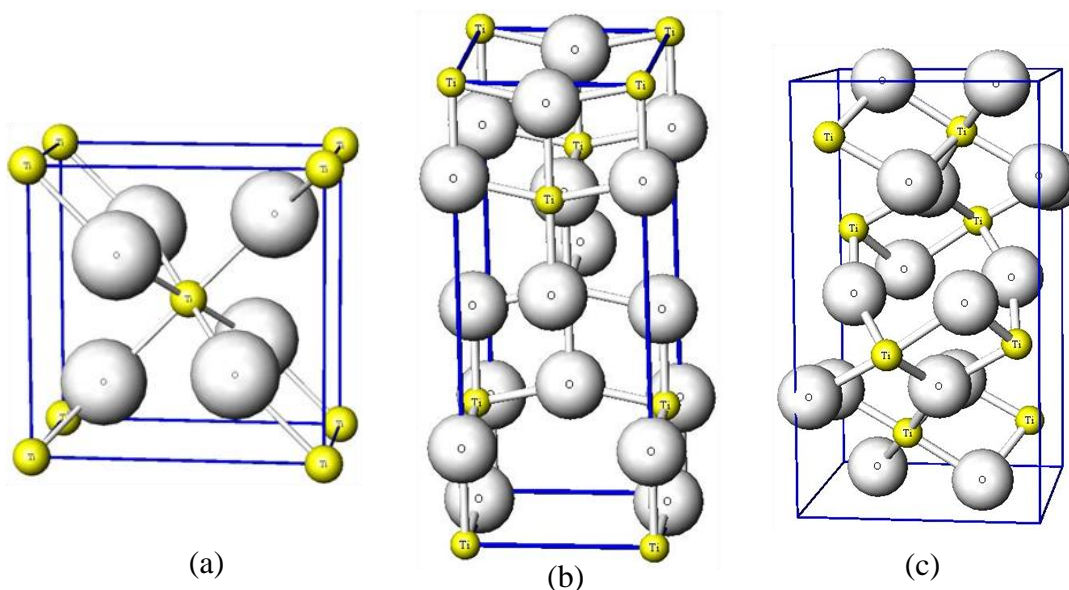


**Figure 1-1 Unit cells of  $\text{TiO}_2$  polymorphs (a) rutile, (b) anatase, (c) brookite**

The crystal structures of  $\text{TiO}_2$  polymorphs are envisaged from the viewpoint of an oxygen octahedron frame, which is composed of one Ti cation sitting in the center and six O anions occupying corners. Each oxygen corner is shared by three octahedra, and this configuration results in 1:2 (Ti:O) stoichiometric ratio in ideal situation. There are multiple methods to satisfy stoichiometric requirement since sharing could be corner, edge, and/or face. Each octahedron in the rutile  $\text{TiO}_2$  is surrounded by ten neighboring octahedra (two sharing the

edge of the octahedron and eight sharing the corner of the octahedron. In the anatase structure, each octahedron is in contact with eight octahedra (four sharing the edge and four sharing the corner). Figure 1-2 (a-c) present octahedral structures of different  $\text{TiO}_2$  polymorphs, and Figure 1-2 (d) shows the characteristic octahedral filament of rutile along  $[001]$  direction. The knowledge of octahedral arrangement has been employed to interpret the influence of  $\text{TiCl}_4$  concentration on formation of different structures in hydrothermal reactions.<sup>4</sup>

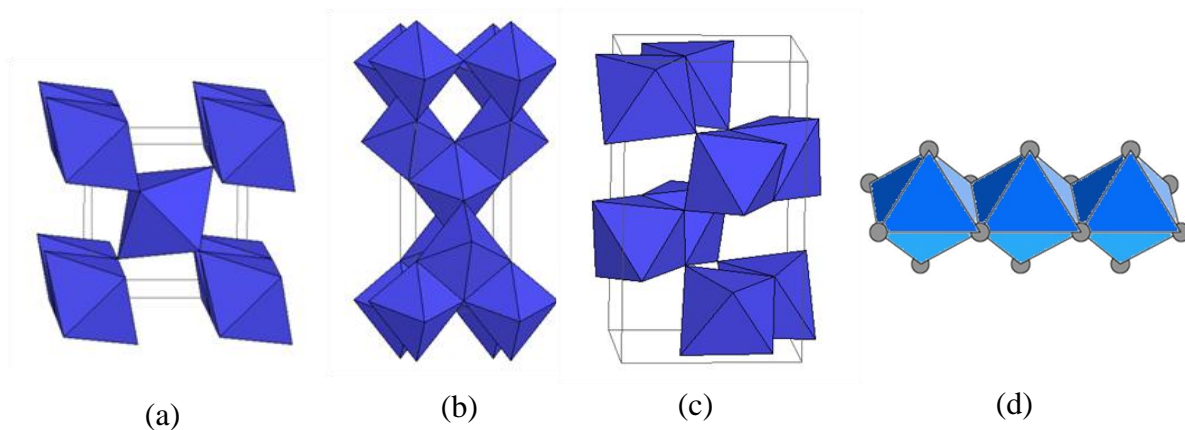


**Figure 1-2 Octahedra stacking of (a) rutile, (b) anatase, (c) brookite; (d) octahedral filament along  $[001]$  direction for rutile**

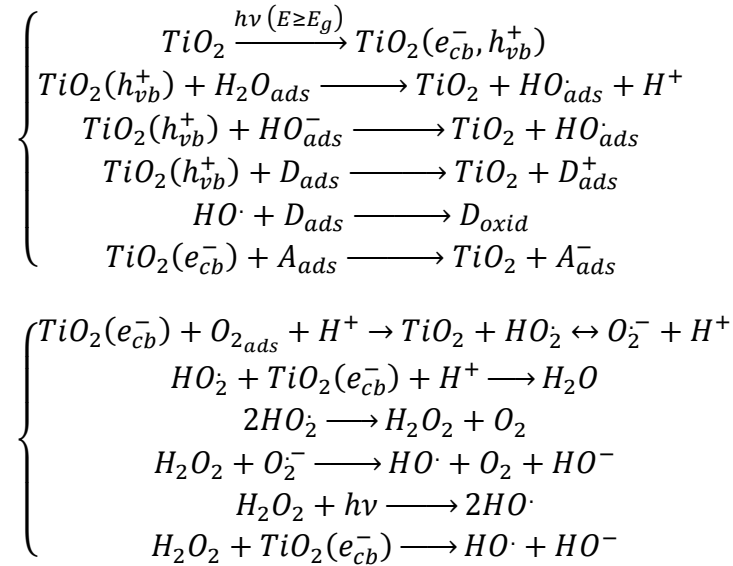
Fundamental difference of crystalline structure will end up with different physical properties, such as optical properties, band gaps, carrier transport. Rutile is one of the highest refractive index minerals ( $n_o=2.605\sim 2.613$ ,  $n_e=2.899\sim 2.901$ ), and has a strong anisotropy and dispersion. Anatase has the same uniaxial type, and its refractive index is  $n_o=2.561$ ,  $n_e=2.488$ , while brookite is a biaxial type ( $n_\alpha=2.583$ ,  $n_\beta=2.584$ ,  $n_\gamma=2.700$ ). The difference between band gap structures and carrier transport also comes from this atomistic arrangement.

## 1.2 APPLICATIONS

The applications of TiO<sub>2</sub> as an advanced material are summarized in this section, including photocatalysis, dye sensitized solar cell, batteries, memristor, et al.

### 1.2.1 Photocatalysis

Photocatalytic behavior of TiO<sub>2</sub> has been extensively explored since it was discovered in 1970s<sup>5</sup>. When TiO<sub>2</sub> is exposed to UV light, the light is absorbed and electron/hole pairs are generated in the conduction and valence bands. Holes in the valence band will oxidize/mineralize pollutant target directly or indirectly (via mediator hydroxyl radical). If the adsorbed A is O<sub>2</sub>, O<sub>2</sub> will react with an electron from the conduction band to generate a hydroxyl radical as described in the second set of reactions. The sequence of the photocatalysis reaction of TiO<sub>2</sub> in water is summarized as following<sup>6</sup>:



The subscripts used in the equations have meanings: ads, adsorbed; cb, conduction band; vb, valence band; oxid, oxidized.

The photocatalytic reaction is schematically explained in Figure 1-3. Since this redox reaction based mineralization has a power to decompose toxic pollutants such as 4-chlorophenol, benzene, it has been widely used in water treatment and surface self-cleaning. Due to its nature using solar light, the photocatalysis based system can be installed both in rural and urban areas without an external power source. For example, Noxer block is a cement mortar block with a  $\text{TiO}_2$  surface layer which treats pollutants in the air. This converts nitrogen oxides ( $\text{NO}_x$ ) to harmless nitrate ions by using the sunlight. Tens of towns in Japan and England have placed the noxer blocks in street paving.

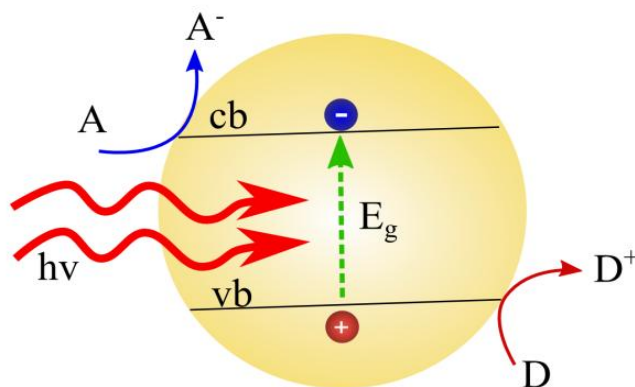


**Figure 1-3 Simplified diagram of heterogeneous photocatalytic process**

Another application of photocatalysis is water splitting and  $\text{CO}_2$  reduction, both of which utilize the electrons that are optically excited to the conduction band.<sup>7,8</sup> Photocatalytic splitting of water by  $\text{TiO}_2$  has received a considerable amount of attentions. For hydrogen production, the conduction band and valence band edges should be well matched with the redox potentials of

water, as shown in Figure 1-4. The conduction level should be higher than hydrogen production level ( $E_{\text{H}_2/\text{H}_2\text{O}}$ ) while the valence band should be lower than water oxidation level ( $E_{\text{O}_2/\text{H}_2\text{O}}$ ). Electrons and holes will be generated on the semiconductor site, and holes generate  $\text{O}_2$  at semiconductor site, while electrons will migrate to counter electrode to execute reduction forming  $\text{H}_2$ . In addition to that, materials should be chemically stable to resist photocorrosion and have long lifetime of electron/hole pairs.  $\text{TiO}_2$  is a suitable material from the viewpoint of band arrangement and chemical stability requirement.

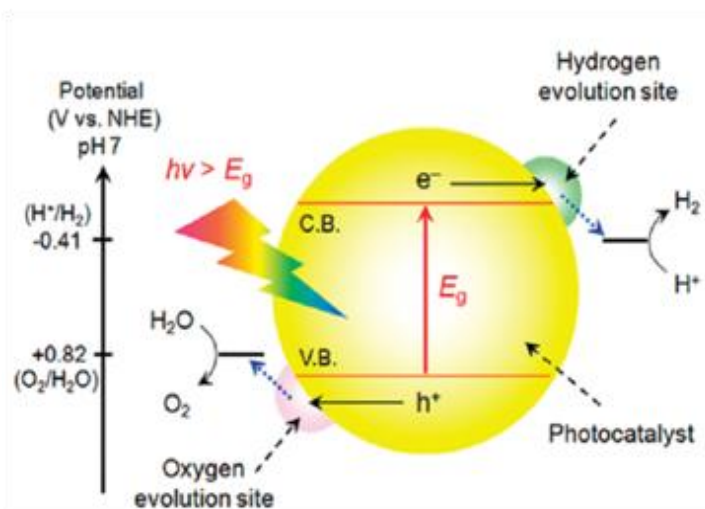


Figure 1-4 Mechanism of  $\text{TiO}_2$  photocatalytic water splitting for hydrogen production<sup>9</sup>

One kind of photoelectrochemical cells that is applied to water splitting is schematically explained in the left plot of Figure 1-4. An interesting development is the deployment of particulate and colloidal semiconductor.<sup>9,10</sup> Particulate semiconductor consists of a wide band gap semiconductor (such as  $\text{TiO}_2$ ) powder or colloid and a noble metal (such as Pt) which is fused to semiconductor to work as co-catalyst. The system is a miniature of

photoelectrochemical cell, and mixed  $H_2$  and  $O_2$  are formed at same place. The roles of co-catalyst are to lower the electrochemical overpotentials associated with the multielectron water oxidation and reduction reaction and provide an interface to enhance electron-hole separation.  $RuO_2$  and  $IrO_2$  are best known catalyst for water oxidation, whereas noble metals (Pt, Pd, and Ni) are commonly used as water reduction. In this particulate paradigm, photocatalysis can take place in the homogeneous phase without the requirement of expensive transparent electrodes and without the need for directional illumination.

One drawback of particulate semiconductor is its back reaction since catalyst for  $H_2/O_2$  is also a good catalyst for the recombination of  $H_2/O_2$ . If no prevention is taken to tackle this issue, the system will end up with photostationary state, where forward and back reaction reach equilibrium. Several techniques have been developed to address this issue. For example, a specific photoreactor design circulates catalyst suspension inside a transparent, semipermeable polymer pipe, which separates  $H_2$  and  $O_2$  as they are formed. It has also been reported that the addition of chemical additives (electron donor including hydrocarbons and inorganic ions, carbonate salt) were able to promote hydrogen production by suppressing recombination. Novel structures have been investigated to improve water-splitting. A  $Cr_2O_3$  nanoscale coating on Rh particle can inhibit the back reaction by blocking access of  $O_2$  to Rh particles.

Another important factor limiting the efficiency of photocatalysis is the band gap of semiconductors. In principle, smaller band gap means broader solar spectrum will be absorbed to produce more electron/hole pairs. However, electrons that are produced by surpa-bandgap photons relax to conduction band edge dissipating excess energy higher than band gap in a heat form. This thermalization loss requires an optimum band gap value to achieve a maximum power output. Schockley and Queisser has discussed this issue and found that maximum efficiency of



electricity conversion (~30%) could be achieved using 1.4eV band gap material in a single p-n junction.<sup>11</sup> In terms of the light absorption, the ideal band gap of the semiconductor for the water splitting is about 1.23eV. On top of this number, however, an additional electric potential of the electrons is required in order to electrolyze water smoothly from the viewpoint of thermodynamics. In order to split water molecules under one sunlight intensity (15-25mA/cm<sup>2</sup>), the electrons need to have an additional electric potential of at least 0.6V. Therefore, the minimum band gap required for water-splitting is around 2.0eV, and its corresponding theoretical efficiency is less than 10%. This indicates that the theoretical efficiency of the water splitting reaction increases as the band gap of the semiconductors gets close to 2.0eV.

The band gaps of commonly used semiconductor are summarized in Figure 1-5. Most oxide semiconductors have the band gap larger than 2 eV, which make them unsuitable for the photocatalytic dissociation of water in terms of the band gap match. For example, the band gap of the anatase phase TiO<sub>2</sub> is 3.2eV. This wide band gap is a major hurdle of achieving high photocatalysis efficiency. Band gap engineering is necessary to overcome this barrier.

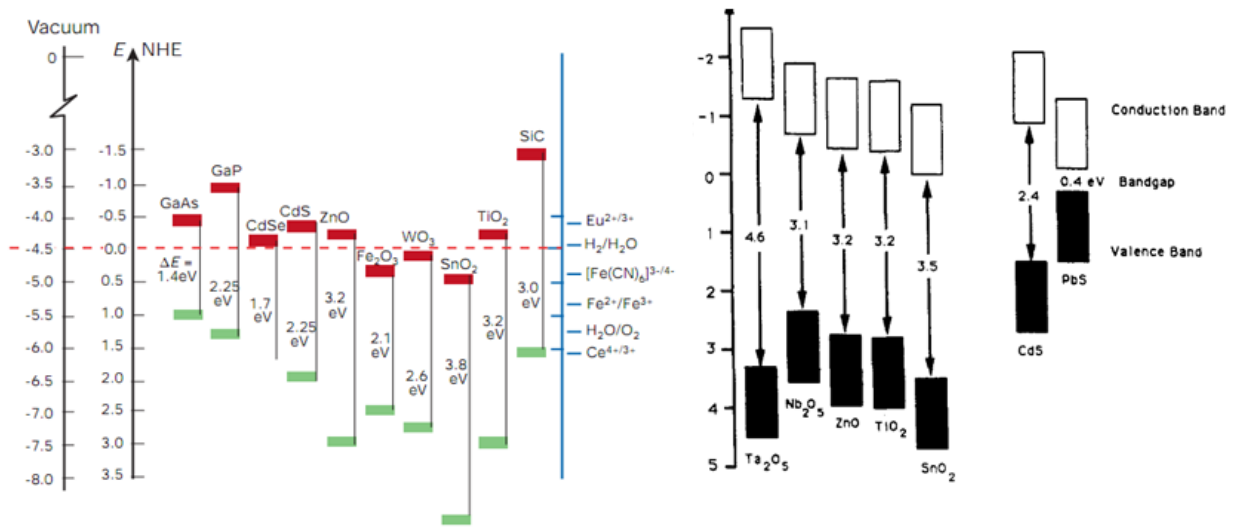


Figure 1-5 Band gap alignment of various semiconductor<sup>12,13</sup>

### 1.2.2 Dye sensitized solar cell

A dye-sensitized solar cells (DSSC) is another class of photoelectrochemical cells, which converts solar light to electric energy by using inorganic semiconductors and sensitizers.<sup>12</sup> DSSCs offer moderate conversion efficiency with other advantages, such as low production cost, easy scale-up, good performance under weak/diffuse light, and compatibility with building window glass and flexible substrates. Therefore, DSSCs have been placed as one of promising alternatives to bulk silicon-based solar cell which is currently dominant in the market.

The history of the dye sensitizer is very long. The photosensitization phenomenon by organic dyes was first reported in 1887.<sup>13</sup> However, the energy conversion efficiency of the devices stays as low as 1% until Graetzel *et al.*, carried out a milestone research and invented a current structure of DSSCs in early 1990s.<sup>14-17</sup> The breakthrough made in Graetzel's cell is the introduction of TiO<sub>2</sub> nanoparticle based photoanode with extremely high surface area.<sup>18</sup> A thin layer of the dyes is coated on the surface of TiO<sub>2</sub> porous film that preferentially collects the photogenerated electrons from the dyes. The energy conversion efficiency of the first Graetzel's cell is 7.1% under the condition of AM 1.5. For the last two decades, DSSCs have been extensively studied, which covers the areas of fundamental physics, device operating mechanism, material innovation, and novel structure design. This leads to the significant increase the performance of the solar cell and the reduced manufacturing cost.<sup>12,19-28</sup> Currently, the efficiency of DSSCs manufactured by Sharp reaches to 10.4% and the efficiency of the submodule produced by Sony goes up to 9.2%.<sup>29</sup> In the lab scale, the best efficiency of DSSCs has already surpassed 11%.<sup>30-33</sup>

Major differences of DSSCs from other semiconductor solar cells are that the solar light is not mainly absorbed by the semiconductor (TiO<sub>2</sub>) and that the electron-hole pair is separated not

by the built-in-potential of a p-n junction. A visible component of the solar light generates electron-hole pairs in the dye sensitizer which anchors on the photoanode of wide bandgap semiconductor nanoparticles. When the electron-hole pairs are formed in the dye molecules, they are quickly separated at a picosecond scale due to the difference in energy levels. Electrons are injected from the dye to the conduction band of the photoanode, and are transferred to the transparent conducting oxide (TCO) film that is coated on the glass. Holes in the dye molecules are delivered to the electrolyte through a redox reaction. In this structure, the maximum output voltage is the difference between Fermi energy of the semiconductor film and redox potential of the electrolyte. The operating principle of DSSCs and the potential source for a back-electron transfer is schematically summarized in Figure 1-6.

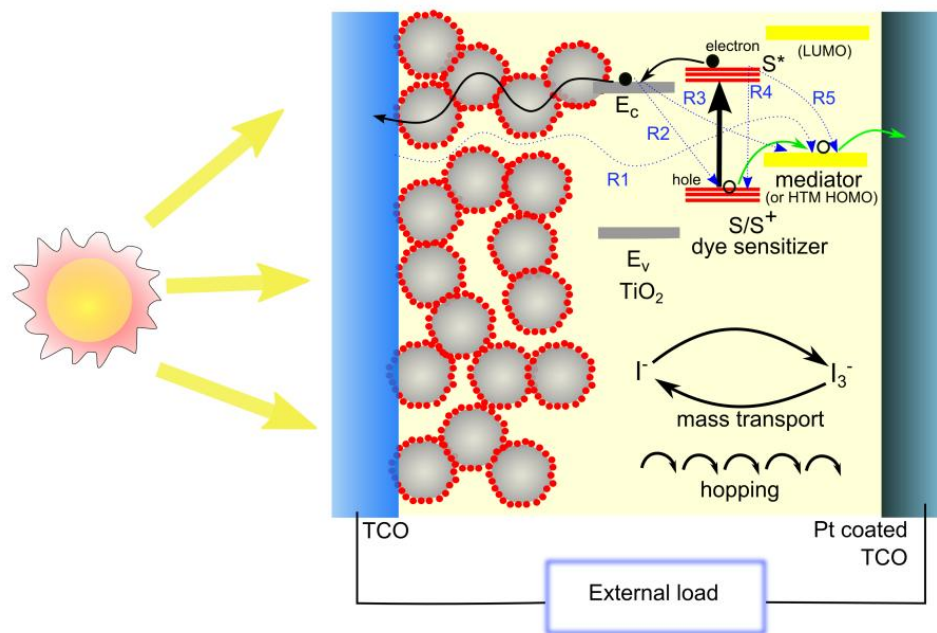


**Figure 1-6 Schematics of dye-sensitized solar cell**

Photoanode acts as electron transport path, light path, and dye anchoring scaffold. It is one of the most important components in DSSC. Carrier injection, transport, trapping, and

recombination are closely related to material, morphology, phase of photoanode. Related challenging issues will be addressed in the challenging issue section in detail.

A dye sensitizer is a major component to absorb incoming solar light generating electron/hole pairs. The role of sensitizer requires its well matched energy level to facilitate efficient electron injection and dye regeneration, strong physical anchoring to photoanode, sufficient absorption of solar light, and stable operation for a long period. Metal-complex, metal-free organic dye, natural dye, and quantum dot have been used as sensitizing materials. The widely used sensitizer is polypyridyl complex of ruthenium because of its high efficiency and long term stability. N3, N719 are typical examples, black dye extends the light absorption to near IR range, and amphiphilic Z907 shows higher stability at high temperature application. Organic dye is an emerging sensitizer because of tunable band gap, large extinction coefficient, and relative cheap cost.

Electrolyte performs mediator function to deliver hole through redox reaction or direct hole transport. It can be divided into organic solvent liquid, solvent free liquid, quasi-solid, and solid electrolytes. The highest efficient DSSCs are made of organic solvent liquid electrolyte due to its fast ion diffusion and ease of infiltration. The commonly employed redox couple is  $I^-/I_3^-$  pairs. The electron transfer from  $TiO_2$  to  $I_3^-$  at sensitizer site is slow, and it  $I^-$  can be fast regenerated from  $I_3^-$  at the counter electrode. Several additives, such as lithium ion, 4-tert-butylpyridine (TBP), N-methylbenzimidazole (NMBI), are incorporated into solvent in order to obtain higher short circuit current and/or suppress electron/hole recombination. However organic solvent liquid electrolyte is composed of volatile solvent, which is not stable at high temperature or difficult to seal and assemble. Solvent-free liquid (or called ionic liquid), quasi-liquid, and solid electrolytes has been explored to address drawbacks of organic solvent liquid electrolyte.

Transparent conducting oxide (TCO) plays a pivotal role in optoelectrical devices, fulfilling the function of light transmittance and conducting electrode simultaneously. In DSSC, TCO is additionally required to be chemically stable enduring corrosive electrolyte and high temperature stable due to partial sintering process of TiO<sub>2</sub> photoanode. Tin-doped indium oxide (ITO) is not suitable for DSSC because of its significant drop of performance after annealing above 300°C. Fluorine-doped tin oxide (FTO) is widely used TCO in DSSC due to its good thermal and chemical stability.

### **1.2.3 Other applications**

#### **1.2.3.1 Lithium ion battery**

Lithium ion battery is widely used in consumer electronics because of its several strengths, such as high energy density, no memory effect, and slow charge dissipation in a standby state. One of the key elements in the lithium ion battery is anode in which TiO<sub>2</sub> nanomaterials with 3-D structure can be implemented to increase the charge capacity of the lithium ion battery.<sup>34</sup> Due to structural perfection of mesoscopic skeleton, lithium ions can be inserted into the internal space of nanostructured TiO<sub>2</sub>.<sup>35</sup> Two pairs of cathodic/anodic peaks at 1.5 and 1.6 V vs. Li/Li<sup>+</sup>, which are experimental proofs for the charging and discharging of lithium ions, have been observed in TiO<sub>2</sub> with a good mesoporous structure. Intercalation of lithium ions into TiO<sub>2</sub> is reported to spontaneously result in Li-rich phase (Li<sub>0.6</sub>TiO<sub>2</sub>) and Li-poor phase (Li<sub>0.01</sub>TiO<sub>2</sub>). An equilibrium lithium flux rate between Li-rich and Li-poor phases is as high as  $1.2 \times 10^{20} \text{ s}^{-1} \text{ m}^{-1}$  by lithium magic-angle-spinning solid state NMR.<sup>36</sup> TiO<sub>2</sub> nanoparticles are also used to improve the performance of an ionic polymeric membrane in the lithium ion battery. When added, TiO<sub>2</sub> nanoparticles change the recrystallization kinetics of the polyethylene

oxide (PEO) because the tremendous surface area and Lewis-acid characteristics of TiO<sub>2</sub> nanoparticles. This, in turn, increases the ionic conductivity of the polymeric membrane and the stability of the lithium ion battery.<sup>37</sup>

### **1.2.3.2 Dilute magnetic semiconductor oxide**

If spin states of electrons (spin-up and spin-down) in the transistors are controlled, the transistors have much faster process speed, smaller power consumption, and higher integration intensity, compared with conventional electronic devices. This new technology is called as spintronics. Dilute magnetic semiconducting oxide (DMSO) is a cornerstone to realize the fascinating promise of spintronic devices. When a small amount of magnetic impurities is doped into semiconductors, the spins of the electrons in the non-magnetic semiconductor may be coherently aligned through the interaction with the magnetic impurities. This means that electrons can be polarized under the external magnetic field and the ferromagnetism may emerge in the materials with the originally non-magnetic host. Commonly investigated oxide materials in the early stage of the spintronics are III-V semiconductors such as ZnO, and TiO<sub>2</sub>, because these materials can increase Curie transition temperature of DMSO to be higher than room temperature. Matsumoto *et al.*, have serendipitously shown that ferromagnetism of Co doped anatase TiO<sub>2</sub> film is stable at room temperature.<sup>38</sup> This observation lead to intensive studies on TiO<sub>2</sub> based DMSO. Huge potential of the spintronics and concerns on the origin of ferromagnetism on DMSO have rationalized further study on the uniform doping and defect control with the help of new characterizing techniques. The current view of scientific community towards this DMSO field is cautious optimism.<sup>39</sup>

### 1.2.3.3 Memristor

Memristor is one of the four fundamentals in passive circuit elements (others are resistor, capacitor, inductor), and it has been predicted by Leon Chua in 1971. The missing memristor has been discovered by Hewlett Packard (HP) labs recently.<sup>40</sup> The configuration of memristor is composed of two platinum plates and semiconductor, which is partially doped. When external voltage is applied under two electrodes, this system will present a coupled motion of atoms and electrons. The current-voltage relationship of the memristor displays a pinched hysteresis (refer to Figure 1-7(b)).  $\text{TiO}_2$  has been chosen as the material of the memristor, because it is easily self-doped with oxygen vacancies that provide some sort of mobility. If the electric potential of 1~2 V is applied to the nanoscale  $\text{TiO}_2$  film, a remarkable electric field is built up in the film and the drift velocity of the charge species is exponentially increased. A typical I-V curve in the  $\text{TiO}_2$  memristor is presented in Figure 1-7(c).

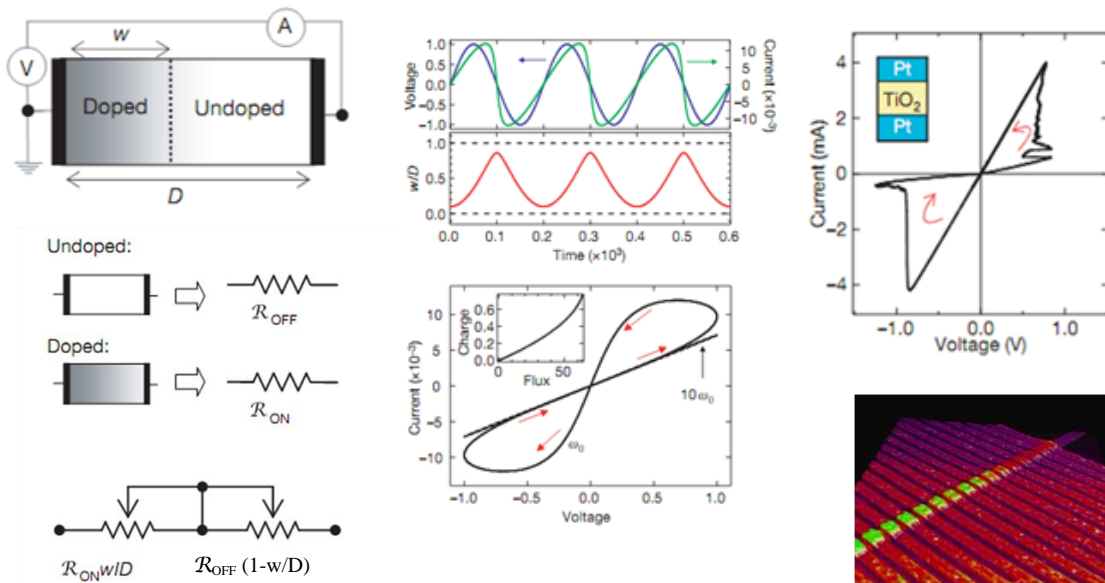


Figure 1-7 (a) Memresistor configuration, (b) characteristic current voltage curve, (c) actual measured IV curve, (d) AFM diagram of a circuit with 17 memristors<sup>41</sup>

The memresistor can be potentially used to store data and perform digital logics. One application of memresistor is Resistive Random Access Memory (ReRAM), which could lower the power consumption and data access time of existing RAM. In 2011, HP and Hynix semiconductor have signed a joint development agreement to bring the memresistor to market.

### **1.3 CHALLENGES OF TiO<sub>2</sub> FOR ADVANCED APPLICATIONS**

As described in the above, TiO<sub>2</sub> has unique properties that advance the current technology in the fields of catalysis, solar cell, energy storage, and semiconductor devices. However, there are several issues to be addressed in order to maximize the potential of TiO<sub>2</sub>.

First of all, the band gap of TiO<sub>2</sub> is not suitable in harnessing the full spectrum of solar spectrum. Light absorption of TiO<sub>2</sub> is an important process for solar light related application especially for photocatalysis. The wide band gap property of TiO<sub>2</sub> determines that its light absorption is limited UV and lower wavelength than UV. The solar spectrum is a broad distribution as shown in Figure 1-8, and the portion of UV light energy is only small part of total energy. Inability of utilizing visible and/or near IR energy, which compose of majority of solar energy, will hurdle its efficiency. Considering the absorption window and thermalization loss, theoretical efficiency can be calculated. As mentioned in Section 1.2.2, Schockley and Queisser proposed maximum theoretical efficiency limit for single p/n junction solar cell, and optimum band gap for solar cell is 1.4eV which possesses ~30% efficiency. Wide band gap of TiO<sub>2</sub>, which is far away from the optimum band gap, means a significant loss of solar energy.



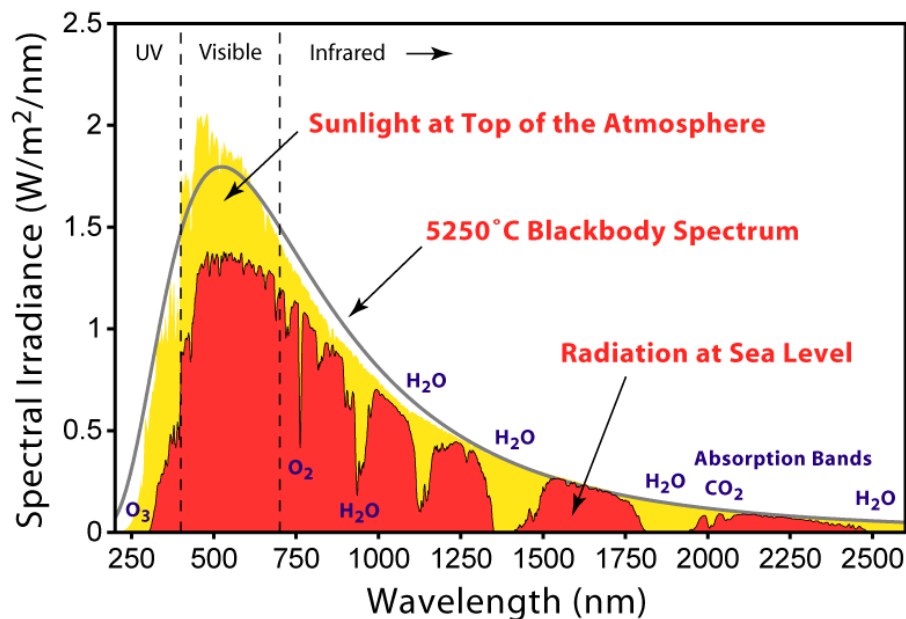
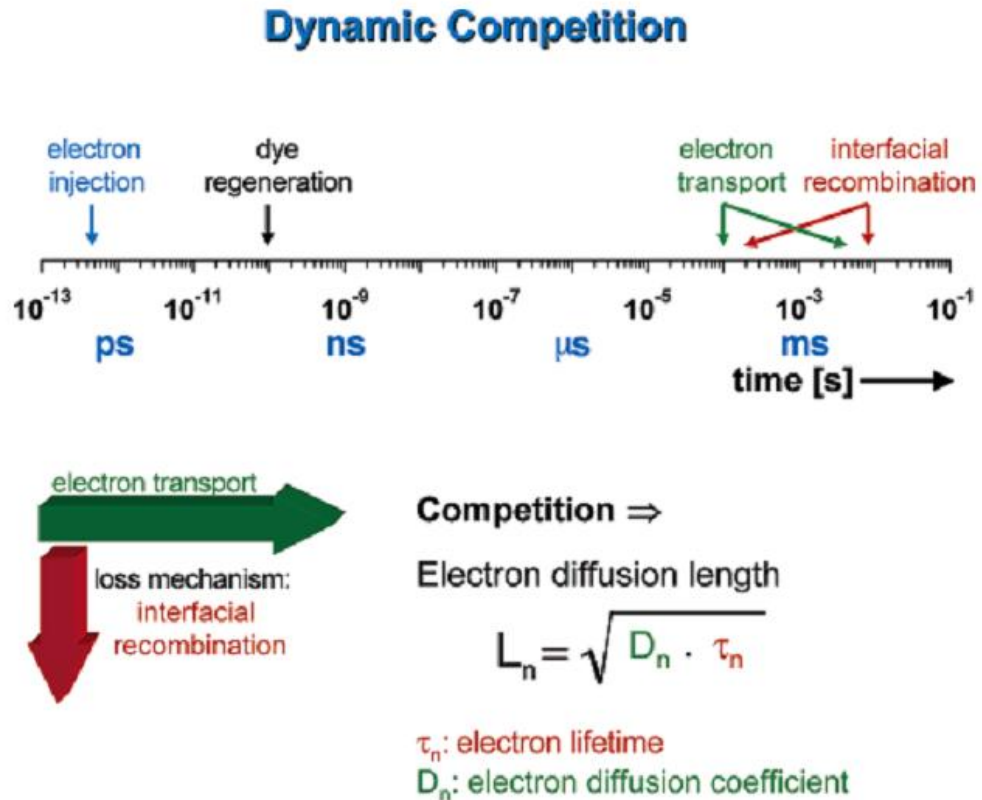


Figure 1-8 Solar light spectrum

Second issue is that the band edge position of TiO<sub>2</sub> is not very well aligned with the redox potentials of the water. As talked in water-splitting part, conduction band and valence band edge positions are very critical to accomplish the task of hydrogen production. The position of band edges is also problematic in DSSCs. In this solar cell, the conduction band edge of TiO<sub>2</sub> needs to be lower than the lowest unoccupied molecular orbit (LUMO) of the dye sensitizer for efficient electron injection, while extremely low conduction band edge decreases the open circuit voltage. Hence, it is of importance to control/modify band edge position to achieve an optimum output.

The third factor that needs further study is how to control dynamics of carrier transport. In the case of DSSC, the carrier collection efficiency is one of the critical parameter to obtain high energy conversion efficiency. A conventional architecture of DSSC utilizes the thick film of TiO<sub>2</sub> nanoparticles, as shown in Figure 1-6. This traditional mesoporous structure has benefits of enormous interface area that facilitates dye adsorption. However, numerous boundaries between

particles impose possible trapping and recombination, which will be detrimental to carrier transport. Theoretical and practical backward reaction paths in DSSC can be described in Figure 1-6. From the time scale of DSSC (Figure 1-9), the most possible happened backward reaction is path R1 and R3.



**Figure 1-9 Dynamics time scale in Dye-Sensitized Solar Cell<sup>31</sup>**

The time scale at different stages of the carrier transport ranges from pico-second to micro-second. Electron-hole generation in dye sensitizer and electron injection to TiO<sub>2</sub> happens extremely fast, around picosecond order, dye generation with assistance of electrolyte is around nanosecond. The hole transport in liquid electrolyte is relatively fast, electrons pass through nanocrystalline network in the order of millisecond. The slow transport of electrons is confronted with other competing effects such as interfacial recombinations.<sup>41</sup> Therefore, it is

requested to enhance the electron transport and collection using novel structure and/or materials without deteriorating the anchoring behavior of the dye. The 1-D nanomaterials vertically standing on TCO coated glass substrates are such a good candidates. The electron transport along the long axis of the crystalline nanowires is expected to be several orders of magnitude faster than the electron percolation via a random walk in the spherical nanoparticles.<sup>42</sup>

Last question shed on  $\text{TiO}_2$  is related to surface chemical properties which directly influence DSSC performance. The surface area and surface potential of the oxide nanoparticles control the amount the dye adsorbed on the photoanode, which determines total number of photogenerated carriers. Moreover, the electrons that are injected from the dye molecule migrate in the  $\text{TiO}_2$  anode by a random work hopping without the support of the built-in-potential. To facilitate the dye adsorption and carrier transport, systematical studies on the surface modification of  $\text{TiO}_2$  nanoparticles have been conducted.

## 2.0 BAND GAP ENGINEERING OF TiO<sub>2</sub>

### 2.1 BACKGROUND AND APPROACH

#### 2.1.1 Motivation

Capasso Federico has envisaged the application of band gap engineering in semiconductor devices in late 1980s.<sup>43</sup> He proposed that the concept of band gap engineering, that is, band diagram of semiconductor can be tailored and carriers transport can be continuously tuned for specific application with the assistance of heterojunction and modern growth method. This concept evolves and has spurred numerous developments in different fields, such as graded gap transistor, carbon nanotube/graphene, nanocrystal. For example, band gap of nanocrystal can be tuned in various methods: size, shape (sphere, disk, rod, tetra-rod), alloying, doping, strain tuning, band gap edge warping.<sup>44</sup> For TiO<sub>2</sub>, available routes of band gap engineering can be summarized in Figure 2-1.<sup>45</sup> Basically, it can be divided into two categories to narrow band gap TiO<sub>2</sub>: phases mixing and doping.

The first approach is to use a mixture of complementary phase or materials to achieve broad absorption of light spectrum. Hurum *et al.*<sup>46</sup> reported that a light absorption edge can be extended to visible wavelength in a mixture of anatase TiO<sub>2</sub> with rutile TiO<sub>2</sub>. They argued that rutile TiO<sub>2</sub> particles with lower band gap act as an electron antenna in the visible range.

Heterogeneous semiconductor mixtures, such as CdS/TiO<sub>2</sub>, have been also investigated to increase the response to the visible light via a similar mechanism<sup>47,48</sup>. When the visible light is converted to electron-hole pairs in CdS with a smaller band gap, the electrons in CdS are injected to the conduction band of anatase TiO<sub>2</sub> and are used for the catalytic reaction.

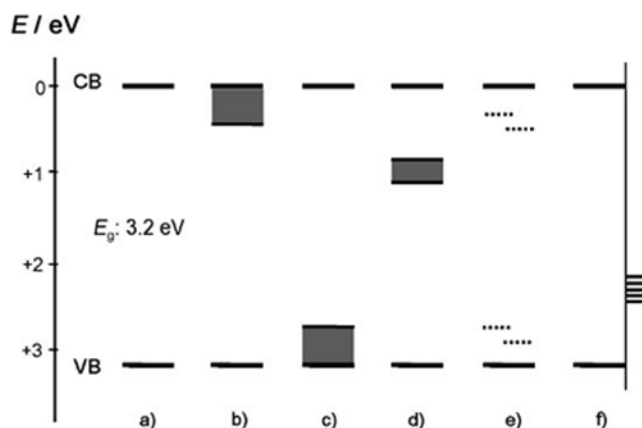


**Figure 2-1 Schematics of band gap alternations: a) pristine TiO<sub>2</sub>; b) and c) phase mixing to lift VB or lower CB; d) creation of discrete band in band gap; e) discrete doping level; f) surface doping<sup>45</sup>**

Another route to increase the photoresponse of TiO<sub>2</sub> under the visible light is to directly modify the energy band of TiO<sub>2</sub> by introducing defect levels between conduction band and valence band. Choi et al<sup>49</sup> systematically analyzed the photo-activities of 21 different metal ion-doped TiO<sub>2</sub> colloids. They found that TiO<sub>2</sub> nanoparticles doped with Fe<sup>3+</sup>, Mo<sup>5+</sup>, Ru<sup>3+</sup>, Os<sup>3+</sup>, Re<sup>5+</sup>, V<sup>4+</sup>, and Rh<sup>3+</sup> have enhanced photoactivity in visible range. This observation has been followed by extensive research on the effect of dopants<sup>50,51</sup>, such as chromium<sup>52,53</sup>, molybdenum<sup>54</sup>, iron<sup>55</sup>, vanadium<sup>56</sup>, platinum<sup>57</sup>, chromium/antimony<sup>58</sup>, and lanthanide ions<sup>59</sup>. A positive effect of the doping on the photocatalysis is explained as the introduction of new defect energy levels, which narrows the band gap of TiO<sub>2</sub> and accelerates the separation of photogenerated carriers. However, there are also contradictory reports suggesting that the metal ion doping is detrimental to the photocatalysis, since the defect levels of dopants trap carriers or

increase the probability of electron-hole recombination. For example, Asilturk *et. al*, recently reported the enhanced photocatalytic property in TiO<sub>2</sub> doped with high concentration of Fe has been reported<sup>60</sup>, while earlier studies show that Fe doping increases the density of electron-hole recombination centers and deteriorates the photocatalytic power<sup>50,61</sup>.

In addition to cation doping, anion doping into TiO<sub>2</sub> has been extensively studied for a decade. Since Asahi *et al.* discovered the visible light absorption in N doped TiO<sub>2</sub><sup>62</sup>, several anions such as nitrogen<sup>63,64</sup>, carbon<sup>65</sup>, sulfur<sup>66</sup>, and fluorine<sup>67,68</sup> were found to enhance the absorption of visible light. A formation of non-oxide phase or new defect level slightly above the valence band of TiO<sub>2</sub> has been suggested to cause the red shift of absorption spectrum in anion doped TiO<sub>2</sub>.

Recently, co-doping of both cation and anion into TiO<sub>2</sub> has been explored to increase the solubility limit of dopants and improve photocatalytic efficiency, because a pair of dopants can self-compensate the excessive electric charge of counter aliovalent dopants<sup>69-71</sup>. For example, nitrogen and iron were incorporated into TiO<sub>2</sub> together to decrease the bandgap more effectively and enhance the photocatalysis of co-doped TiO<sub>2</sub> under the visible light<sup>72-74</sup>. However, previous investigations were mainly focused on TiO<sub>2</sub> doped with a small amount of Fe in which the dopant effect can be easily affected by intrinsic defects and impurities. It is of interest to extend Fe doping level and explore the tunable range of TiO<sub>2</sub> band gap and the correlation among bandgap, electron-hole recombination and photocatalytic power.

### **2.1.2 Fluorescence spectroscopy**

Fluorescence is a type of photoluminescence, which emits light under an external photon stimulus. Another type of photoluminescence is phosphorescence, which usually has longer

lifetime compared with fluorescence. The mechanism of photoluminescence can be illustrated using Jablonski diagram as shown in Figure 2-2.<sup>75</sup>  $S_0$  is the ground state, and its vibrational energy levels are depicted by 0, 1, 2, etc. Its first and second electronic energy levels are represented by  $S_1$  and  $S_2$ , and the first triplet state is denoted by  $T_1$ . The terminologies singlet and triplet state are the result of the spin quantum number  $s$ .<sup>76</sup> More precisely, it is determined by the multiplicity ( $M$ ) parameter. The energy of triplet state is slightly lower than the singlet state energy. When a photon hits a matter, energy of photon could lift electron from ground to excited singlet state. Excited electron will relax to the lowest vibrational energy level of  $S_1$  through internal conversion. The time scale of internal conversion is generally around  $10^{-12}$ s. Then the electron can either jump to the ground state with fluorescence or transfer to triplet state via intersystem crossing. If the electron transfers to triplet state, it will return to ground state with phosphorescence. Generally, the emission rate of fluorescence is  $10^8 \text{ s}^{-1}$ , and that of phosphorescence is  $10^3$  to  $10^0 \text{ s}^{-1}$ .

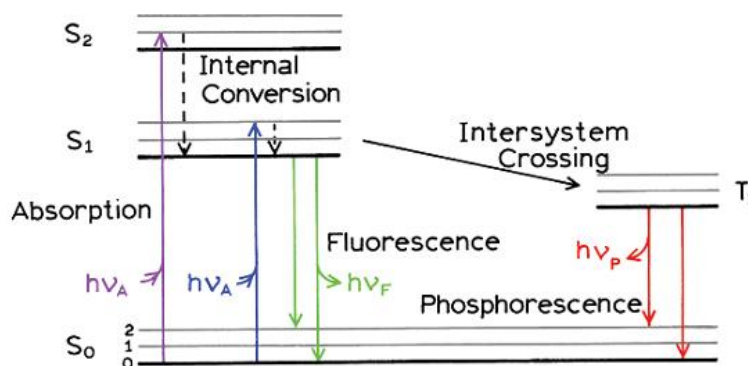


**Figure 2-2 Jablonski diagram for fluorescence,  $S_0$  is ground state,  $S_1$  and  $S_2$  are excited singlet states, and  $T_1$  is triplet state <sup>75</sup>**

The internal conversion is a few orders faster than fluorescence, which results in that the emission spectrum is independent of excitation wavelength. The electron could be excited to higher electronic and vibrational energy level, but its excess energy is quickly dissipated, leaving

electron in the lowest vibrational level of  $S_1$ . Therefore, fluorescence mainly reflects the difference between ground states and the lowest energy level in  $S_1$ . This independence of excitation wavelength is also called Kasha's rule. Some exceptions, such as existence of two ionized states, do exist.

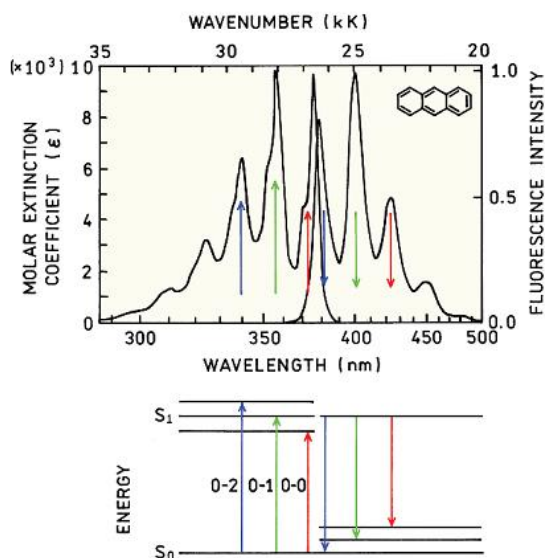


**Figure 2-3 Absorption and emission spectra of anthracene, and its mirror-image can be interpreted as similar spacings of vibrational levels<sup>75</sup>**

Another common feature for many fluorophores is the symmetry between an absorption spectrum and an emission spectrum, the so-called mirror-image rule. As shown in Figure 2-3, absorption and emission spectra of anthracene have a very high symmetry, which comes from the similar spacing between vibrational energies at different electronic distribution states,  $S_0$  and  $S_1$ . The individual peak in the spectrum of anthracene originates from the  $S_0$  to one vibrational level of  $S_1$ , or  $S_1$  to one vibrational level of  $S_0$ . The vibrational energy level is not significantly altered by different electronic states.

Fluorophore normally is aromatic amino acids, NADH, flavins, derivatives of pyridoxyl, and chlorophyll. In addition to these conventional fluorophores, new materials, such as



semiconductor nanoparticle (quantum dot), lanthanide ( $\text{Eu}^{3+}$ ,  $\text{Tb}^{3+}$ ), metal-ligand complexes, have become popular because of their unique properties.

Fluorescence spectroscopy is a technique with extraordinary sensitivity and selectivity, and is widely used in biochemical, medical, and chemical research.

### 2.1.3 X-ray Photoelectron spectroscopy (XPS)

X-ray photoelectron spectroscopy is an important surface characterization technique. It utilizes the soft X-rays, (normally Al  $K\alpha$  or Mg  $K\alpha$  with 1000 ~ 2000 eV), to probe the properties of materials by a special form of photoemission. Notations used in XPS and X-ray are correlated with quantum numbers as shown in Table 2-1.  $n$  is the principle quantum number, determining the energy of the quantum state.  $l$  is the angular momentum quantum number, and different  $l$  numbers (0, 1, 2, 3) represent different shells (s, p, d, f).  $j$  is the total angular momentum quantum number, which is the combination of orbital angular momentum and intrinsic angular momentum (spin).

**Table 2-1 The relation between quantum number and XPS, X-ray notation<sup>77</sup>**

Quantum number			Notation	
n	l	j	XPS	X-ray
1	0	1/2	1s <sub>1/2</sub>	K
2	0	1/2	2s <sub>1/2</sub>	L <sub>1</sub>
2	1	1/2	2p <sub>1/2</sub>	L <sub>2</sub>
2	1	3/2	2p <sub>3/2</sub>	L <sub>3</sub>
3	0	1/2	3s <sub>1/2</sub>	M <sub>1</sub>
3	1	1/2	3p <sub>1/2</sub>	M <sub>2</sub>
3	1	3/2	3p <sub>3/2</sub>	M <sub>3</sub>
3	2	3/2	3d <sub>3/2</sub>	M <sub>4</sub>
3	2	5/2	3d <sub>5/2</sub>	M <sub>5</sub>
etc.			etc.	

A typical process of XPS is illustrated in Figure 2-4 (a): an electron from a core level (this case K) is knocked off by the incident X-ray. The kinetic energy ( $E_K$ ) of the ejected electron can be measured through an electron energy analyzer, and the binding energy ( $E_B$ ) can be calculated using the following equation:

$$E_B = h\nu - E_K - W \quad (2-1)$$

where  $W$  is work function.

The spectrum from XPS measurement is the intensity as a function binding energy, and it could be superimposed on a schematic of electronic structure as shown in Figure 2-4 (b). It is clear that peaks in the spectrum are related to the electrons at different orbitals very accurately. It should be mentioned that only electrons without energy loss during the process represent characteristic peaks in the spectrum and those which undergo inelastic scattering and have energy losses contribute to background of the spectrum.

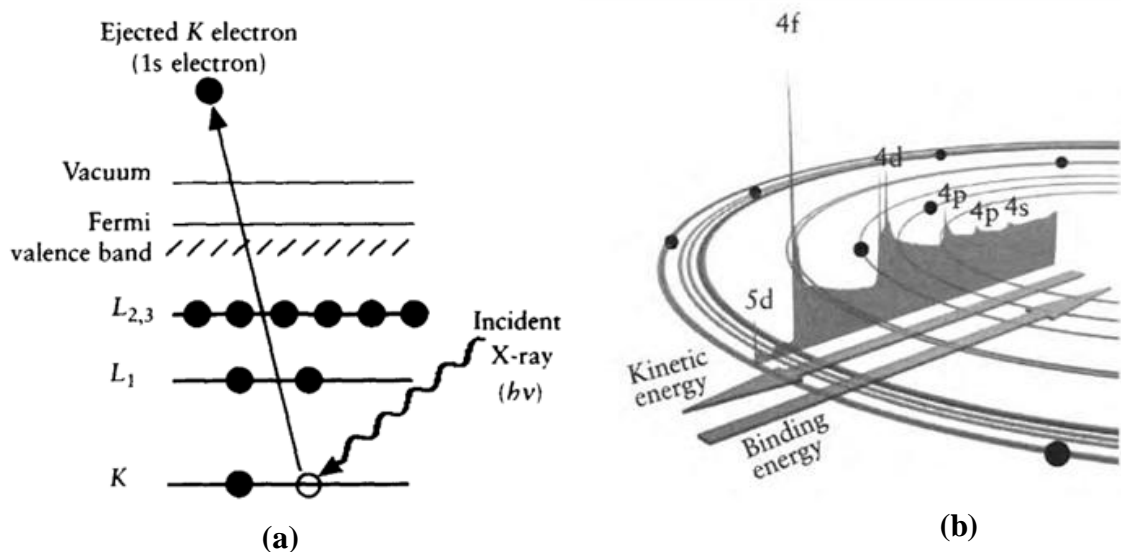
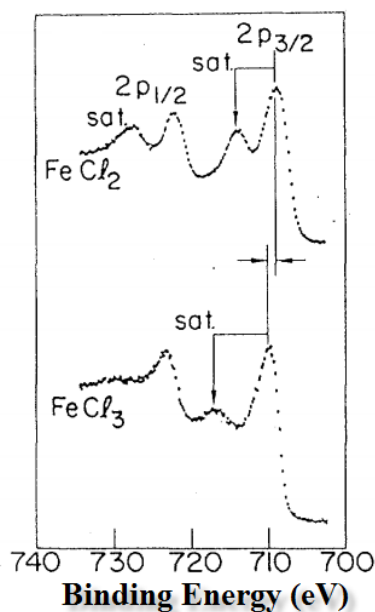


Figure 2-4 Schematics of XPS process of 1s signal (a) and the correlation between XPS spectra and energy orbitals (b) <sup>77</sup>

The uniqueness of XPS is the spectrum is strongly related to chemical states in addition to element information. From the high-resolution spectrum, almost all elements in periodic table exhibit a chemical shift, which varies from a fraction of an eV to several eVs. This chemical shift is traced back to either initial-state effects or final-state effects. For initial-state effects, the charge on the atom prior to photoemission is critical for the spectrum, and it is a dominant factor for most elements. This initial-state effect could reflect the magnitude of chemical shift. If there are more bonds with electronegative atoms that are in place, it will result in the greater the positive XPS chemical shift. That is the reason that C-O bond in an organic polymer is positively shifted 1.6 eV relative to the unfunctionalized (methylene) carbon, and C=O and O-C-O are both shifted by 2.9 eV. As shown in Figure 2-5, the main peak of  $2P_{3/2}$  for  $Fe^{3+}$  is shifted to a higher binding energy compared to that for  $Fe^{2+}$ .<sup>78</sup>



**Figure 2-5 Effect of chemical state on XPS spectra, Fe  $2p_{3/2}$  and its satellite line shift at different chemical states ( $Fe^{2+}$ ,  $Fe^{3+}$ )<sup>78</sup>**

Generally speaking, there is a positive shift between the elemental form and mono-, di- or trivalent ions. Exception does exist. For example, a negative chemical shift of about 2 eV

between Ce and CeO<sub>2</sub>. This is caused by very large final-state effects, which occurs following photoelectron emission. Final-state effects include core hole screening, relaxation of electron orbitals, and the polarization of surrounding ions.<sup>77</sup> The satellite peaks in Figure 2-5 and its remarkable shift come from the final-state effects.

## **2.2 DOPING EFFECTS OF NITROGEN, IRON, AND N/Fe CODOPING**

### **2.2.1 Sample preparation**

Titanium (IV) Isopropoxide (TTIP, 97% Aldrich) was used as a Ti-precursor. 46.8 mL of TTIP was poured into 135 mL of de-ionized (DI) water with a vigorous stirring and the mixture was kept for 12 hrs at room temperature. After the hydrolysis reaction was completed, the precipitate was centrifuged and washed using DI water several times, and dried in a vacuum oven at room temperature. The prepared white precipitate (amorphous titanium hydroxide) was used as raw material in hydrothermal reaction. 8 g of amorphous TiO<sub>2</sub> was mixed with 200 mL DI water thoroughly by an overnight stirring. Urea ( $\geq 98\%$ , Sigma-Aldrich) was employed as N source, and Ferric (III) nitrate ( $\geq 98\%$ , Sigma-Aldrich) was used as Fe source. Based on the composition of target materials, precursors containing 10 at% of N and/or 3 at% of Fe were added to TiO<sub>2</sub> mixed water. Then, raw materials were reacted at 175°C for 12 hours. During the hydrothermal reaction, the mixture was stirred at the rate of 300 rpm. When the reaction was finished, powder products were collected, washed, and then dried in a vacuum oven at room temperature. Samples were named pure TiO<sub>2</sub>, N-doped, Fe-doped, and N/Fe-doped TiO<sub>2</sub> after doped elements.

## 2.2.2 Characterization and measurement

Crystal structure of synthesized TiO<sub>2</sub> nanoparticles was investigated by using x-ray diffractometer (X'pert, Philips, Netherland) and Raman spectroscopy (Renishaw inVia Raman microscope). The particle size and morphology were investigated by transmission electron microscope (TEM, JEOL-200CX). The optical bandgap was characterized via UV/Vis spectrometer in an absorption mode (Perkin Elmer Lambda 35). X-ray photoelectron spectra (XPS) of pure and doped TiO<sub>2</sub> were acquired using monochromatic Al-K radiation (100 W), and the core levels of N 1s were calibrated with respect to the C 1s level at 284.5 eV. The formation of hydroxyl radicals on the surface of TiO<sub>2</sub> nanoparticle in water under illuminated light was monitored by a terephthalic acid (TA) fluorescence probe method<sup>79,80</sup>. Fluorescence spectra of terephthalic acid solutions were obtained by using PTI QM-3 Luminescence Spectrofluorometer. For this measurement, three independent samples have been prepared for one type of particle, and its results have been averaged with difference bars. In addition, the photoluminescence (PL) spectra of pure and doped TiO<sub>2</sub> were obtained using a photoluminescence spectrometer (SPEX 1403, SPEX) at 10K.

Photocatalysis of TiO<sub>2</sub> powder was examined by monitoring the dissociation reaction of rhodamine B (Rh. B). UV light with the wavelength of 365 nm and simulated solar light were employed as illumination sources. 0.05 g of pure or doped TiO<sub>2</sub> was dispersed in 40 mL of Rh. B aqueous solution (10 μM), and stirred for five minutes in dark condition. Then the aqueous suspensions were exposed to light while they were stirred. With an interval of 20 min, 4 mL of photoreacted suspension was extracted to measure the amount of dissociated Rh. B. The suspension was centrifuged to separate nanoparticles. UV-Vis spectra of centrifuged solutions were measured by Perkin Elmer Lambda 35 UV/Vis Spectrometer.

### 2.2.3 Results and discussion

X-ray diffraction (XRD) patterns in Figure 2-6 (a) show that all of the synthesized samples have an anatase structure. Additional peaks of the second phase resulting from inhomogeneous doping of Fe or N are not observed. To probe structural changes at micrometer-scale, Raman spectroscopy analysis has been performed. All of Raman spectra in Figure 2-6 (b) show the peaks that are assigned to the modes of anatase  $\text{TiO}_2$ <sup>81</sup>. A dominant peak centered at  $144\text{cm}^{-1}$  is associated with  $E_g(v_6)$  mode. Peaks centered at  $400\text{cm}^{-1}$  and  $514\text{cm}^{-1}$  are associated with  $B_{1g}$  and  $A_{1g}$  modes, and  $638\text{cm}^{-1}$  peak is assigned to  $E_g(v_1)$ . In Fe doped and Fe/N codoped  $\text{TiO}_2$ ,  $B_{1g}$  mode exhibits a slight shift to lower wavenumbers. Because  $B_{1g}$  mode comes from stretching of Ti-O bonds, this slight change is attributed to the substitution of Ti ions with Fe ions.

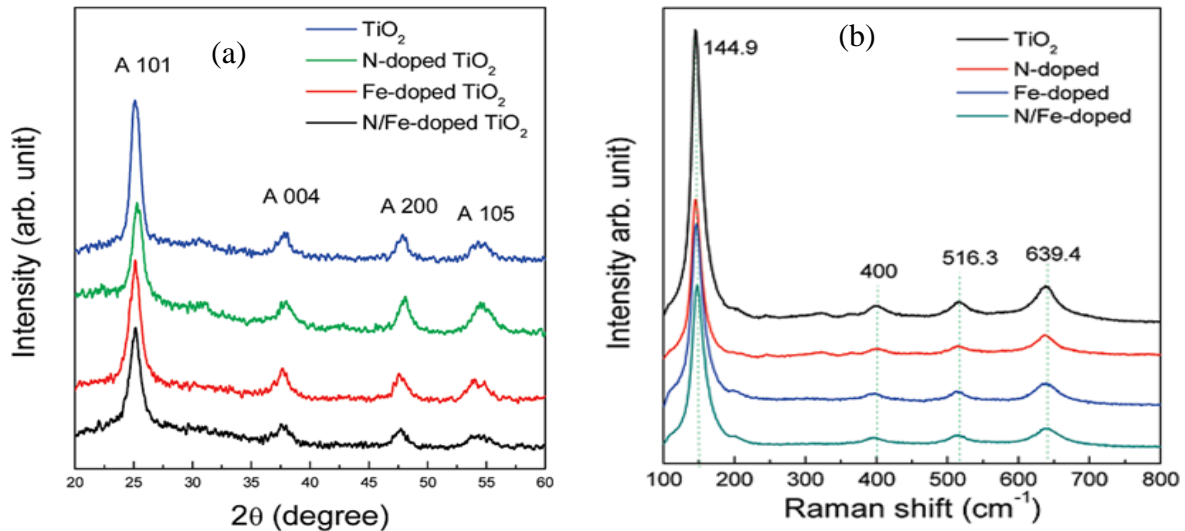


**Figure 2-6 (a) XRD pattern of doped  $\text{TiO}_2$  (b) Raman spectra of doped  $\text{TiO}_2$ , both show anatase phase for synthesized nanoparticles**

TEM analysis was used to examine the microstructure of nanoparticles grown by the hydrothermal method. TEM micrographs in Figure 2-7 show that the primary particle size of pure  $\text{TiO}_2$  and N doped  $\text{TiO}_2$  particles are very similar (average size  $\sim 9\text{nm}$ ). When Fe is

incorporated into  $\text{TiO}_2$ , the particle size slightly decreases. Fe doped and Fe/N co-doped  $\text{TiO}_2$  have the average particle size of 8nm. This indicates that all  $\text{TiO}_2$  samples have comparable surface area and provide a similar amount of reaction sites on their surface.

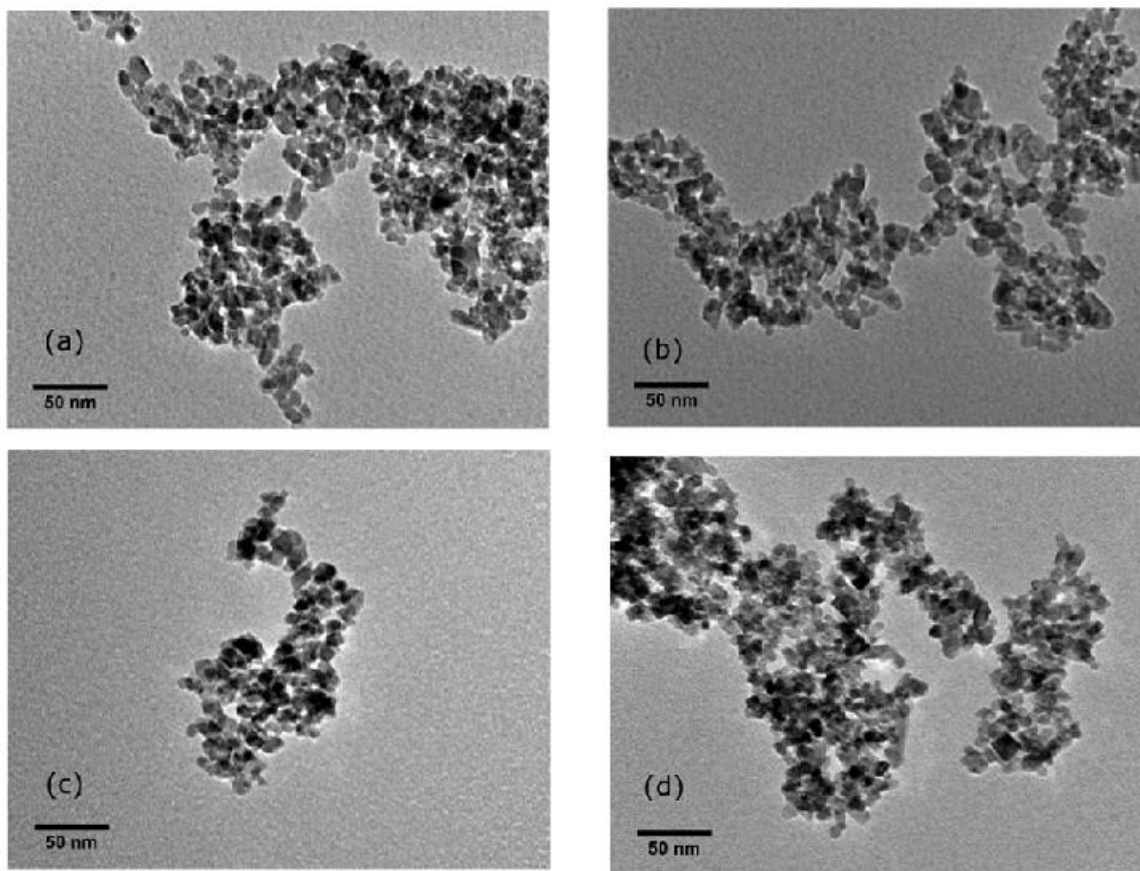


**Figure 2-7 TEM micrographs of (a) pure  $\text{TiO}_2$  (b) Fe-doped  $\text{TiO}_2$  (c) N-doped  $\text{TiO}_2$  and (d) N/Fe-codoped  $\text{TiO}_2$**

Figure 2-8 shows the optical absorption spectra of pure and doped  $\text{TiO}_2$  nanoparticles. Pure  $\text{TiO}_2$  nanoparticles show a dramatic decrease between 300 and 350 nm, which is consistent with the well-known band gap of anatase  $\text{TiO}_2$  bulk. In doped  $\text{TiO}_2$  nanoparticles, however, absorbance increased significantly in visible light region. The shift in the absorption band edges

of the doped TiO<sub>2</sub> samples indicates that the optical bandgap decreases in the order of N doped TiO<sub>2</sub>, Fe-doped TiO<sub>2</sub>, and N/Fe co-doped TiO<sub>2</sub>.

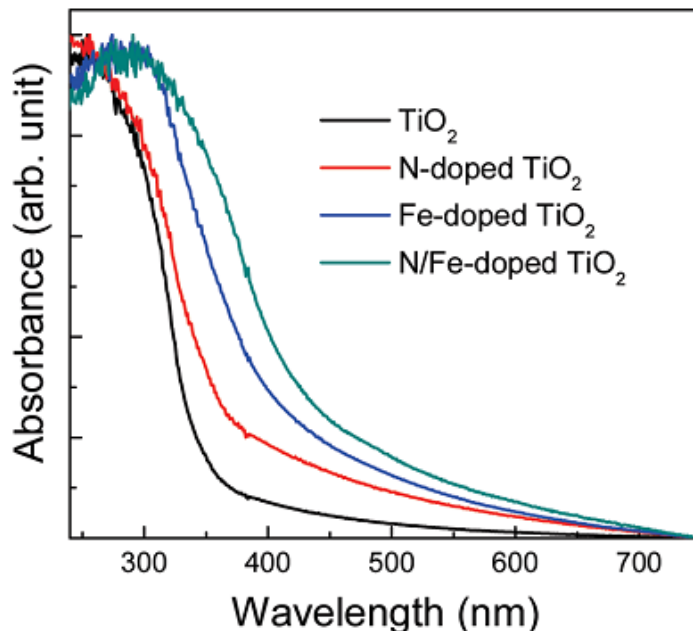


**Figure 2-8 Absorption spectra of pure and doped TiO<sub>2</sub>**

Photocatalytic characteristics of pure and doped TiO<sub>2</sub> nanoparticles are evaluated by measuring the decomposition of rhodamine B (Rh. B). Figure 2-9 shows the relative amount of Rh. B in TiO<sub>2</sub> suspended solution as a function of light illumination time. Under UV light irradiation, pure TiO<sub>2</sub> and N-doped TiO<sub>2</sub> exhibit comparable photocatalytic activities. In contrast, the decomposition reaction of Rh. B by UV light became very inefficient in Fe-doped and N/Fe co-doped TiO<sub>2</sub>. When the samples were exposed to simulated solar spectrum, a remarkable difference in the decomposition was observed among the doped samples. The amount of decomposed Rh. B increased two times by replacing pure TiO<sub>2</sub> with N-doped TiO<sub>2</sub>, which could be explained by the narrower bandgap of N-doped TiO<sub>2</sub>. However, Fe/N co-doped TiO<sub>2</sub> whose band gap is smaller than N-doped TiO<sub>2</sub>, still show the poor decomposition rate. This inconsistency between the absorption spectra and photocatalytic characteristics imply that the



effect of the doping on the light absorption is not a single factor determining the photocatalytic property of doped TiO<sub>2</sub>.

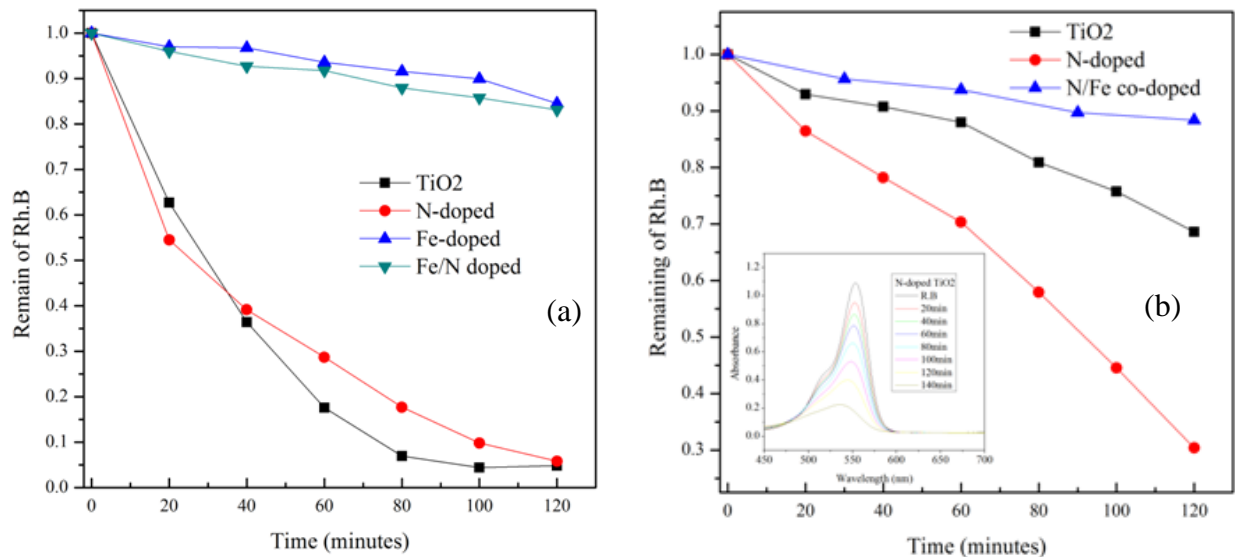


**Figure 2-9** Relative concentration of Rh. B as a function of illumination time; (a) under UV light, (b) under simulated solar light (an inset shows a gradual change in absorption spectra of N-doped sample)

The photocatalytic reaction of TiO<sub>2</sub> is related to the formation of highly reactive hydroxyl radicals on the surface of nanoparticles rather than direct reaction with photogenerated carriers. To examine the origin of different photocatalytic capabilities of pure and doped TiO<sub>2</sub> nanoparticles, the production of hydroxyl radicals was monitored by adding TA fluorescence probe into aqueous solutions. Since TA reacts with hydroxyl radicals to generate highly fluorescent hydroxy terephthalic acid (TAOH), the amount of hydroxyl radicals can be quantified by measuring the fluorescence of TAOH. As shown in Figure 2-10 (a), fluorescence intensity dramatically increases as the aqueous solution of pure TiO<sub>2</sub> is exposed to UV light. Figure 2-10 (b) shows the evolution of the fluorescence intensity of TAOH as a function of light illumination time. One distinguished characteristic in Figure 2-10 (b) is that the fluorescence intensity of Fe-

doped and N/Fe co-doped TiO<sub>2</sub> decreased almost by two orders, compared to that of pure TiO<sub>2</sub>. This large disparity indicates that Fe doping prevents photogenerated carriers from producing hydroxyl radicals, which agrees with the poor photocatalysis in Fe-doped and N/Fe co-doped TiO<sub>2</sub>.

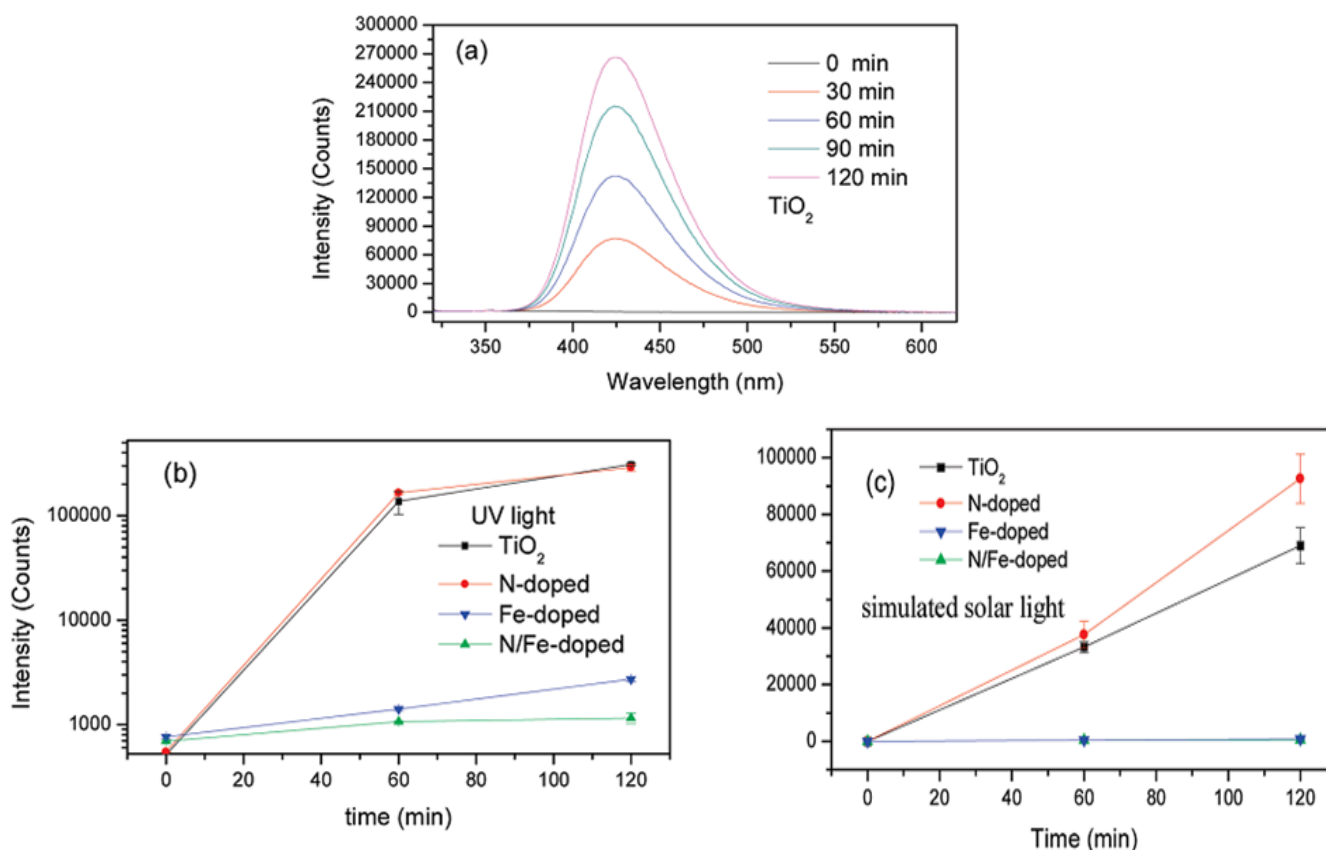


**Figure 2-10 TA fluorescence probe test; (a) luminescence spectra of TiO<sub>2</sub> dispersed TA solution under UV light, (b) change in the luminescence intensity of the solutions dispersed with four types of TiO<sub>2</sub> under UV light, (c) change in the luminescence intensity of the solutions dispersed with pure and N-doped TiO<sub>2</sub> under simulated solar light**

A change in the fluorescence intensity of TAOH in pure TiO<sub>2</sub> and N-doped TiO<sub>2</sub> dispersed solutions under simulated solar light is shown in Figure 2-10 (c). After the solution was reacted for 120 min, the fluorescence intensity of TAOH was increased in N-doped TiO<sub>2</sub> dispersed solution. A stronger fluorescence of TAOH of N-doped TiO<sub>2</sub> is consistent with the enhanced decomposition of Rh. B by simulated solar light observed in Figure 2-9. For Fe-doped TiO<sub>2</sub> and

N/Fe co-doped TiO<sub>2</sub>, the fluorescence of TAOH did not well evolved even under UV light. This indicates that a gain in the light absorption by the small bandgap of Fe-doped TiO<sub>2</sub> and N/Fe co-doped TiO<sub>2</sub> does not lead to the production of more hydroxyl radicals.

Photocatalysis of TiO<sub>2</sub> is determined by several steps including charge carrier generation, carrier trapping, electron-hole recombination, and interfacial charge transfer<sup>82</sup>. To improve the photocatalytic performance, photoexcited carriers need to be transferred to the surface of TiO<sub>2</sub> nanoparticles and form redox radicals with the carrier trapping and electron-hole recombination being minimized. Defect levels introduced by impurity doping can affect these important steps of the photocatalysis by changing the amount of absorbed light and the ratio of radiative/non-radiative recombination. The introduction of N ions into TiO<sub>2</sub> changes the band gap and carrier path of TiO<sub>2</sub>. Asahi *et al.* suggested that N 2p level could mix with O 2p level and increase the maximum energy level of its valence band by the coupling of the O 2p and N 2p orbitals<sup>62</sup>. However, recent experimental and theoretical studies show that N doped into TiO<sub>2</sub> makes a localized energy level between conduction band and valence band<sup>83</sup>. This difference comes from the location of doped N in TiO<sub>2</sub> lattice<sup>84</sup>. When N substitutes for O of TiO<sub>2</sub>, N creates a shallow acceptor state right above the valence band. In contrast, interstitially doped N forms a bond with O, leading to an isolated impurity level in the middle of the forbidden bandgap. At the same time, nitrogen doping can reduce the oxygen vacancy forming energy greatly and oxygen vacancy that is located below conduction band (0.71eV~1.18eV<sup>85</sup>) is formed relatively easily<sup>86</sup>.

The status of doped N in TiO<sub>2</sub> nanoparticles was examined by measuring the binding energy of N. XPS spectrum (Figure 2-11 a) shows that the N1s band is centered at around 400eV for N-doped sample. Although there is some dispute for the assignment of XPS spectra<sup>86</sup>, it is generally accepted that the binding energy of substitutional N and interstitial N is 396eV and

400eV, respectively<sup>62,87</sup>. A peak of 400eV in Figure 2-11 indicates that N is incorporated into the interstitial site during the hydrothermal growth of TiO<sub>2</sub> nanoparticles. A comparison of XPS and UV/Vis data also attests that interstitial N that is hydrothermally doped into TiO<sub>2</sub> nanoparticles allows for the decrease in the optical bandgap. In addition, the photocatalytic performance and TA fluorescence in Figure 2-9 and Figure 2-10 show that N in the interstitial state does not change the surface charge transfer, carrier trapping and electron-hole recombination behaviors of pure TiO<sub>2</sub>, leading to the significant improvement of the photocatalytic efficacy in visible range<sup>83,88</sup>. Comparing N1s peak between N-doped and N/Fe codoped samples, it is found the N1s has a slight shift to lower binding energy for co-doped sample. This shift indicates the electronic interaction of N with other ions in co-doped sample is different from that in N-doped one, implying the successful modification of TiO<sub>2</sub> lattice by Fe substitution.<sup>74</sup>

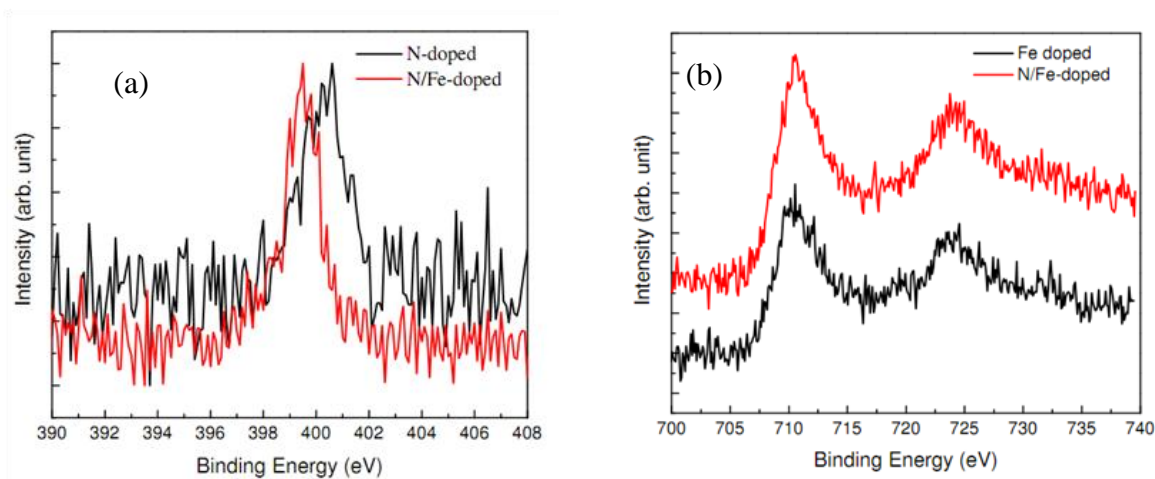


**Figure 2-11 XPS spectra of N1s (a) and Fe2p (b)**

Fe doping status is examined with Fe2p XPS spectrum (Figure 2-11 (b)). Fe 2p<sub>3/2</sub> peaks locate at 710.4eV and 710.5eV for Fe-doped and N/Fe-doped TiO<sub>2</sub> respectively, which is a little

smaller than Fe 2p<sub>3/2</sub> in Fe<sub>2</sub>O<sub>3</sub>. It is reported that this low energy shift is contributed to the Fe-O-Ti formation after doping<sup>74</sup>. It is worth to mention that there is no Fe-N bond (around 707eV<sup>89,90</sup>), which will come with iron oxynitride if doping is not fulfilled. Furthermore, the area of co-doped Fe2p peak is larger than that of Fe-doped sample, indicating the proposed synergic codoping takes effect.

An adverse effect of Fe doping on the photocatalysis under both UV light and simulated solar light is intriguing. Since the Fe and N/Fe doped nanoparticles have similar particle size, the effect of surface area is negligible. A decrease in TA fluorescence of Fe and N/Fe doped TiO<sub>2</sub> implies that Fe doping may modify the surface charge transfer and carrier trapping behaviors by changing the band gap structure of TiO<sub>2</sub>. Yamashita<sup>91</sup> reported the band gap narrowing by Fe implantation, and their ab initio molecular orbital calculation shows the overlapping of Fe (d) orbital with Ti (d) orbital decrease the minimum energy level of the conduction band. In addition, Moser *et al.*<sup>92</sup> demonstrated that the doping of Fe(III) can inhibit the electron-hole recombination since Fe(III) plays a role of a shallow trap via the transition from Fe(III) to Fe(IV), and boost the photocatalytic reaction. In contrast to previous studies, Fe-doped or N/Fe co-doped samples in this study exhibit poor photocatalytic property even though their bandgaps have been significantly narrowed. TA fluorescence experiment supports that doped Fe suppresses the transfer of photogenerated charges to the surface of nanoparticles and decreases the redox reactions producing hydroxyl radicals. This implies that the energy levels of doped Fe may trap the photogenerated electrons and promote the radiative electron-hole recombination. Mizushima *et al.*<sup>93</sup> have proposed Fe<sup>3+</sup> and Fe<sup>2+</sup> energy levels are located near a valence band and a conduction band, respectively. The ab initio band calculation based on the density function theory from Umebayashi *et al.*<sup>94</sup> demonstrated Fe t<sub>2g</sub> level is located 0.2 eV above the valence

band and Fe  $e_g$  level is split into  $d_{z^2}$  and  $d_{x^2-y^2}$  orbitals which extend the conduction band to some degree. It is reasonable to propose that Fe doping can trap both hole and electrons based on the band gap structure. As the amount of doped Fe increases, chances for the recombination of trapped electrons and holes also increases and photocatalytic efficacy decreases according to Zhang, *et al.*<sup>82</sup>. They showed that there is an optimum Fe(III) dopant concentration, and this concentration will decrease with increasing particle size. They argued that the shallow trapping, which can be thermal excited, is critical. The high doping concentration will result in the recombination of hole and electrons through quantum tunneling or low mobility of excited carriers. Other reports show the similar dependence on the doping concentration. Nagaveni *et al.*<sup>50</sup> observed the negative effect of  $Fe^{3+}$  doping in  $TiO_2$  prepared by the solution combustion method when the doping level is at the range of 2.5~10 atomic .%. Shah *et al.*<sup>61</sup> indicates that 1 atomic % of  $Fe^{3+}$  in  $TiO_2$  is detrimental to photocatalytic property.

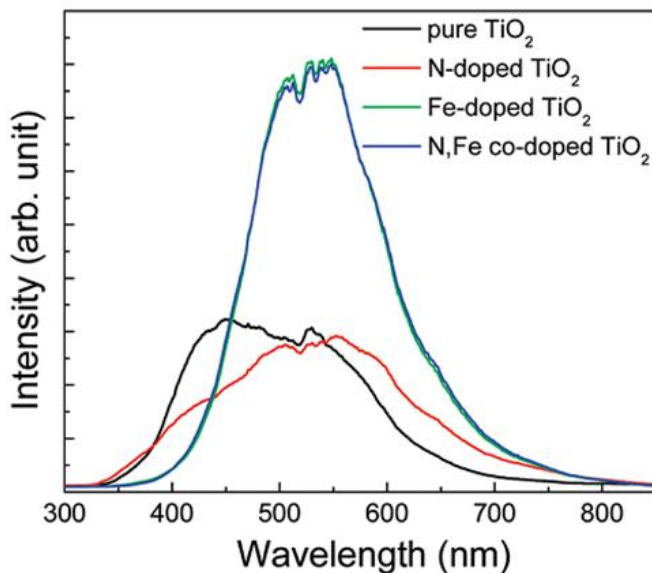


**Figure 2-12** Photoluminescence spectra of pure, N-doped, Fe-doped, and N/Fe codoped  $TiO_2$  at 10K

Photoluminescence (PL) of pure and doped TiO<sub>2</sub> samples was measured at 10 K to characterize the effect of doping on the radiative recombination of electron-hole pairs. Broad PL spectra were observed in all samples, as shown in Figure 2-12. The intensity and wavelength of PL spectra are sensitive to the doping of aliovalent ions. PL spectra of Fe-doped and N/Fe co-doped TiO<sub>2</sub> have larger intensity than those of pure and N-doped TiO<sub>2</sub>, which implies the electron-hole recombination rate is much higher in Fe-doped and N/Fe co-doped TiO<sub>2</sub> than in pure and N-doped TiO<sub>2</sub>. Further information on the nature of the energy band modification can be obtained by observation of the spectral shift. When the dopants are incorporated into TiO<sub>2</sub>, red shift of PL spectra is observed. This is qualitatively consistent with the change in the optical absorption spectra in Figure 2-8. It is noted that PL spectra of Fe-doped and N/Fe co-doped TiO<sub>2</sub> samples are very similar, which means the overwhelming effect of Fe-doping in term of carrier radioactive recombination. The dominant effect of Fe doping indicates that the electrons trapped in Fe defect levels are recombined with the holes in the valence band or defect levels, instead of the holes trapped in the isolated defect levels associated with N doping. This shows that the high concentration of localized Fe defect levels in TiO<sub>2</sub> do not contribute to the photocatalysis, since the defect levels provide a by-pass to photoexcited carriers.

## 3.0 CARRIER TRANSPORT MANIPULATION

### 3.1 BACKGROUND

#### 3.1.1 Motivation of 1-D nanostructure for photoanode

The photoanode of DSSC is mainly the mesoporous film of TiO<sub>2</sub> nanoparticles on which a monolayer of the sensitizing dyes is coated. Mesoporous TiO<sub>2</sub> photoanodes, which have the percolated links of the nanoparticles, produce very large photocurrent because of their high surface area and well matched energy level. These surfaces are suitable for dye adsorption and its electron energy level matching allows the efficient injection of carriers from dye molecules to nanostructured TiO<sub>2</sub> films.<sup>12</sup> In spite of this advantage of the nanoparticle based photoanodes, their numerous interparticle boundaries easily trap the charge carriers, which results in decrease in the carrier mobility and the carrier lifetime. In nanoparticle based DSSCs, therefore, the carrier transport is a trap-limited diffusion process and the electron diffusion coefficient is several orders of magnitude smaller than the expected value which is deduced from the physical properties of the single crystalline bulk TiO<sub>2</sub>.<sup>95</sup> To compensate for the slow carrier transport of the nanoparticle based photoanodes, extensive research efforts have been placed on modifying the internal microstructure of the photoanodes.<sup>22,96,97</sup>



Nanowire/nanorods have demonstrated a great potential of achieving high diffusion coefficient of carriers in electric devices, because of their unique one-dimensional (1-D) structure.<sup>22</sup> When a nanoparticle-based photoanode of DSSC is substituted with the nanorods-based photoanode, it is expected that the nanorods will provide a ballistic pathway for the carriers and enhance the carrier transport. In nanoparticle-based DSSCs, carrier transport mostly is through simple diffusion instead of drift force under built-in potential as in silicon solar cells. To conserve charge neutrality, cations in electrolyte make a corresponding movement through porous nanoparticle networks as electrons diffuse to the anode direction, and it is a type of ambipolar diffusion. The mobility of electrons usually is faster than that of cations, but electric field built from the position difference between electrons and cations will slow down the movement of electrons and eventually maintain equilibrium. In nanorod photoanodes, it is expected that the existence of radial and axial fields will guide electrons to go through nanorod and the ambipolar diffusion mode may be not valid.

It is reported that the stable high fill factor (FF) and increasing short circuit current as the length of TiO<sub>2</sub> nanowire gets longer arise from the elongated lifetime of the carriers.<sup>98</sup> Kang et al. analyzed the effect of short nanorod based electrodes on DSSCs, and reported enhanced carrier lifetime when the aspect ratio of the individual nanoparticles increases.<sup>99</sup> In contrast to the carrier lifetime, the improvement of the carrier transport has not been clearly observed in the nanorod based DSSCs. This is due to the unique microstructure of the nanowires grown by an oriented attachment technique, which includes locally formed necks and sudden turns in the electron path.<sup>100,101</sup>

Enache-Pommer has examined carrier transport in single crystal ZnO nanowire, TiO<sub>2</sub> nanoparticles, polycrystalline TiO<sub>2</sub> nanowire, and single crystalline rutile nanowire.<sup>102</sup> The

transport rate of carriers in ZnO nanowire is independent of illumination light, and is at least two orders faster than recombination rate. The transport time of polycrystalline TiO<sub>2</sub> nanowires exhibit a similar power law dependence of illumination intensity as that of nanoparticles, although the ratio of recombination time to collection time is much larger than that in nanoparticles. It has been expected that single crystalline TiO<sub>2</sub> may make a difference. In contrast, for the single crystalline rutile nanorods, it is reported that the carrier transport is slower for the rutile nanorod than for the anatase P25 particles.<sup>103</sup> However, the previous studies do not compare the carrier transport and recombination behaviors in the nanorods and nanoparticles with the same crystalline phase and a controlled microstructure.

TiO<sub>2</sub> nanowire/nanorods have been synthesized using several methods, such as chemical vapor deposition (CVD)<sup>104</sup>, physical vapor deposition (PVD)<sup>105,106</sup>, vapor-liquid-solid growth (VLS)<sup>107</sup>, templated sol-gel method<sup>108</sup>, and, mostly, hydrothermal reaction with an assistance of surfactant and copolymer<sup>98,99,101</sup>. Recently, single crystalline TiO<sub>2</sub> nanorods with a rutile phase have been successfully grown on the top of fluorine-doped tin oxide (FTO) films coated glass, by a hydrothermal method.<sup>109,110</sup> Because the single crystalline rutile nanorods grown by this method are in a direct contact with the FTO film, no complicated procedure is needed to form the bottom electrode for subsequent device fabrication. The preferential adsorption of chlorine ions on different crystallographic planes allows for the selective hydrolysis of titanium alkoxide on the highly textured FTO, which results in the single crystalline nanorods. While the hydrothermal reaction provides high crystalline rutile nanorods, the time to grow a few micrometer long nanorods ranges from several hours to days. From a viewpoint of the nanorod growth, it is of importance to find a way to increase the growth rate for the widespread use of the nanorods.

In this study, we explored the combined use of the microwave (M-W) heating and the hydrothermal reaction to accelerate the growth of the single crystalline rutile nanorods. It is known that the microwave hydrothermal method provides a fast ramping rate and faster reaction kinetics during the crystallization process, compared with the conventional hydrothermal methods.<sup>111</sup> This method has been already applied to synthesizing TiO<sub>2</sub> colloidal particles.<sup>111-113</sup> The use of M-W in growing the nanorods increased the growth rate of the nanorods. In addition, due to the volumetric heating effect of the microwave reaction technique, the arrays of the nanorods were very uniform. The nanorods grown via the M-W assisted hydrothermal reaction, were used to fabricate DSSCs. In the fabrication process, the surface of the rutile nanorods was modified by coating the rutile thin layer to control the surface area and the electron transport path. In the nanorod based DSSCs, we systematically investigated the electron diffusion coefficient and lifetime with an emphasis on the role of the surface coating.<sup>20</sup> In the nanowire based DSSCs, the energy conversion efficiency is mainly influenced by a complex function of the electron mobility and the surface area and the effect of the carrier recombination is limited.

### **3.1.2 Carrier transport model in DSSC**

As shown in Figure 1-6, carrier transport is a complex process in DSSCs. In conventional DSSCs, electron/hole pairs are generated in a dye sensitizer, and the electrons and holes move in the TiO<sub>2</sub> nanoparticle network and the electrolyte, respectively. In the TiO<sub>2</sub> nanoparticle matrix, carrier transport can be described as ambipolar transport.<sup>114</sup> Ambipolar transport typically refers to a situation where an electric carrier is injected into a sea of oppositely charged mobile carriers. In DSSCs, there are plenty of cations in the electrolyte (majority carriers), and the injected electrons in TiO<sub>2</sub> photoanode are the minority carrier. For a 0.5M electrolyte, the concentration

of ions is  $10^{20} \text{ cm}^{-3}$ , while the photo-excitation density observed experimentally is around  $10^{18} \text{ cm}^{-3}$ . In the mesoporous  $\text{TiO}_2$  network, the cations can reach the surface of the photoanode and screen the negative charge of electrons. In addition, the transport of the electrons is coupled with the motion of cations, and the effective diffusion coefficient can be described as follow:

$$D_{amb} = \frac{n+p}{n/D_p+p/D_n} \quad (3-1)$$

Where  $n$  is electronic density,  $p$  is positive charge density, and  $p \gg n$  in DSSC. The above equation can be reduced to,

$$D_{amb} = D_n \quad (3-2)$$

Eqn 3-2 demonstrates that the effective diffusion coefficient in DSSC is determined by the electron transport in a photoanode. The electron transport in  $\text{TiO}_2$  is significantly influenced by traps (bulk, surface). The electron trapping states,  $g(E)$  are often described as an exponential distribution:

$$g(E_t) = \frac{N_{t,0}}{k_B T_0} \exp\left(-\frac{E_c - E_t}{k_B T_0}\right) \quad (3-3)$$

Here,  $N_{t,0}$  is the total trap density (typically  $10^{19}$ - $10^{20} \text{ cm}^{-3}$ ), and  $T_0$  is a characteristic temperature, usually much higher than room temperature. Figure 3-1 shows the distribution of density of states below the conduction band with blue short lines representing the trapping sites. In a dark condition, the Fermi level in  $\text{TiO}_2$  is the same as redox level in the electrolyte, while the Fermi level is elevated to a quasi-fermi level ( $nE_F$ ) as electrons fill the trapping sites above the redox level. An equilibrium of electron distribution and the total number of electrons in trapping sites under illumination can be described as the integration of  $g(E)$  and the Fermi-Dirac function over all energy domains:

$$n_t = \int_{-\infty}^{\infty} \frac{1}{1 + \exp\left(\frac{E_c - nE_F}{k_B T}\right)} g(E) dE \quad (3-4)$$

If the Fermi-Dirac distribution is a step function, the change in the number of trapped electrons under illumination can be estimated by changing the integration boundary from  $E_F$  to  ${}_nE_F$ . This change is schematically shown as the shaded area in Figure 3-1. The number of electrons in a conduction band is noted as  $n_c$ , which has the following relation:

$$n_c = N_c \exp\left(-\frac{E_c - {}_nE_F}{k_B T}\right) \quad (3-5)$$

where  $N_c$  is the density of conduction band states.

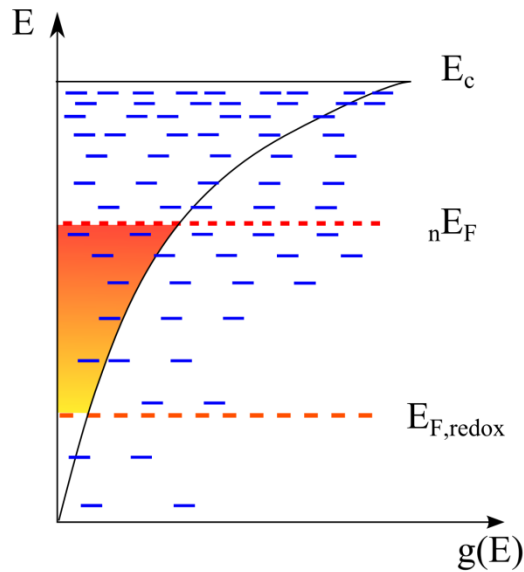


**Figure 3-1 Density of state function vs energy below conduction band**

The most popular model of electron transport in  $\text{TiO}_2$  is a multiple-trapping model as shown in Figure 3-2.<sup>115,116</sup> Electrons travel at the conduction band, but they are influenced by the trapping sites between the conduction band and the quasi-Fermi level. Electrons are trapped and de-trapped during the transport and their effective diffusion coefficient can be described as,

$$D_n = \left(1 + \frac{\partial n_t}{\partial n_c}\right)^{-1} D_0 \quad (3-6)$$

where  $D_0$  is the diffusion coefficient of the free electrons which are not trapped. The derivative of  $n_t$  with respect to  $n_c$  shows the effect of trapping and de-trapping on the electron diffusion.

Combining Eqn. 3-4 and 3-5, we can get the derivative

$$\frac{\partial n_t}{\partial n_c} = g(nE_F) \frac{k_B T}{n_c} \propto \exp\left[-\frac{nE_F}{k_B} \left(\frac{1}{T} - \frac{1}{T_0}\right)\right] \quad (3-7)$$

Eqn. 3-7 indicates that a higher quasi-Fermi level results in a higher diffusion coefficient.

From another perspective: a smaller amount of trapping sites between the conduction band edge and the quasi-Fermi level could reduce the chance of trapping and de-trapping.

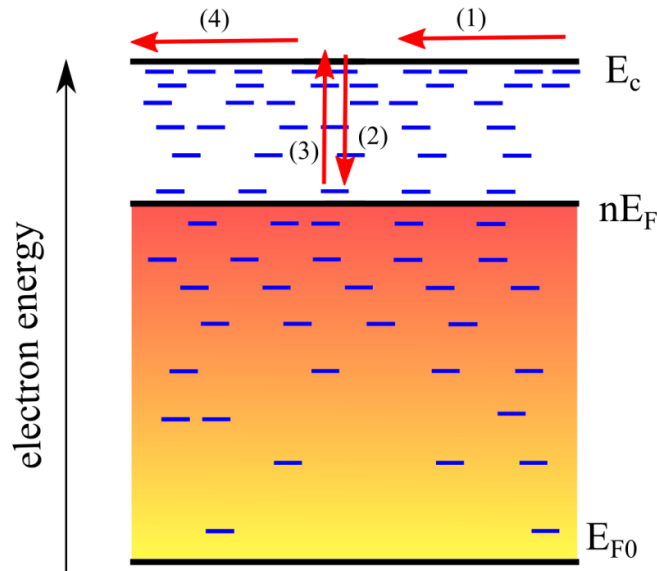


**Figure 3-2 Schematics of multiple-trapping model**

A few years ago, another model, namely the hopping model, was proposed by Prof. Juan Bisquert.<sup>117,118</sup> In this model, electrons jump from one trapping site to another trapping site directly, and especially around the vicinity of special energy called transport energy, or  $E_{tr}$ , as shown in Figure 3-3. The assumption of transport energy is valid in a system with heavily localized states. The energy difference between  $E_{tr}$  and  $E_c$  is:

$$\Delta E_{tr} = 3k_B T \ln\left[\frac{3\alpha T_0}{2\alpha T} \left(\frac{4\pi}{3}\right)^{1/3}\right] \quad (3-8)$$

where  $\alpha$  is localized radius of trap site, and  $a$  is the mean distance between localized sites that is equal to  $(N_{t,0})^{-1/3}$ . The diffusion coefficient in this model is determined by the following equation:

$$D_n = \frac{9T_0^3}{4T^3} \left(1 - \frac{T}{T_0}\right) \exp \left[-3 \frac{T_0}{T} - (E_{tr} - nE_F) \left(\frac{1}{k_B T} - \frac{1}{k_B T_0}\right)\right] \alpha^2 \nu_0 \quad (3-9)$$

where  $\nu_0$  is the fundamental frequency, and  $T_0$  is also the characterization temperature (normally  $T_0 > T$ ).

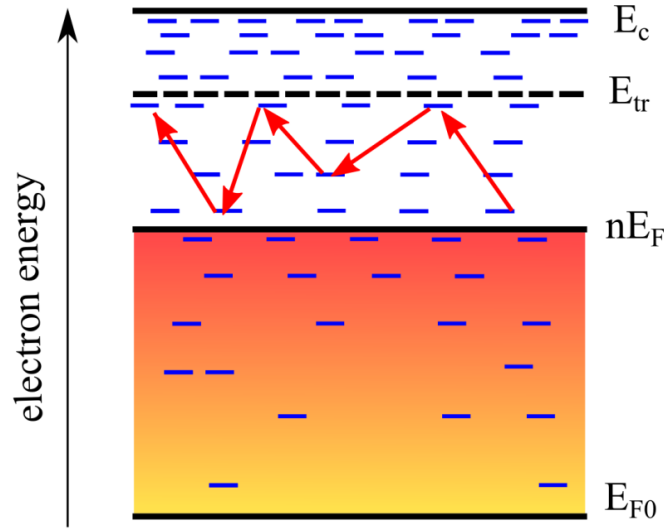


**Figure 3-3 Schematics of hopping model**

Both the multiple trapping model and the hopping model explain why the diffusion coefficient has a power law dependence on the electron concentration (i.e. the quasi-Fermi level has an effect on the diffusion coefficient). The two models predict different diffusion coefficients as temperature deviates from room temperature. However, it is not easy to measure the properties of DSSCs at high temperature due to the volatile liquid electrolyte.

### 3.1.3 SLIM-PCV method

Several techniques are available to measure charge transport in DSSCs. These include open-circuit voltage decay (OCVD)<sup>119,120</sup>, intensity-modulated photovoltage/photocurrent spectroscopy (IMVS/IMPS)<sup>121,122</sup>, electrochemical impedance spectroscopy (EIS)<sup>123,124</sup>, and stepped light-induced transient measurements of photocurrent and photovoltage (SLIM-PCV)<sup>125,126</sup>. These measurements can be briefly summarized in Table 3-1. SLIM-PCV has been widely used to probe the diffusion coefficient and lifetime due to its simplified optical setup and fast measurement.<sup>24,125,127-129</sup>

**Table 3-1 Summary of charge transport measurement techniques for DSSCs**

Method	Input	Output	results	remarks
Electrochemical Impedance Spectroscopy (EIS)	Voltage ( $\delta\hat{V}$ )	Current ( $\delta\hat{j}$ )	$\tau_R, \tau_t$	Frequency domain
Intensity-modulated photocurrent spectroscopy (IMPS)	Photon flux ( $\delta\hat{I}$ )	Current ( $\delta\hat{j}$ )	$D_n, \tau_c$	Frequency domain
Intensity-modulated photovoltage spectroscopy (IMVS)	Photon flux ( $\delta\hat{I}$ )	Voltage ( $\delta\hat{V}$ )	$\tau$	Frequency domain
Step-light induced transient measurement of photocurrent (SLIM-PC)	Photon flux ( $\delta\hat{I}$ )	Current ( $\delta\hat{j}$ )	$D_n$	Transient
Step-light induced transient measurement of photovoltage (SLIM-PV)	Photon flux ( $\delta\hat{I}$ )	Voltage ( $\delta\hat{V}$ )	$\tau$	Transient
Open circuit voltage decay (OCVD)	Photon flux ( $\delta\hat{I}$ )	Voltage ( $\delta\hat{V}$ )	$\tau$	Transient

\*  $\tau_t$  is transport time,  $\tau_R$  is recombination time,  $D_n$  is diffusion coefficient,  $\tau$  is life time.

SLIM-PCV is a perturbation measurement using a stepwise change in light intensity. The basic measurement principle is to monitor the change of photocurrent and voltage under this perturbation. The measurement setup is shown in Figure 3-4. Monochromatic light from a laser diode (660 nm wavelength) is modulated to produce a stepwise change of light intensity as



performed by a function generator (Agilent 33220A). To ensure a small perturbation, the drop of light intensity is controlled to be small enough comparing to the original intensity (less than 10% of the original intensity). Incoming light from the diode goes through a neutral density filter before it hits the sample. The role of the neutral density filter is to change the total intensity, since carrier transport in DSSC is a function of light intensity. Photocurrent is measured in a short circuit state, while photovoltage is measured in an open circuit state. The photocurrent is converted to voltage via a current amplifier. Voltage signals are measured by a digital oscilloscope (Tektronix, TDS2024B) that is synchronized with the function generator.

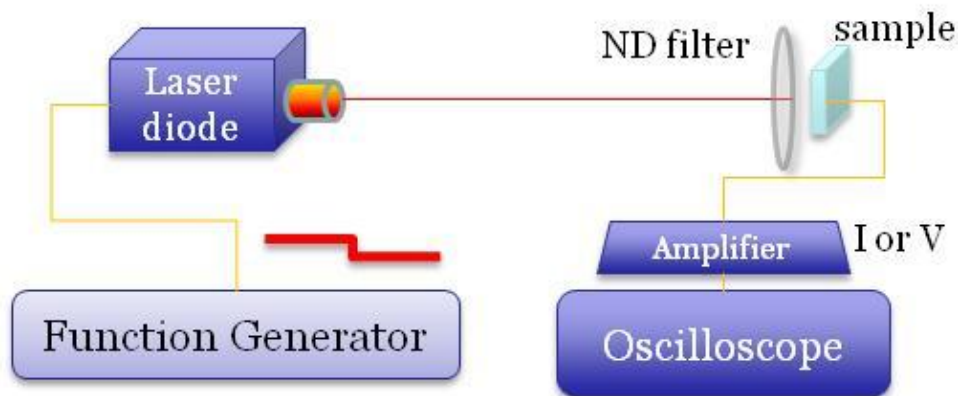


**Figure 3-4 Configuration of SLIM-PCV measurement**

From the change in photocurrent and photo-voltage as a function of time, we can obtain the basic transport parameters in the system. Figure 3-5 gives a typical experimental result of photocurrent and photovoltage change as a function of time. It is obvious that the transition curve is something like an exponential decay. These data are fitted with mathematical functions to extract the apparent diffusion coefficient and the carrier life time.

For the photocurrent-time curve, there are two steady state regions, before the light intensity is changed and after. Just after the change in light intensity, electrons diffuse to the

electrode to reach a new equilibrium electron distribution. The time needed to achieve a new equilibrium state reflects the diffusion coefficient, quantified as<sup>24</sup>:

$$D = L^2 / (2.77\tau_c) \quad (3-10)$$

where  $L$  is the thickness of  $\text{TiO}_2$  layer, and  $\tau_c$  is the exponential decay time constant in the short-circuit current decay curve.

Under the general framework of electron density rate at the open circuit condition, the electron density has the following relation<sup>24</sup>:

$$n(t) = A \exp(-\frac{t}{\tau}) \quad (3-11)$$

where  $A$  is  $\Delta n$ , the difference in electron density before and after the light intensity change. The open circuit voltage is related to the Fermi level of the  $\text{TiO}_2$  electrode and also scales with  $\log(n/n_0)$ . Under the approximation of a small perturbation (small  $\Delta n$ ),  $V_{oc}$  is proportional to Eqn. 3-11. Therefore, the fitting of the relaxation time of open circuit voltage decay enable us to obtain the apparent carrier lifetime in DSSCs.

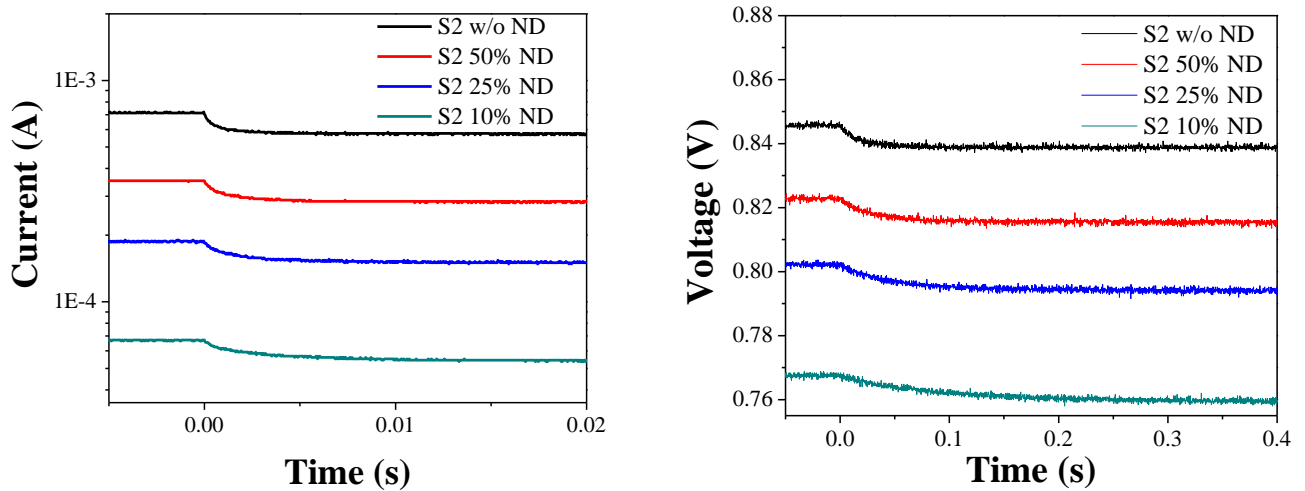


Figure 3-5 Measurement of current (a) and voltage (b) transition under a small drop of light intensity

## 3.2 SINGLE CRYSTALLINE RUTILE NANOROD ON FTO

### 3.2.1 Experiment

TiO<sub>2</sub> nanorods were grown by using a CEM microwave accelerated reactor system (MARS). 60 ml of Deionized (DI) water and 60 ml HCl were mixed with a magnetic stirrer thoroughly for 10 min, and 2 ml of titanium tetraisopropoxide (TTIP, Aldrich, 97 %) was dropped into the mixed solution. The obtained reagent solution was stirred for another 10 min, and was dispensed into four vessels equally. Bare FTO (Pilkington TEC8) or surface modified FTO substrates were immersed into solution. The microwave reaction was carried out and the effects of temperature and time were examined.

The process of the FTO surface modification is as follows. 150ml pure ethanol, 2.77 ml DI water, and 0.36ml HNO<sub>3</sub> (70 % concentration) was mixed at first, and well mixed solution was slowly poured into another beaker containing 150 ml pure ethanol and 23.04 ml TTIP to form TiO<sub>2</sub> sol. Then a thin layer of TiO<sub>2</sub> was spin-coated on top of FTO substrate with the TiO<sub>2</sub> sol.

After the microwave reaction, the TiO<sub>2</sub> nanorod grown substrates were cleaned with DI water and 0.1 M nitric acid. A part of the TiO<sub>2</sub> nanorods were treated with a TiCl<sub>4</sub> solution. TiO<sub>2</sub> nanorod grown substrates were immersed into the 0.05 M TiCl<sub>4</sub> at 50°C for 30 min or 2 hrs.<sup>103</sup> Coated TiO<sub>2</sub> nanorod arrays were washed thoroughly with DI water, and annealed at 450°C for 30 min.

TiO<sub>2</sub> nanorod substrates were immersed into 0.27 mM N719 dye (ruthenium 535-bis-TBA solaronix) for 24 hours. Dye-anchored nanorods were capped by a Pt-coated FTO. Two substrates were separated by hot-melt sealing foil (SX1170-25, solaronix) and the space between

the substrates was filled with the iodide based electrolyte (Iodolyte AN-50, solarnix). External electrodes were coated with silver paste.

The morphology of bare FTO substrates and nanorods grown FTO substrates was examined by a scanning electron microscope (XL-30, Philips) and an atomic force microscope (Multimode V, Veeco). The crystal structure of the nanorods was examined by X-ray diffractometer (X'pert diffractometer, Philips, Cu K $\alpha$  source), Raman microscope (inVia, Renishaw), and transmission electron microscope (200CX, JEOL).

The photovoltaic performance of DSSCs was obtained by measuring photocurrent density-voltage (J-V) curves under the simulated solar light. The detailed response of DSSCs to the light at different wavelengths was examined through incident photon-to-current conversion efficiency (IPCE) spectra. The surface roughness factor of the nanowire arrays was estimated using a dye desorption method.<sup>130,131</sup> Dye-anchored electrodes were placed in 1mM NaOH of ethanol/H<sub>2</sub>O (vol 50/50) solution for 2 hrs. The amount of the desorbed dye was calculated by comparing their UV/VIS spectra with Beer's law. Electron diffusion coefficient and lifetime were measured by a stepped light-induced transient measurement of photocurrent and voltage (SLIM-PCV) method as described in the previous section.<sup>24,127</sup> The light source was a 660 nm laser diode, and the impinging light was modulated by connecting a function generator (Agilent 33220A) to the laser diode. The changes in the photovoltage and photocurrent of the DSSCs were monitored by a digital oscilloscope (Tektronix, TDS2024B) and a current amplifier. During the measurement, a set of neutral density filters were used to control the light intensity. SLIM-PCV measurements have been conducted multiple times (both different sample, and multiple measurement of single sample) for every sample, and presented results are typical results.

### 3.2.2 Synthesis of rutile nanorod on FTO

In this section we will discuss of the properties of grown nanorod, growth rate, and the effect of surface modification.

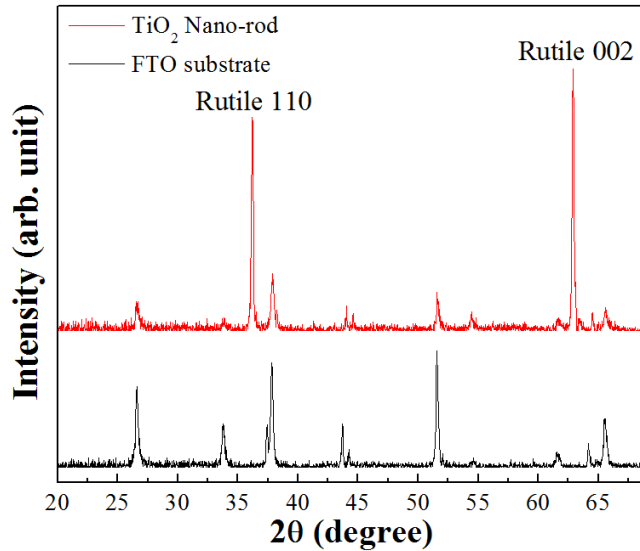
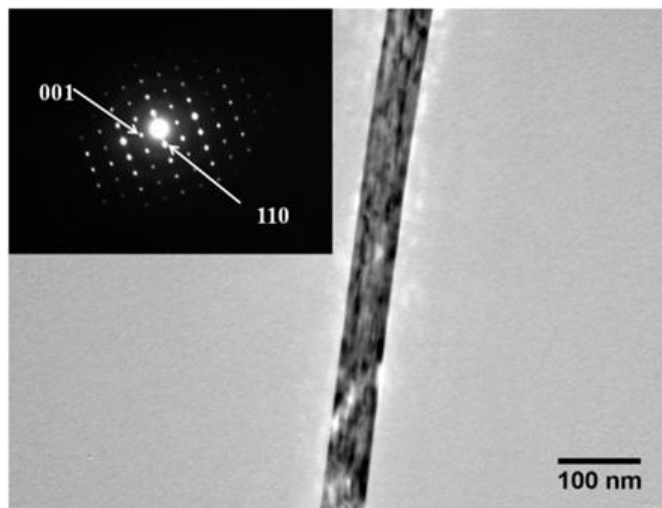


Figure 3-6 XRD diagram of TiO<sub>2</sub> nanorod on FTO substrate

Figure 3-6 shows the XRD pattern of the TiO<sub>2</sub> nanorods grown on FTO/glass substrates. Since the lattice mismatch between tetragonal FTO and the rutile TiO<sub>2</sub> is small, the rutile TiO<sub>2</sub> nanowires grow on the top of the FTO/glass substrates. After the M-W assisted hydrothermal reaction, the intensity of the peaks associated with the FTO films decreased and two strong peaks appeared. New peaks are indexed as the (110) and (002) planes of rutile TiO<sub>2</sub>, which indicates that the highly oriented rutile layer was formed on the FTO film. The microstructure and crystal phase of the nanorods were also examined by TEM. As presented in the Figure 3-7, the typical width of the nanorod is around 50 nm. A selected area diffraction (SAD) pattern in the inset of Figure 3-7 shows that the nanorod is single crystalline and its growth direction is [001], which is consistent with the results of XRD analysis.



**Figure 3-7 TEM image of TiO<sub>2</sub> nanorod in a bright field mode; an inset shows the selected area diffraction pattern of the nanorod**

To carefully examine the growth rate of the rutile nanorods, a series of nanorod growth experiments were conducted as a function of the growth time (10min, 30min, 50min, and 100min). As shown in Figure 3-8, both width and length of the nanorods increase with reaction time. The growth rate of the nanorods is plotted in Figure 3-9. It is noted that the growth rate of the nanorods in the M-W assisted hydrothermal reaction is much faster than in the conventional hydrothermal reaction. When the nanorods were grown at 195°C for 50 min in the M-W reactor, the nanorods were as long as 4  $\mu\text{m}$ . In the purely hydrothermal reaction, the growth of the nanorods with the same length needs more than 10 hrs. This accelerated reaction rate is traced to the unique heating mechanisms of the microwave assisted reaction, such as volumetric heating. The microwave can penetrate into the sub-surface region of the growing materials, deposit energy, and cause the volumetric heating. This is different from the conventional heating where the material is heated through the conduction from the surface.<sup>132</sup> The volumetric heating makes it possible to achieve a rapid and uniform reaction in the nanowire films. In addition, the strong electric field of the microwave can induce a non-linear driving force for the movement of dipoles

near the surface of the nanowires in the precursor solution, which improves the reaction kinetics.<sup>133</sup>

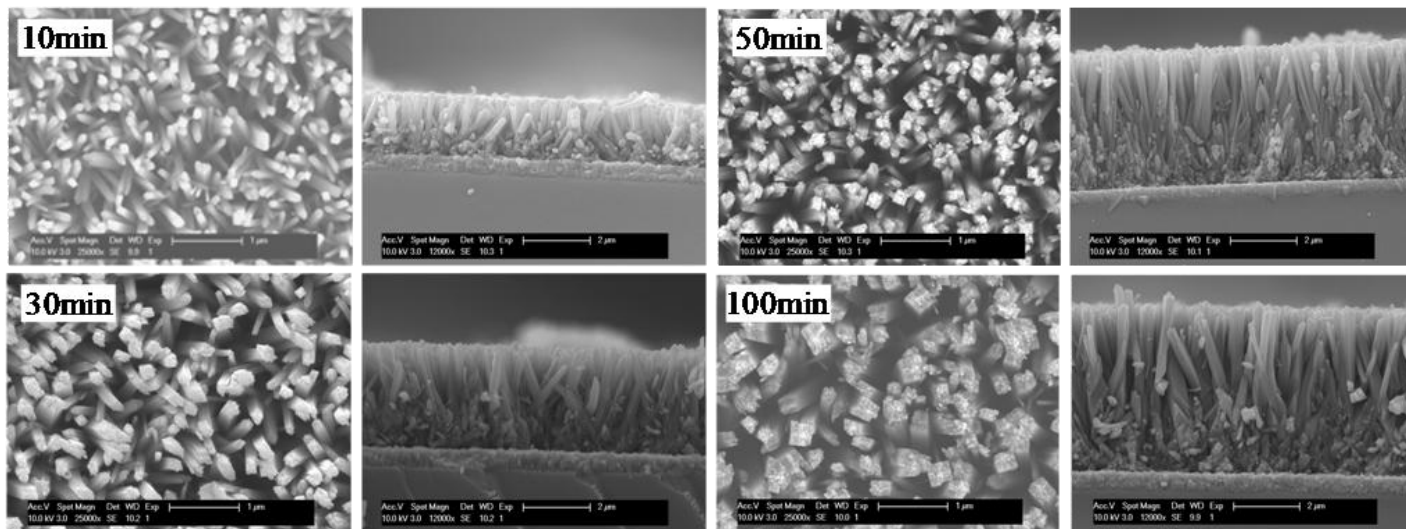


Figure 3-8 SEM image of TiO<sub>2</sub> nanorod at different reaction time (10 min, 30 min, 50 min, 100 min)

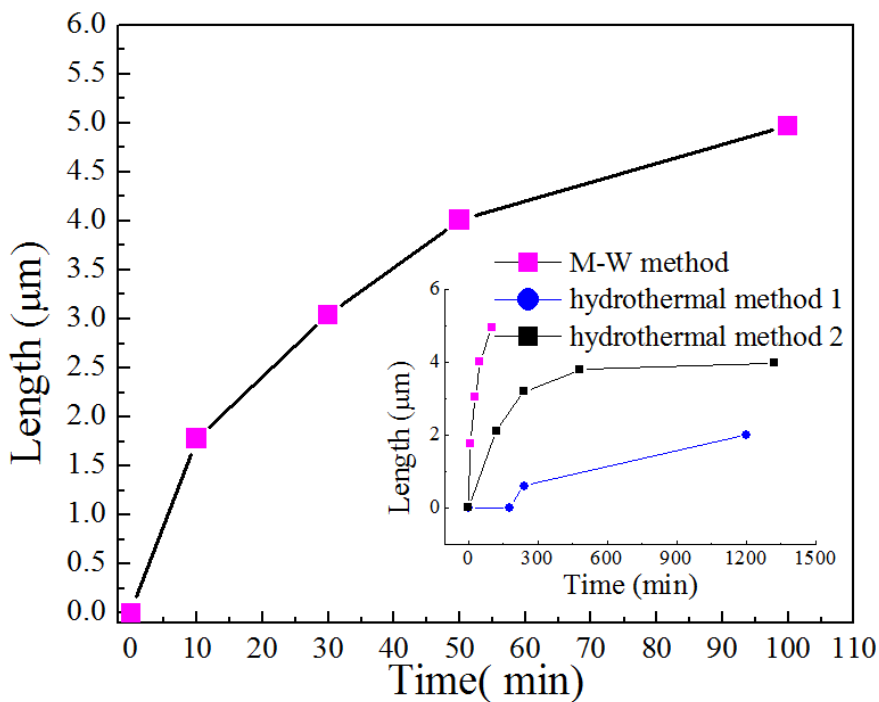
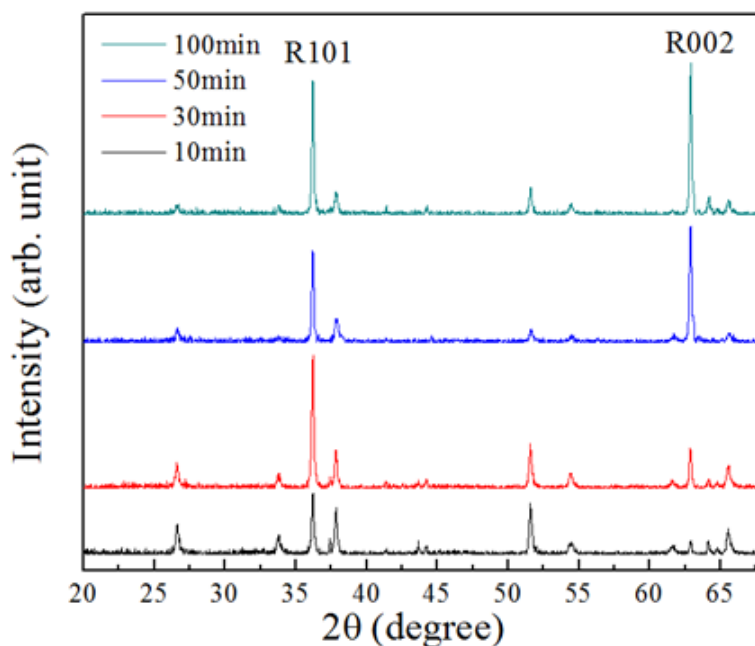


Figure 3-9 Growth rate of TiO<sub>2</sub> nanorods during a microwave assisted hydrothermal reaction; an inset indicates the growth rate of a conventional hydrothermal reaction in literature

Figure 3-10 shows the change in the XRD patterns as a function of the growth time. The intensity ratio of (002) peak over (101) peak represents the degree of the alignment of the rutile nanorods. The higher intensity of the (110) peak indicates that the nanorods are more randomly oriented at the early stage of the growth. As the reaction time increases, the growth of the oblique nanorods is retarded and the well aligned arrays of the vertical nanorods bury the oblique nanorods. Therefore, the relative intensity of (002) increases as the growth time increases. This explanation on the change in the orientation of the nanorods is supported by SEM micrographs in Figure 3-8.



**Figure 3-10 XRD patterns of TiO<sub>2</sub> nanorod grown at 195°C for different reaction times (10 min, 30 min, 50 min, and 100 min)**

Figure 3-11 presents the effect of the growth temperature on the morphology of the nanorod. To compare the change in the aspect ratio, length, and alignment, the rutile nanorods were grown at 155°C, 175°C, and 195°C for 50 min. An increase in the reaction temperature



increases both length and diameter of the nanorods. However, the growth temperature influences the length of the nanorods more than the diameter of the nanorods in the M-W assisted hydrothermal reaction; the aspect ratio of the nanorods increases from 12 to 20 with increasing growth temperature. This indicates that the nanorods grown at a relatively high temperature are suitable for their application to DSSCs due to their higher surface area.

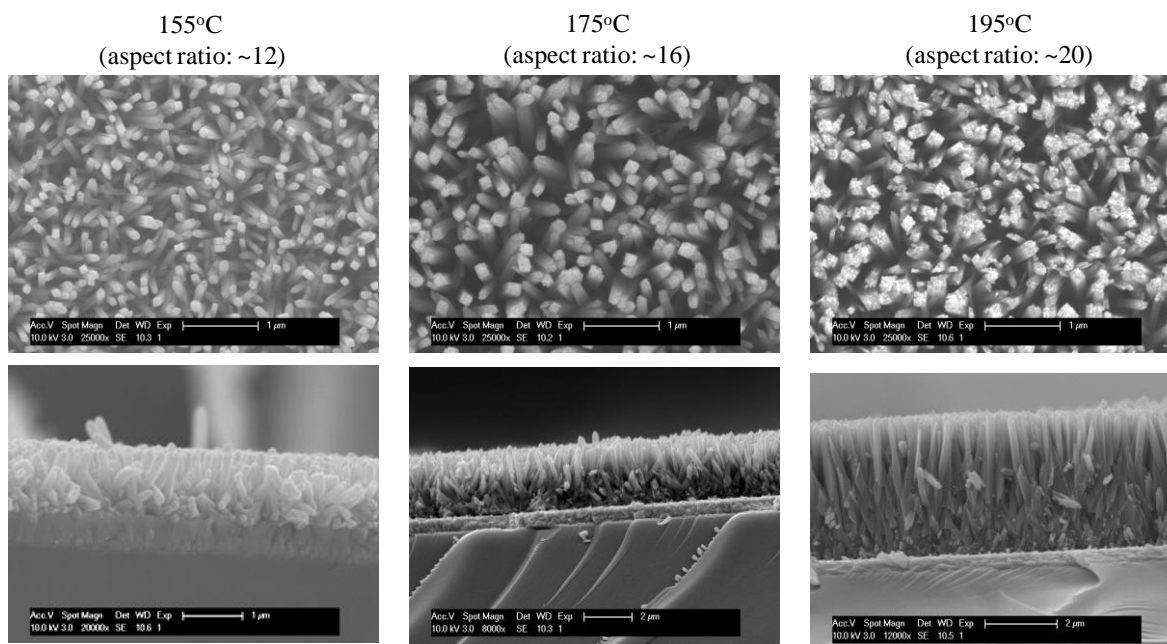


**Figure 3-11 SEM images of TiO<sub>2</sub> nanorod grown at different temperatures (155°C, 175°C, and 195°C) for 50 min**

While the rutile nanorods directly grown on the FTO/glass substrates can be easily integrated into the DSSCs, the relatively large width of the nanorods decreases the surface roughness of the nanorod arrays and the amount of the adsorbed dye, leading to inefficient light absorption. The relatively large width of the rutile nanorods on the textured surface of FTO films was also reported by Hosono et al.<sup>134</sup> This small roughness has been pointed out as a potential problem in utilizing the nanorod arrays in the DSSCs. To decrease the width of the

nanorods, we modified the nucleation sites on the surface of the FTO films. Prior to the nanorod growth, the polymeric sol of TiO<sub>2</sub> nanoparticles smaller than 10 nm was spin-coated on the FTO films to increase the nucleation sites for the growth of the nanorods. Figure 3-12 shows AFM images of pure and polymeric TiO<sub>2</sub> sol coated FTO films. On the surface of the pure FTO film, the grain size was a few hundred nanometers and the root-mean-square (RMS) roughness was 20 nm. In contrast, very fine features with the RMS roughness of less than 5 nm was uniformly found on the surface of the polymeric sol coated FTO films. The appearance of the very small seeds is more pronounced in the amplitude error image (Figure 3-12 (c), (d)), since the variation in the signal in detecting the amplitude of the surface is very sensitive to the change in the surface roughness. The size of the nucleation seeds are about 18 nm, which is much smaller than the width of the nanorods directly grown on the bare FTO film/glass substrates.

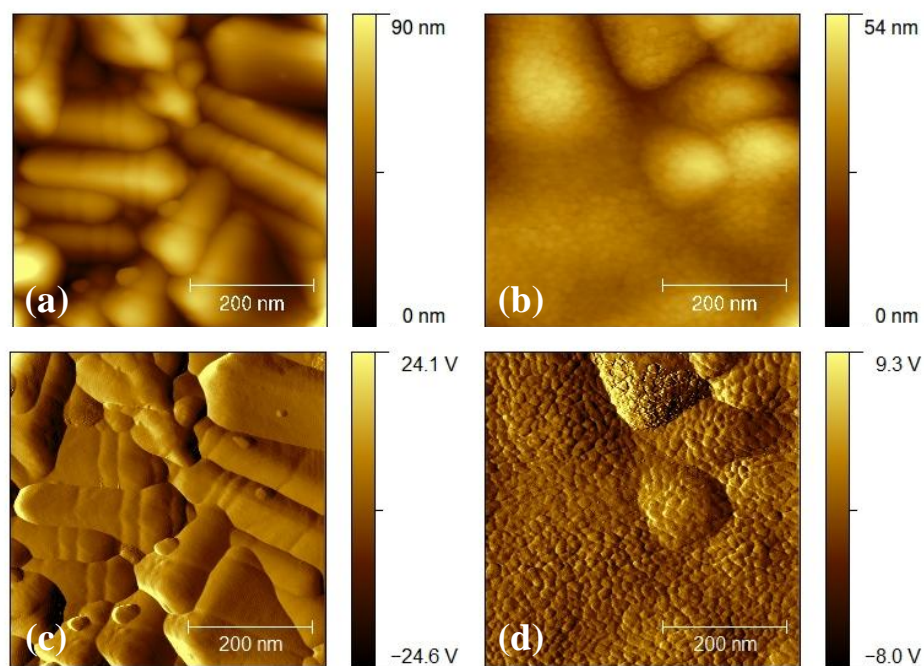


**Figure 3-12 AFM images of (a) bare FTO and (b) TiO<sub>2</sub> polymeric sol coated FTO; the amplitude error images of (c) bare FTO and (d) TiO<sub>2</sub> polymeric sol coated FTO during AFM measurement**

Figure 3-13 shows the effect of the nucleation seeds on the morphology of the rutile nanorods. The introduction of the TiO<sub>2</sub> nanoparticle layer significantly decreases the width of the individual nanorod and increases the density of the nanorods. These changes result from the presence of the nanoparticle seeds that promote the heterogeneous nucleation of the rutile nanorods. These narrow TiO<sub>2</sub> nanorods grown on the polymeric TiO<sub>2</sub> sol treated substrates were used in fabricating the DSSCs.

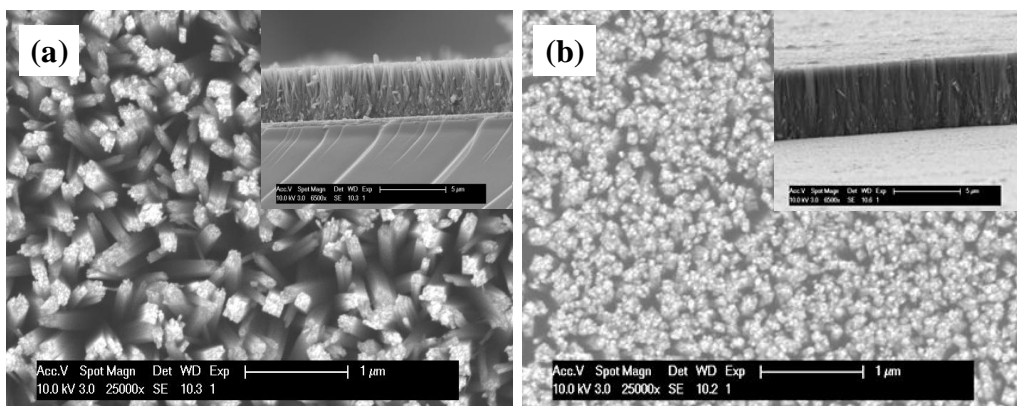


**Figure 3-13 SEM images of the nanorods grown (a) on pure FTO and (b) on TiO<sub>2</sub> polymeric sol coated FTO**

### 3.2.3 Carrier transport in TiCl<sub>4</sub> treated nanorods

TiCl<sub>4</sub> treatment is a common method used to enhance DSSC performance. It is very popular especially in nanowire/nanorod or nanotube based device. Here we investigate the influence of TiCl<sub>4</sub> coating on carrier transport in nanorod system.

The procedure of post-treatment follows: TiO<sub>2</sub> nanorod grown substrates with aforementioned cleaning were immersed into the 0.05 M TiCl<sub>4</sub> at 50°C for 30 min or 2 hrs.<sup>103</sup> Coated TiO<sub>2</sub> nanorod arrays were washed thoroughly with DI water, and annealed at 450°C for 30 min.

Figure 3-14 shows the J-V characteristics of the DSSCs which were fabricated using the 2.5  $\mu\text{m}$  long rutile nanorods. In DSSCs using the raw nanorod arrays, the short circuit current density ( $J_{\text{sc}}$ ), open circuit voltage ( $V_{\text{oc}}$ ), and fill factor (FF) are 2.55  $\text{mA}/\text{cm}^2$ , 0.85 V, and 0.60, respectively. Overall energy conversion efficiency is 1.31 %. These values are comparable to the DSSCs using the anatase nanoparticle photoelectrodes with the same thickness.<sup>30</sup> After the surface of the nanorods was treated with  $\text{TiCl}_4$  for 2 hrs,  $J_{\text{sc}}$  is dramatically increased to 8.13  $\text{mA}/\text{cm}^2$ , FF has similar value 0.63, and  $V_{\text{oc}}$  slightly decreases to 0.72 V. Subsequently, the total conversion efficiency of the DSSC is improved to 3.7%. This dramatic increase in  $J_{\text{sc}}$  is attributed to the increase in the amount of the dye adsorbed on the porous coating layer. Given that the rutile nanorods in DSSCs are only 2.5  $\mu\text{m}$  long, this relatively high efficiency of the solar cells indicates the potential benefit of the nanorods in the DSSCs.<sup>135,136</sup>

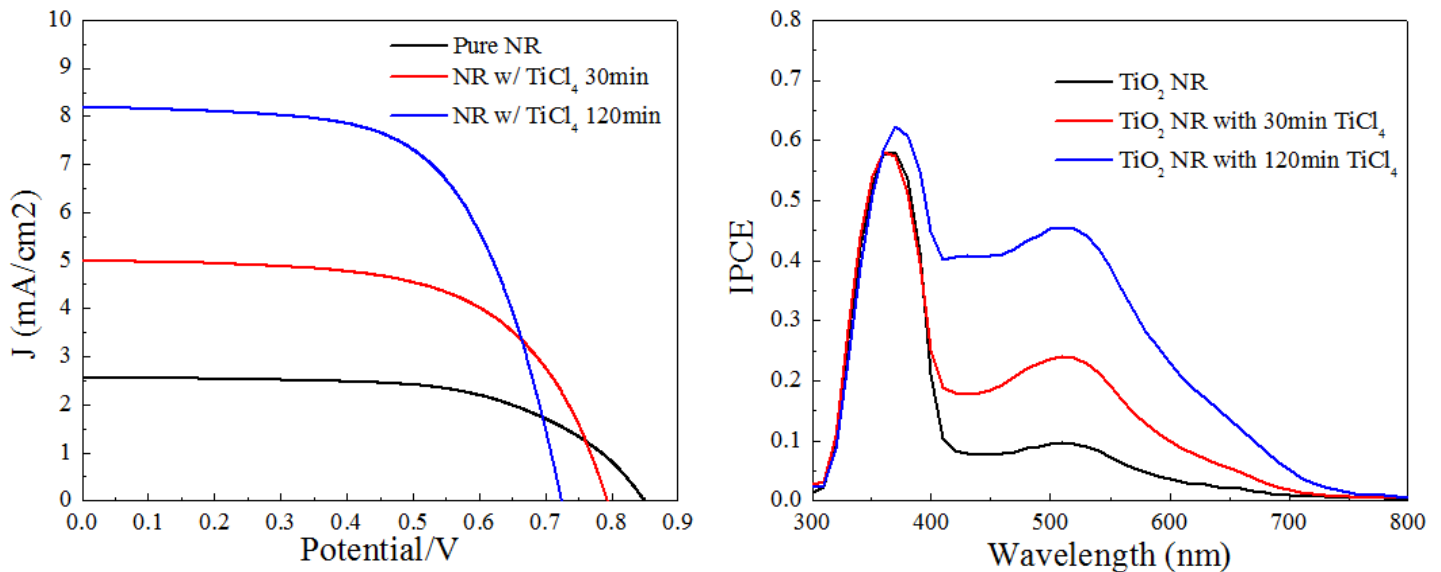
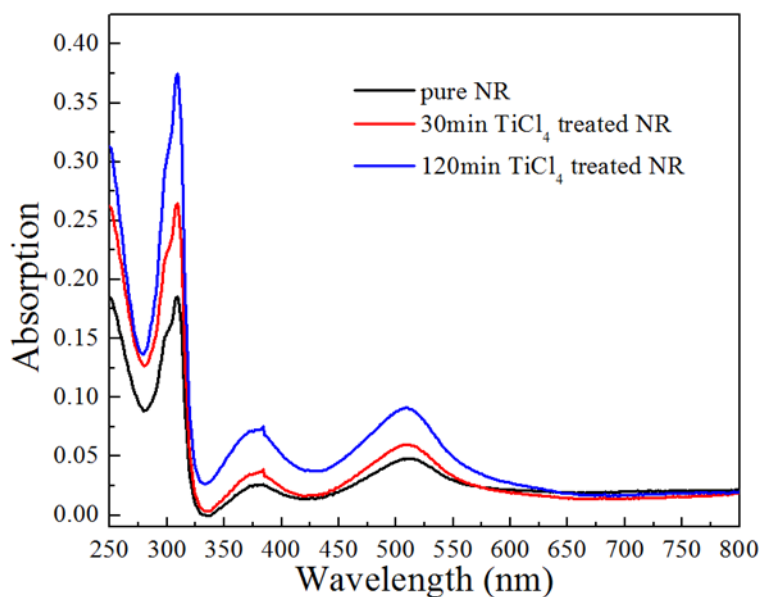


Figure 3-14 Performance of DSSCs using bare  $\text{TiO}_2$  nanorods and  $\text{TiO}_2$  nanorods treated with  $\text{TiCl}_4$  solution for different times; (a) J-V curves and (b) IPCE spectra

The IPCE spectra of the TiO<sub>2</sub> nanorod based DSSC are presented in Figure 3-14 (b). It is noted that the IPCE is the highest at the wavelength of 375 nm. This maximum IPCE value located in the UV regime results from the band-to-band transition in the rutile nanorods. The high crystallinity of the nanorods enhances the absorption of UV light and suppresses electron-hole recombination at the grain boundaries, which efficiently convert the UV light to the electricity.<sup>109</sup> A recent photoluminescence study showing a strong band-to-band peak in the nanorods at the room temperature indicates that the carriers are not easily trapped within the highly crystalline nanorods.<sup>137</sup> In the IPCE spectra of bare and coated TiO<sub>2</sub> nanorod arrays, the conversion efficiency at the wavelength of 375 nm is very similar. This implies that the surface coating layer has a negligible effect on the separation and transport of electron-hole pairs that are produced in the single crystalline rutile nanorods. The TiCl<sub>4</sub> treatment significantly increases the photon-electron conversion efficiency in the visible regime. The TiCl<sub>4</sub> effect in the nanoparticle based DSSCs has been explained in several viewpoints such as enhanced dye absorption<sup>110</sup>, enhanced charge transport due to dye bonding<sup>138</sup> or shift of conduction band edge<sup>139,140</sup>, scattering effect<sup>141</sup>, and suppression of surface recombination.<sup>140</sup>

To estimate the effect of the TiCl<sub>4</sub> treatment in the nanorod based DSSCs, the amount of the adsorbed dye was measured. Figure 3-15 shows the UV/Vis spectra of the dye adsorbed by the pure rutile nanorods and TiCl<sub>4</sub> treated rutile nanorods. If a single N719 dye molecule is assumed to occupy 1 nm<sup>2</sup> as N3<sup>131</sup>, the roughness factors are 243, 346, and 491 for pure, 30 min treated, and 120 min treated nanorods, respectively. Since the roughness factor is doubled after TiCl<sub>4</sub> treatment, it is evident that the increase in the amount of the adsorbed dye significantly contributes to the increase in the photocurrent by the TiCl<sub>4</sub> treatment, which agrees well with the IPCE spectra of Figure 3-14.



**Figure 3-15 Absorption spectra of dyes desorbed from DSSCs using bare, 30 min-TiCl<sub>4</sub> treated, and 120 min-TiCl<sub>4</sub> treated nanorods**

A remaining question of the interest is the transport and recombination of the carriers that are produced in the porous coating layer on the rutile nanorods. Therefore, we examined the detailed change in the electron diffusion coefficients and lifetimes of the photogenerated electrons on the microscale by using SLIM-PCV method. Figure 3-16 shows the diffusion coefficient and life time of DSSCs using the nanorod arrays which were treated with TiCl<sub>4</sub> for different time (0 hr, 30 min, and 2 hr). The diffusion coefficient is very sensitive to the surface state of the rutile nanorods. As TiCl<sub>4</sub> treatment time increases, the diffusion coefficient decreases. As a reference, we also prepared the rutile nanoparticle based DSSC from the similar TiCl<sub>4</sub> solution using reported method<sup>142</sup> without the nanorods and measured its diffusion coefficient. The diffusion coefficient of the pure rutile nanoparticle based DSSC is smaller than that of the pure rutile nanorod based DSSCs by more than one order of the magnitude. When the electrons pass through the nanoparticle electrodes, the carriers repeatedly experience trapping and detrapping processes and the time for the diffusion increases. The comparison of the rutile

nanoparticle, the rutile nanorod, and the  $\text{TiCl}_4$  treated coated nanorod indicates that the electron diffusion is very effective in the rutile nanorods. In addition, Figure 3-16 (a) shows that the introduction of the rutile nanoparticle in the electron transport path produces the trapping sites and prevents the fast diffusion of the electron. The implication of this observation is that the dramatic improvement of the diffusion coefficient can be achieved by using single crystalline nanorod that has less trapping sites such as necks.

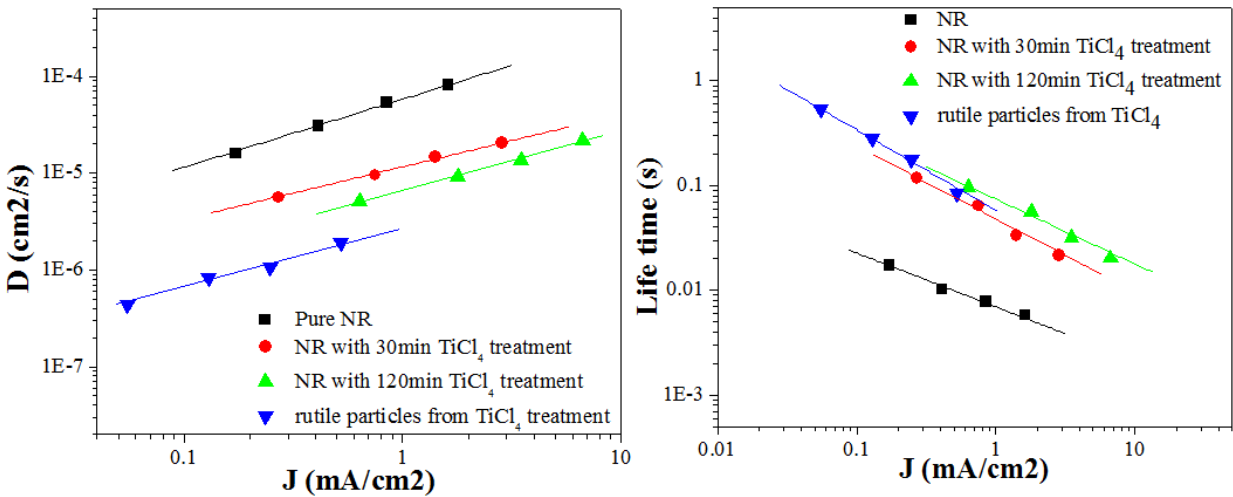
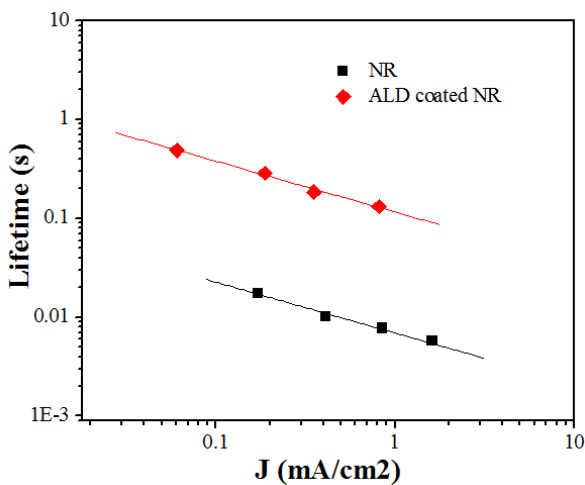


Figure 3-16 (a) Diffusion coefficient and (b) lifetime of DSSCs employing bare nanorods, 30 min- $\text{TiCl}_4$  treated nanorods, 120 min- $\text{TiCl}_4$  treated nanorods, and rutile nanoparticles grown from  $\text{TiCl}_4$  solution

The carrier lifetime in the mesoporous  $\text{TiO}_2$  films with different microstructure is shown in Figure 3-16 (b). In contrast to the diffusion coefficient, the lifetime in the different DSSCs is very similar except the pure nanorod based DSSC. This is strange, since the single crystalline nanorod is expected to decrease the recombination rate due to its fast transportation and less trapping sites. Further analysis shows that the lower lifetime of the pure nanorod based DSSC results from the backward electron transfer from the FTO to the electrolyte.<sup>143</sup> If the electrolyte is in contact with the FTO in the nanorod based DSSC, faster transport of the electron in the

nanorod accelerates the recombination of the electron in the FTO with iodine ions in the electrolyte.<sup>22</sup> The backward electron transfer is significantly reduced when the surface of the FTO is treated with the  $\text{TiCl}_4$  solution, as shown in Figure 3-16 (b). This is consistent with recent studies on nanotube devices.<sup>140,144</sup> To confirm the role of the backward electron transfer in the pure nanorod based DSSCs, the surface of FTO was passivated by depositing a 2 nm thick  $\text{TiO}_2$  layer. The passivation layer was coated on the surface of the nanorod grown FTO substrate by an atomic layer deposition (ALD) method. As shown in Figure 3-17, the lifetime in the FTO passivated DSSCs increases more than one order of the magnitude and becomes very close to the lifetime of DSSCs that are built on the pure rutile nanoparticles and the  $\text{TiCl}_4$ -treated nanorods. This clearly evidences that the lifetime is not sensitive to the microstructure of the mesoporous rutile films. Though the surface trapping site density and the grain boundary density are very different in several DSSCs of Figure 3-16 (b) and Figure 3-17, all DSSCs possess a similar carrier lifetime. This similarity implies that the electron transports through the surface of the rutile nanorods.



**Figure 3-17 Life time of DSSCs using bare nanorods and nanorod with a 3-nm thick passivation layer deposited by an ALD method**



In DSSCs, the photoexcited electron-hole pairs in the dye are quickly dissociated and the electrons and holes are transported to the TiO<sub>2</sub> network and the electrolyte efficiently. Then, the annihilation of the carriers mainly occurs at the interface between the TiO<sub>2</sub> mesoporous films and the electrolyte. Given this main annihilation mechanism, the similar carrier lifetime in all samples indicates that the probability of the electrons to meet with the electrolyte is almost the same in the nanoparticle and nanorod films. Therefore, it is proposed that the electrons injected to the nanorods are mainly located near the surface of the nanorods with the width of about 70 nm instead of being confined to the core of the nanorods. Therefore, in the open circuit state in which the carrier lifetime is measured, the electrons in the nanorods and the nanoparticles have similar chances to be recombined with the ions in the electrolyte.

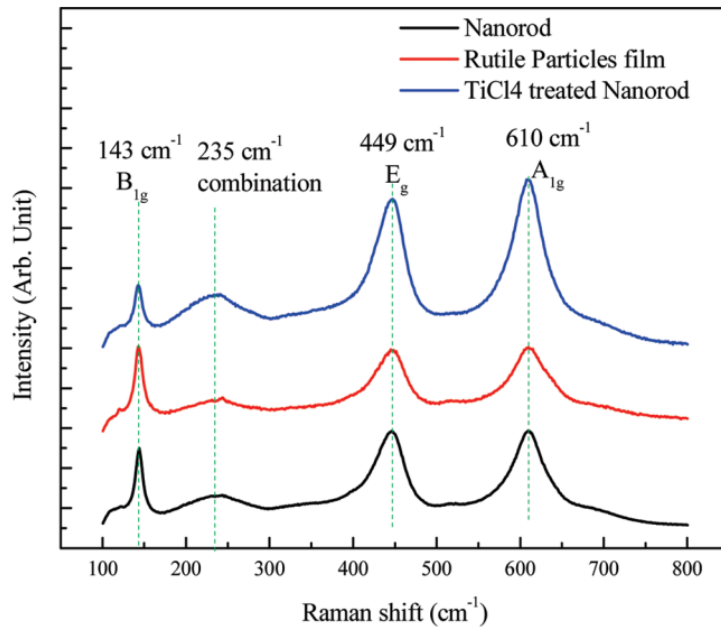


**Figure 3-18 Raman spectra of nanorod, rutile nanoparticle, and TiCl<sub>4</sub> treated nanorod**

It should be noted that our observation shows the dominance of surface diffusion instead of core diffusion. For ZnO nanowires, it has been proposed that the radial electric field, which comes from the upward band bending at the surface of nanowire, will suppress the

recombination of carriers by corralling injected electrons within the nanowire cores. The length scale, which is also called Debye-Huckel screening length, is roughly around one third of thickness of the space-charge layer. The Debye-Huckel screening length of ZnO, which is around 4nm for a carrier concentration of  $10^{18}\text{cm}^{-3}$ , could be realized in ZnO nanowire due to relative large geometry size. However, our  $\text{TiCl}_4$  treated rutile nanowire doesnot show this internal electric field. The possible reasons may be small size of decorated particles, homogenous coating, and small amount of carrier concentration. The crystal structure of  $\text{TiCl}_4$  treated nanorod was explored using Raman spectroscopy. As shown in Figure 3-18, all nanoparticles, nanorods, and  $\text{TiCl}_4$  treated nanorods have very similar pattern. All Raman peaks can be assigned to the rutile phase. This homogeneous contact may be responsible for the surface diffusion. Further exploration of engineered contacts should be carried out to overcome this surface diffusion.

## 4.0 DOPING IN NANOROD

### 4.1 BACKGROUND

The results of the Fe/N ions doping of TiO<sub>2</sub> nanoparticles in chapter 2 show that the doping can change the band gap and charge recombination of TiO<sub>2</sub>. Here, we will implement this understanding to modify the functional properties of TiO<sub>2</sub> nanorods. The first approach is to extend nitrogen doping to nanorod systems, expecting the complementary effect of band gap narrowing. The second one is using niobium doping in order to achieve better transport behavior and contact.

Nitrogen doping shows an effective red shift of the absorption edge, no increase of recombination, and a higher efficiency of solar light utilization. Therefore, it is of interest to combine nitrogen doping with nanorods. N-doped rutile nanorods are expected to expand the absorption of partial of visible light, and this enhanced absorption is complementary to N719 dye absorption, possibly producing a larger short circuit current in DSSCs. Normally, N-doping during the hydrothermal growth requires a basic environment, which is incompatible with our rutile nanorod synthesis environment. For this reason, we choose ammonia gas post-treatment for N-doping, which is reported in nanoparticle<sup>145</sup>, nanotube<sup>146</sup> TiO<sub>2</sub> samples. The location of doped N in the lattice is another factor to determine the efficacy of N doping. Interstitial doping of N will result in a relative deep defect level, which will disturb carrier transfer, while substitution of

N in TiO<sub>2</sub> will form shallow defect levels, which favor carrier transfer. It has been shown that ammonia gas annealing will provide a relative large portion of N substitution comparing the addition ammonium hydroxide to titanium precursor.

Nb doped TiO<sub>2</sub> has attracted considerable attention for various applications due to its excellent electronic compensation.<sup>147-149</sup> Sharma et al showed significant increase of sensitivity and short response time using Nb-doped rutile as an oxygen gas sensor.<sup>150</sup> Furubayashi et al demonstrated that comparable Nb doped anatase films possess comparable transport and optical property as conventional transparent conducting oxide, such as Sn-doped In<sub>2</sub>O<sub>3</sub> (ITO).<sup>149</sup> More recently, Nb doped TiO<sub>2</sub> has been applied to dye sensitized solar cell (DSSC).<sup>151-153</sup> Lu et al reported efficient electron injection and transfer arising from a positive shift of the flat-band position, and achieved 18.2% improvement of conversion efficiency using 5atom% Nb doped anatase particles.<sup>151</sup> The downside of this approach is the decrease of open-circuit voltage and degradation of the fill-factor. Yang et al explored the low concentration (< 1wt% Nb) doping effect on anatase nanotubes, and obtained 30% efficiency enhancement, which is ascribed to a lower recombination rate.<sup>153</sup> It is reasonable to extend the light doping to other architectures instead of nanotubes, and light doping may also have less of a side-effect on the drop of open circuit voltage. One goal of our research is to get an improved short circuit current without or with little sacrifice of open circuit voltage, which will result in appreciable enhancement of total efficiency.

Another important factor to influence the performance of DSSC is the back contact between the photoanode and FTO.<sup>154,155</sup> Nb doping has been reported as a novel approach to modify the contact, for example, a thin layer of Nb doped TiO<sub>2</sub> (NTO) has been found to have a better Ohmic-contact and less recombination.<sup>156</sup> The improvement of efficiency is due to

enhanced charge transfer and collection characteristics of NTO films, however, the additional NTO film requires a complicated procedure such as pulsed laser deposition (PLD). It would be more practical to have such an improved contact simply during preparation of the photoanode without additional procedures. Herein we investigate Nb doping effect on nanorod system expecting growth of nanorod and improved contact could be achieved simultaneously in one simple step.

Single crystalline rutile nanorods have been developed and evolved as an alternative architecture to nanoparticle based photoanode.<sup>109,110,157-159</sup> The strength of the nanorod is its high single crystallinity and good contact between the nanorod and substrate. What is more, nanorods on top of FTO are an ideal system for exploiting the back surface contact between FTO and TiO<sub>2</sub> with the assistance of conductive-AFM (c-AFM). C-AFM, especially photoconductive AFM, has been a powerful tool to probe the local current information on the nanoscale and shed light on the correlation between microstructure and performance in bulk heterojunction solar cell.<sup>160,161</sup> In addition to OPV, the contact and interaction between ZnO nanowires and AFM tip has been explored via c-AFM.<sup>162</sup> Characterization using C-AFM was successfully extended to the TiO<sub>2</sub> nanorod system. It is found that the current of lightly doped nanorods is increased at the same applied bias, and, this improvement comes from better contact facilitating electron injection from nanorod to FTO terminal after Nb doping, which at least partially contributes to longer lifetime.

#### **4.1.1 Metal-Semiconductor contact**

Contact is universal for devices as long as more than one material (or phase) is involved. Among contacts of different materials, the metal-semiconductor contact is very important. Generally, the metal-semiconductor contact is classified into several groups depending on the work function of

the metal ( $\Phi_M$ ) and the semiconductor ( $\Phi_S$ ). As shown in Figure 4-1, because the Fermi levels of the contacting materials become the same, the energy band diagram is modified in the contact. Consequently, majority carriers (electron) in n-type semiconductor are accumulated ( $\Phi_M > \Phi_S$ ), neutral ( $\Phi_M = \Phi_S$ ), or depleted ( $\Phi_M < \Phi_S$ ) compared with their concentrations in quasi-neutral states. An Ohmic junction is found in the contact with accumulated carriers, and a Schottky junction is observed in the contact with depleted carriers.

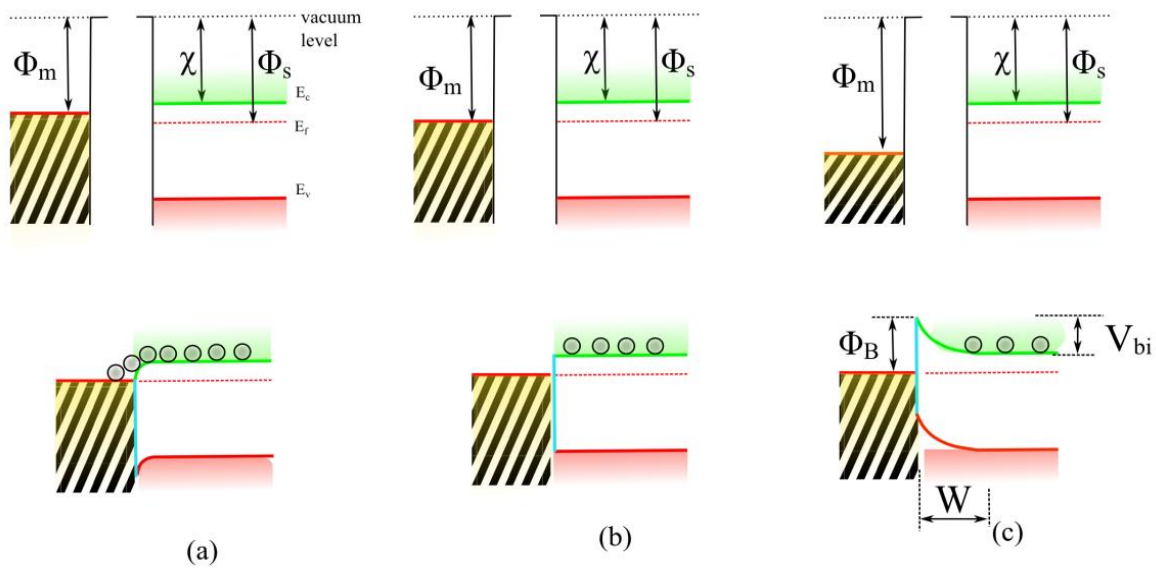


Figure 4-1 Three types of metal-semiconductor contact, (a) accumulated, (b) neutral, (c) depleted <sup>163</sup>

Schottky junction is a very common junction and provides a rectifying effect similar to a p-n junction. The barrier height  $\Phi_B$  at the contact is determined by:

$$\Phi_B = \Phi_M - \chi \quad (4-1)$$

where  $\chi$  is the electron affinity of the semiconductor, defined by the difference between the vacuum level and the bottom of the conduction band. Since the barrier height, in principle, is only related to  $\Phi_M$  and  $\chi$ , it is independent of doping concentration for any particular semiconductor.

Another important parameter of Schottky junction is built-in potential ( $V_{bi}$ ) and width of the depletion region ( $W$ ) at equilibrium as shown in Figure 4-1 (c).  $V_{bi}$  is the difference between  $\Phi_M$  and  $\Phi_S$ , and the width of depletion region can be described by:

$$W = \sqrt{\frac{2\epsilon_s V_{bi}}{qN_D}} \quad (4-2)$$

where  $q$  is the electronic charge,  $\epsilon_s$  is the permittivity of semiconductor, and  $N_D$  is donor concentration.

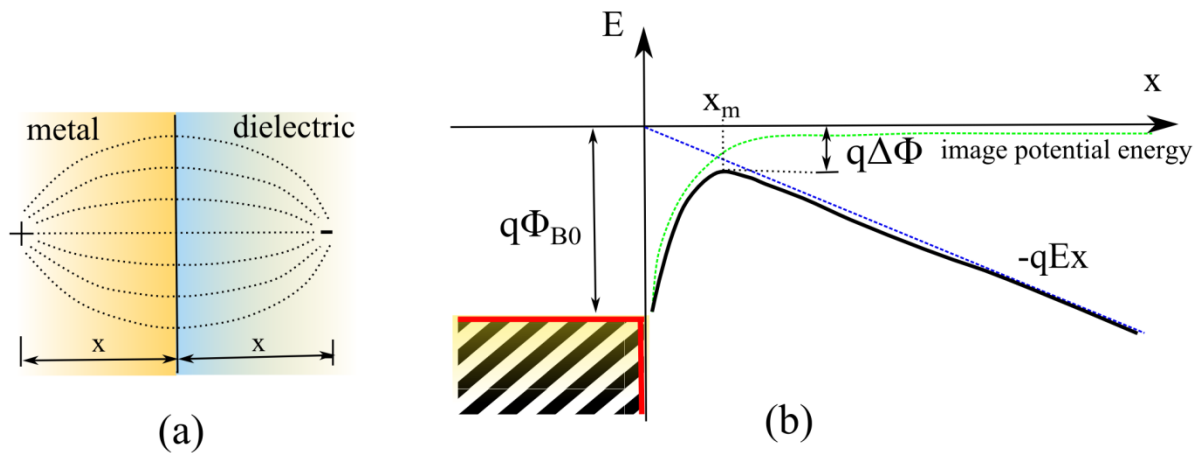


**Figure 4-2 Image charge and electric field distribution(a) and energy-band diagram with the influence of image-force (b) <sup>164</sup>**

There are a few additional factors which may alter the height predicted in Eqn. 4-1. One famous effect, Schottky effect, is an image force that lowers the potential barrier. This effect comes from the electric field that is applied to an electron on the dielectric side. As shown in Figure 4-2 (a), an electron at  $x$  distance from the interface to the metal side creates an electric field, and the field lines are perpendicular to the metal surface at the interface. This imaginary field is built up to create a positive image charge at the same distance  $x$  on the metal side. These imaginary fields could change the barrier height. By combining these imaginary fields with

external electric field  $E$ , the barrier height is lowered by  $\Delta\Phi$  at location  $x_m$  with the following relations,

$$x_m = \sqrt{\frac{e}{16\pi\epsilon_s E}} \quad (4-3)$$

$$\Delta\Phi = \sqrt{\frac{eE}{4\pi\epsilon_s}} = 2Ex_m \quad (4-4)$$

It should be noted that the barrier lowering is very small. For example, for  $\epsilon_s = 12\epsilon_0$ ,  $\Delta\Phi$  would be only 0.035V with an  $E$  field of  $10^5$ V/cm. Barrier lowering would be even smaller if  $E$  field is lower.

Another factor which may influence the barrier height is interface states. A model to simulate this factor can be established by introducing an additional thin interfacial layer (thickness  $\delta$ ), that can transport electrons freely and sustain potential difference ( $\Delta$ ). In this interface, there are numerous interface states, with a density of  $D_{it}$ . An important energy level, surface potential  $\Phi_0$ , defines the charge at these interfaces. All states below  $\Phi_0$  are donor states, which means these states are neutral if the state contains an electron and positively charged if the state does not contain an electron. Similarly, the states above  $\Phi_0$  are assumed to be acceptor states, which will be either neutral (without an electron) or negatively charged (with an electron). Figure 4-3 shows a semiconductor with acceptor interface traps. The interface-trap charge density (negative) on the semiconductor is  $Q_{ss}$ , defined by both  $D_{it}$  and the energy difference between the Fermi level and the neutral level, and the space charge density on the semiconductor side, which is related to depletion width and doping concentration, is  $Q_{sc}$ . The charge density on the metal side ( $Q_M$ ) can be represented by  $Q_{ss}$  and  $Q_{sc}$  based on the charge neutrality. Then, by applying Gaussian's law, the following relation can be obtained:

$$\Phi_m - \chi - \Phi_{B0} = \sqrt{\frac{2q\epsilon_s N_D \delta^2}{\epsilon_i^2}} \left( \Phi_{B0} - \Phi_n - \frac{kT}{q} \right) - \frac{qD_{it}\delta}{\epsilon_i} (E_g - q\Phi_0 - q\Phi_{B0}) \quad (4-5)$$



The extreme case for Eqn. 4-5 is when  $D_{it}$  approaches to infinity. This means that the density of surface states becomes very large. Eqn. 4-5 could then be simplified to

$$q\Phi_{B0} = E_g - q\Phi_0 \quad (4-6)$$

Eqn. 4-6 indicates that the barrier height is determined solely by the surface property of the semiconductor, irrespective of the metal work function. The Fermi level at the interface is pinned by the surface states at  $q\Phi_0$  above the valence band. This Fermi level pinning has an influence on forming Schottky contact even with various types metals, as shown in Figure 4-1 (c) for common semiconductor made of Ge, Si, GaAs, and other III-V materials.<sup>163</sup> For this reason, we had to resort to doping to achieve a good Ohmic junction.

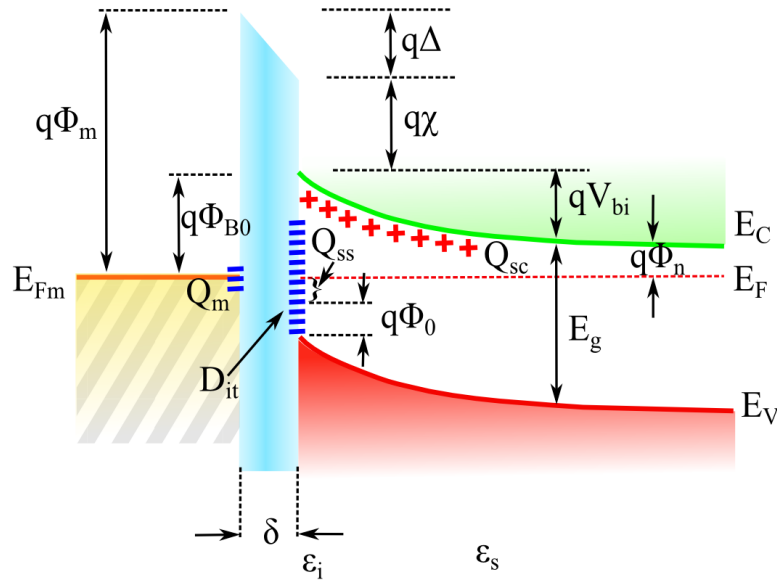


**Figure 4-3 Detailed energy-band diagram of metal-n-semiconductor contact with a thin interfacial layer<sup>165</sup>**

As shown in Eqn. 4-1, the barrier height is independent of the doping concentration, but the barrier width does depend on the doping concentration. Other factors, such as barrier lowering by the image force, may change barrier height after doping, but its effect is usually negligible. Therefore it is worthwhile to discuss the effect of doping on depletion width. With the

space-charge region (SCR) width  $W$  being proportional to  $N_D^{-1/2}$ , as shown in Eqn. 4-2, it is obvious that highly doped semiconductors have a narrow SCR width. For metal-semiconductor contacts with narrow SCR widths, electrons can tunnel from the metal to the semiconductor and from the semiconductor to the metal.

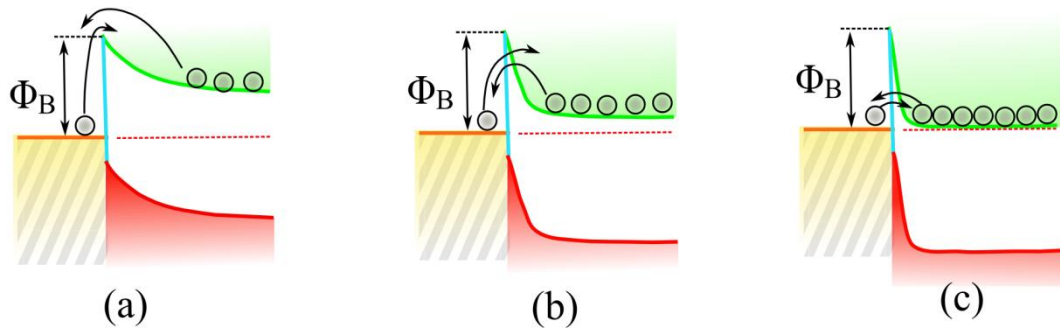


**Figure 4-4 Electron transport at different doping level, (a) thermionic emission, (b) thermionic field emission, (c) field emission<sup>163</sup>**

The conduction mechanism for a metal-n-type semiconductor is illustrated in Fig. 33. For lowly-doped semiconductors ( $N_D < 10^{17} \text{ cm}^{-3}$ ) the current flows as a result of thermionic emission (TE) as shown in Figure 4-4(a) with electrons thermally excited over the barrier. In the intermediate doping range ( $10^{17} < N_D < 10^{19} \text{ cm}^{-3}$ ) thermionic-field emission (TFE) dominates. The carriers are thermally excited to an energy where the barrier is sufficiently narrow for tunneling to take place. With field emission (FE), where  $N_D > 10^{19} \text{ cm}^{-3}$ , the barrier is so narrow that electrons can tunnel directly at or near the bottom of the conduction band.

Current-voltage (I-V), current-temperature (I-T), capacitance-voltage (C-V), and photocurrent (PC) have been employed to perform a quantitative analysis of the Schottky contact. Among these measurements, measurement of I-V is one of the widely used methods. I-V measurement can be interpreted through the frame of thermionic emission theory (more precisely, thermionic-emission-diffusion theory). Considering the factor of series resistance, current is governed by

$$I = I_s \left( e^{\frac{q(V-Ir_s)}{nkt}} - 1 \right) \quad (4-7)$$

where  $I_s$  is the saturation current, and has the following relations,

$$I_s = AA^{**}T^2 e^{-q\Phi_B/kT} \quad (4-8)$$

where  $A$  is the diode area,  $A^{**}$  is modified  $A^*$  (Richardson's constant) considering optical phonon scattering and quantum mechanical reflection,  $\Phi_B$  is the effective barrier height, and  $n$  is the ideality factor.

The thermionic emission in Eqn. 4-7 is similar to the current-voltage relation of the p-n junction. However, two differences exist. First, they have different saturation current terms. The saturation current in the p-n junction is determined by the diffusion of minority carriers while the saturation current in the Schottky junction is governed by the thermionic emission of majority carriers over a potential barrier. Hence, the saturation current of Schottky junction is much larger than that of the p-n junction and the turn-on voltage is smaller for Schottky junction. Second, they have different frequency responses. Since a Schottky barrier diode is a major carrier device, there is no diffusion capacitance in the case of forward bias and no minority carrier storage in the case of reverse bias. This characteristic makes the Schottky barrier diode more suitable for higher-frequency device. A typical switching time for a Schottky diode is in the picosecond range, while the switching time of the p-n junction is usually in the nanosecond range.

A typical I-V curve is shown in Figure 4-5. A straight line can be found when  $kT/q \ll V$  and  $Ir_s \ll V$ . Deviation from a linear line at low current comes from the -1 term in the equation, and a series resistance makes another bending at a high current regime.

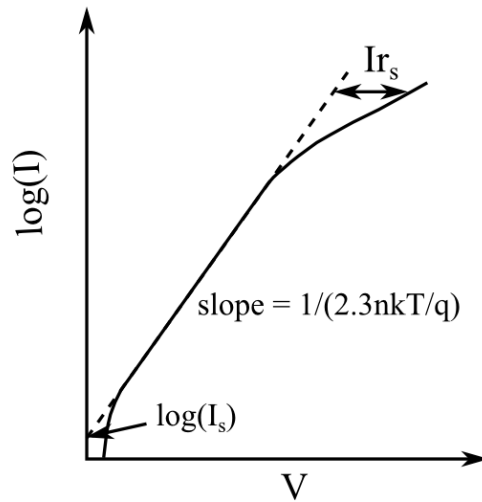


Figure 4-5 Typical I-V curve for a Schottky contact<sup>163</sup>

The series resistance can be derived by

$$I \frac{dV}{dI} = I r_s + \frac{nkT}{q} \quad (4-9)$$

Figure 4-6 presents an example of derivation of series resistance through the slope of  $I dV/dI - I$  curve in a p-n junction. The slope of experimental data line represents series resistance. This similar approach can be applied to Schottky contact as well.<sup>166</sup>

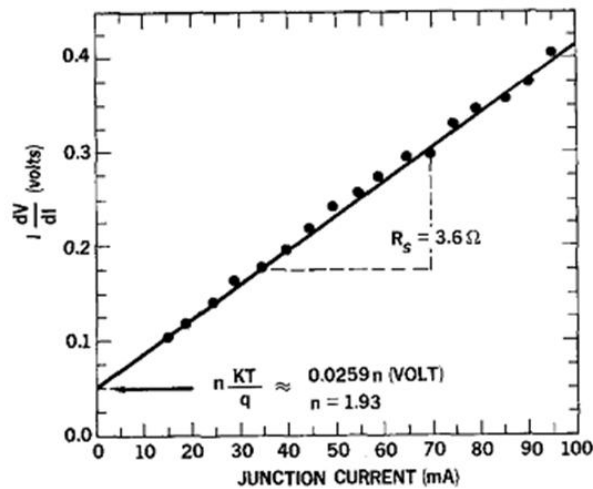


Figure 4-6 Derivation of series resistance in p-n junction using  $I dV/dI$  vs  $I$  plot<sup>167</sup>

### 4.1.2 Electrochemical Impedance Spectroscopy

Impedance spectroscopy is the measurement of the ac current (or voltage) at a specific angular frequency ( $\omega$ ) when the ac voltage (or current) is applied.<sup>168</sup> The complex impedance is scanned as the frequency ( $f = \omega / 2\pi$ ) of AC field changes over several decades (eg. from mHz to 10 MHz).

Complex impedance  $Z$  is defined as

$$Z(\omega) = \frac{\hat{V}(\omega)}{\hat{I}(\omega)} \quad (4-10)$$

The applied ac stimulus is superimposed on top of the steady state, which can be constrained by stationary conditions such as dc current and illumination intensity. As shown in Figure 4-7 (a), a sinusoidal signal is applied on top of  $V_o$  and  $J_o$  condition. A steady state is very important to relate measurement to a given physical model, which will be discussed in the last part of this section.

Normally, the applied stimulus is a small perturbation compared to the steady state bias. For example, an applied ac voltage ( $\sim$  mV) should be far smaller than the steady state bias ( $\sim$ V),  $\hat{V} \ll \bar{V}$ . This small perturbation will result in a linear proportionality between  $\hat{I}(\omega)$  and  $\hat{V}(\omega)$ , which further ensures that the calculated impedance is independent of the amplitude of the perturbation.

The time transient method, which uses small-amplitude time transients, mathematically contains the same information as small-frequency linear impedance. The bridge between these two is the Laplace transform. For the decay governed by a single process, both methods are equally valid. However, the EIS method makes it much easier to deconvolute responses having multiple processes from the spectroscopic response  $Z(\omega)$ .

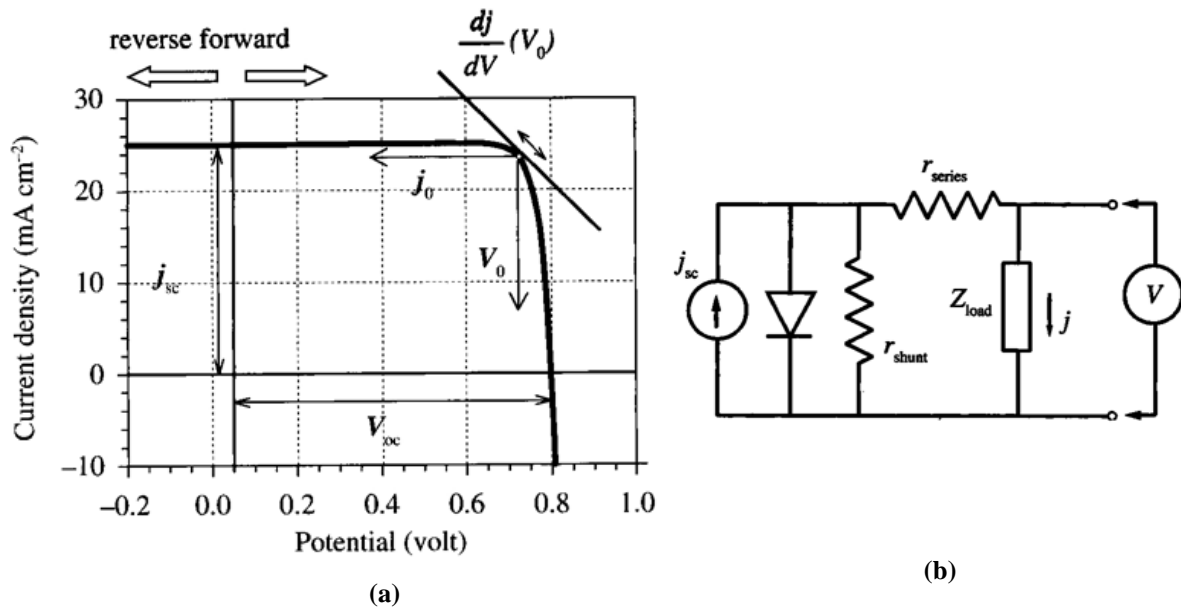


Figure 4-7 Schematics of EIS measurement (a), a small amplitude sinusoidal oscillations with different frequencies are superimposed to a steady bias; DC solar cell equivalent circuit model (b), components of this model include current source, diode, shunt resistance, series resistance, and external load

168

The parameters obtained in EIS are differential resistance and differential capacitance, which are strongly related to the frequency. At zero frequency, impedance is simplified to dc resistance ( $R_{dc}$ ). This  $R_{dc}$  is the reciprocal of the slope of the I-V curve, and can be used to interpret the shunt resistance ( $R_{shunt}$ ) and series resistance ( $R_{series}$ ) when steady states are set to short-circuit voltage and open-circuit voltage respectively.  $R_{shunt}$  and  $R_{series}$  are important parameters for solar cells in dc model as shown in Figure 4-7 (b). For a semiconductor solar cell, these resistances are independent of voltage, but it is not always the case especially for devices involved with electrochemical processes, such as DSSCs.

In the frequency domain, capacitance can be obtained through a simple conversion from impedance:

$$C^*(\omega) = \frac{\hat{I}(\omega)}{i\omega\hat{V}(\omega)} = \frac{1}{i\omega Z(\omega)} \quad (4-11)$$

One advantage of EIS measurement is the ability to test equivalent circuits, which could reflect important physical meaning if it is properly built. Equivalent circuits are composed of four basic electrical elements as shown in Table 4-1. These elements can be aligned in either in series (constant current) or in parallel (same applied voltage).

Table 4-1 Basic ac electrical elements





Denomination	Symbol	Scheme	Impedance
Resistance	R		R
Capacitance	C		$1/(i \omega C)$
Inductor	L		$i \omega L$
Constant phase element (CPE)	$Q_n$		$(i \omega)^{-n}/Q_n$

Figure 4-8 gives an example of an equivalent circuit (two resistors and one capacitor) and its spectroscopies. The equivalent circuit is composed of RC parallel combination ( $R_1$  and  $C_1$ ) and series resistance  $R_2$ .  $R_2$  and  $C_1$  are fixed at specific numbers ( $R_2=1k\Omega$ ,  $C_1=10mF$ ), and a set of  $R_1$  was investigated, namely 2 k $\Omega$ , 4 k $\Omega$ , and 5 k $\Omega$ . As shown in Figure 4-8 (b), a series of semicircles were observed in the complex impedance plane or the Nyquist plot. These semicircles have been shifted from the origin at  $R_2$  distance. The diameter of the semicircles is related to the resistor in the RC combination ( $R_1$  in this case). The impedance of the circuit can be described as following:

$$Z(\omega) = R_2 + \frac{R_1}{1+i\omega\tau_1} \quad (4-12)$$

where  $\tau_1$  is the relaxation time ( $\tau_1=R_1C_1$ ). If the frequency is zero,  $Z(0)$ , dc resistance, will be  $R_1+R_2$ . And if the frequency goes to infinity, the impedance will become  $R_2$ . For other frequencies between zero and infinity, the impedance can be found at points on the semicircle, and the frequency increases in the counter-clock direction. Figure 4-8 (c) shows how the real component of impedance changes from the low frequency (represent  $R_1+R_2$ ) to the high frequency ( $R_2$ ). The difference in relaxation time is present in the shift of the phase peak in the Bode plot. The lower is the frequency at the peak position, the longer is the relaxation time.

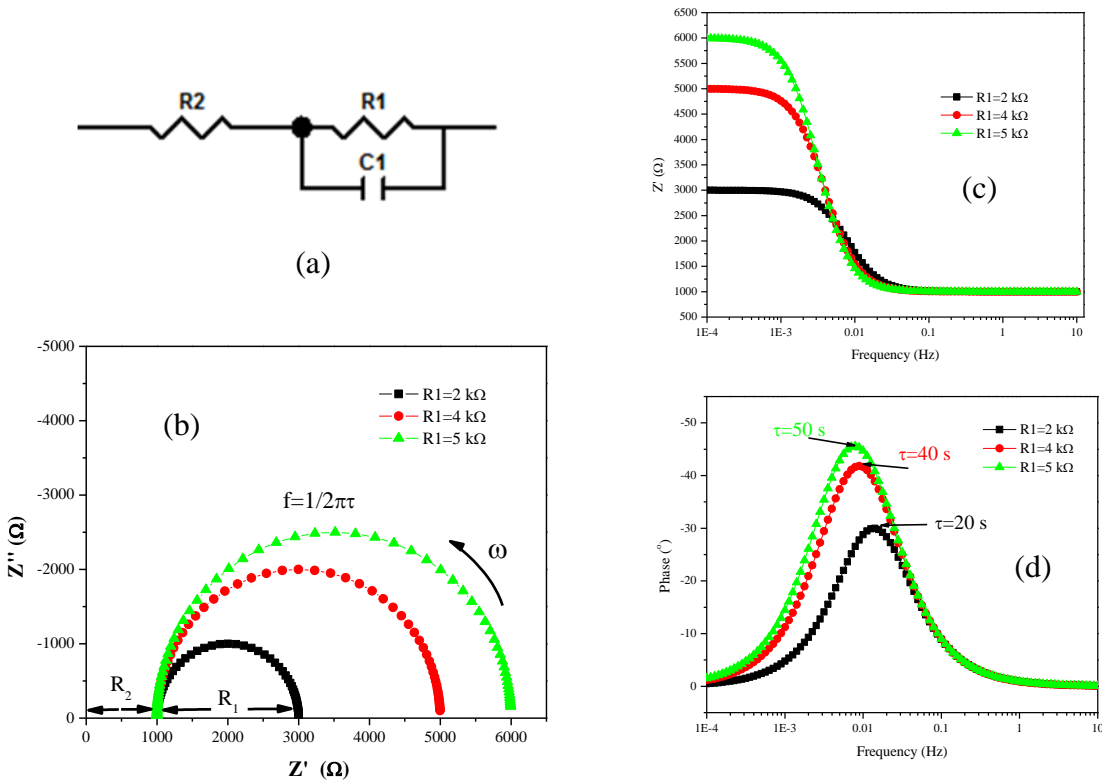


Figure 4-8 Equivalent circuit (a) and its corresponding spectroscopies,  $Z''$ - $Z'$  Nyquist plot (b),  $Z'$ -frequency (c), and Phase-frequency Bode plot (d)<sup>168</sup>



For liquid electrolyte cells, an equivalent circuit can be described as a combination of several resistors and capacitors as shown in Figure 4-7 (b).  $R_{pt}$  is the charge-transfer resistance on the Pt coated counter electrode side, representing the resistance for regenerating  $I_3^-$  into  $I^-$ .  $C_{pt}$  is used to describe the Helmholtz capacitance at the same counter electrode interface. On the anode side, although the FTO is covered by a layer of  $TiO_2$ , there are still some spaces exposed to the electrolyte directly, also known as the back-layer (BL). Similarly, charge transfer resistance ( $R_{BL}$ ) and capacitance ( $C_{BL}$ ) exists in the interface of the back-layer. Series resistance ( $R_s$ ) refers to the sheet resistance in the FTO and the geometry of the cell. The diffusion of redox species in the electrolyte is modeled as  $Z_d$  using the finite-length Warburg impedance in thin layer electrochemical cells. The remaining components account for carrier transport and storage in mesoporous  $TiO_2$ .

Normally, a transmission line model is used to interpret the underlying physics in the  $TiO_2$  network. This model includes chemical capacitance ( $c_\mu$ ), recombination resistance ( $r_r$ ), and transport resistance ( $r_t$ ). The finite transmission line with several capacitors and resistors can be seen in the gray region ( $TiO_2$ ) of Figure 4-9 (b). Resistance should be interpreted as the relationship between the electron flux (current) and the gradient of the quasi-Fermi level, and the chemical capacitance is the ability to store electronic charge in mesoporous oxide system. If the charge transfer involves only the conduction band electron of the semiconductor, which is true for a liquid electrolyte system, the  $r_t$ ,  $r_r$ ,  $c_\mu$ , and their corresponding effective values  $R_t$ ,  $R_r$ ,  $C_\mu$  have the following relations:

$$r_t = \frac{k_B T}{q^2 A n_c D_0} \quad (4-13)$$

$$r_r = \frac{k_B T \tau_0}{A q^2 n_c} \quad (4-14)$$

$$c_\mu = A q^2 g(E) \quad (4-15)$$

$$R_t = r_t d_{film} \quad (4-16)$$

$$R_r = \frac{r_r}{d_{film}} \quad (4-17)$$

$$C_\mu = c_\mu d_{film} \quad (4-18)$$

where  $D_0$  is the diffusion coefficient,  $\tau_0$  is the free electron lifetime,  $g(E)$  is the distribution of localized state,  $d_{film}$  is the film thickness, and  $A$  is area. The electron diffusion length and effective electron lifetime could be derived from  $R_r$ ,  $R_t$ , and  $C_\mu$ . If the stored charge is predominantly in trap sites ( $n_t \gg n_c$ ), the electron diffusion length ( $L_n$ ) and the effective lifetime ( $\tau$ ) have following relations:

$$L_n = \left( \frac{R_r}{R_t} \right)^{1/2} d_{film} \quad (4-19)$$

$$\tau = R_r C_\mu \quad (4-20)$$

Above equations show that larger recombination resistance leads to longer diffusion length and longer lifetime.

In principle, you can fit the components of impedance spectra using physical/mathematical models. In practice, it would be problematic or time-consuming to fit the whole set of parameters. Hence, the spectra are simplified by changing the measurement condition such as external electric potential. The position of the Fermi level of the  $TiO_2$  in contact with the electrolyte is controlled by applying external potential. Consequently, the conductivity of  $TiO_2$  can be modulated, and the different impedance spectra are found (refer to Figure 4-9).

When a small electric potential is applied in the forward or reverse direction, the resistance of  $\text{TiO}_2$  tends to be infinite, and its contribution to the EIS spectrum can be negligible. As shown in Figure 4-9 (a), only a part of the arc from high resistance and capacitance in the back layer is appreciated. Other components, such as the counter electrode, are hidden, because of the overwhelming magnitude of back layer.

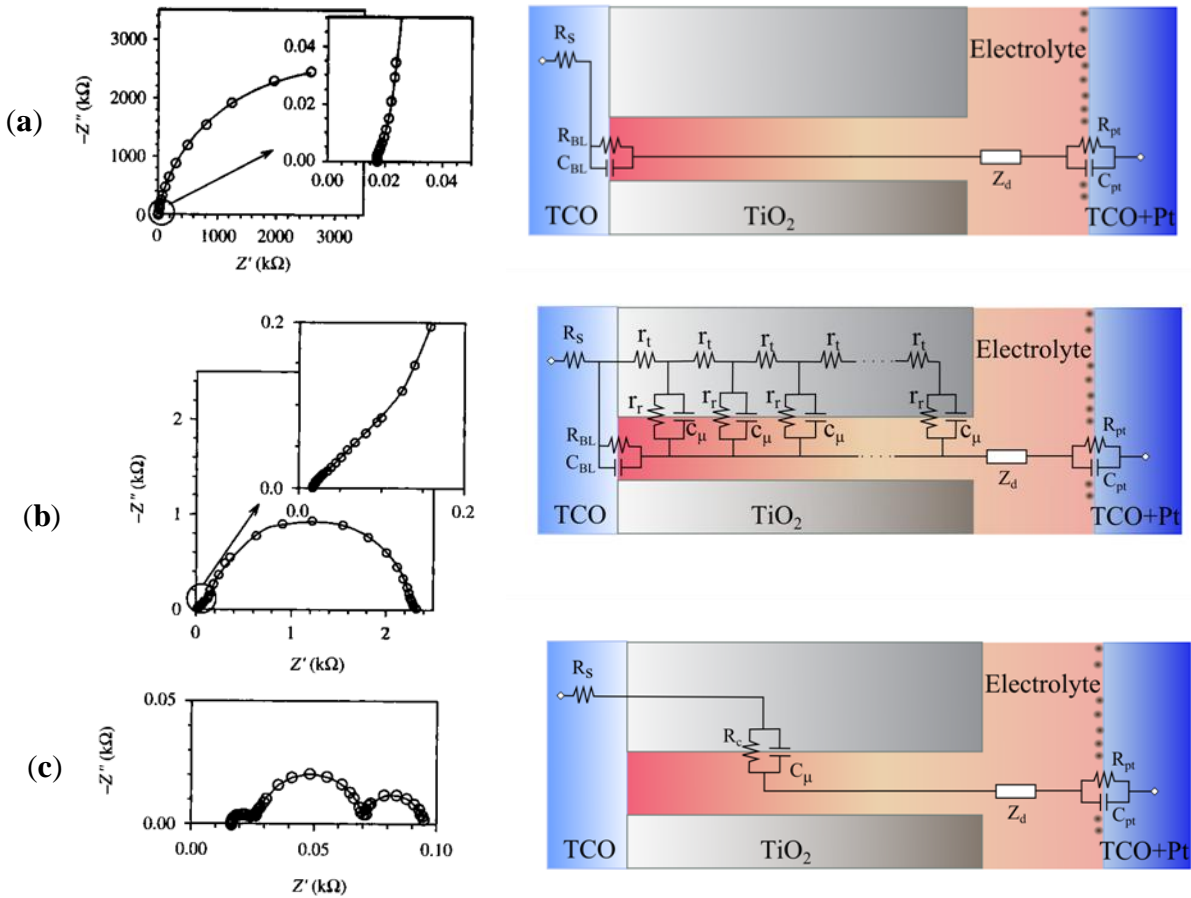


**Figure 4-9** Experimental EIS spectra of an ionic liquid DSSC (left) and simplified equivalent circuit model at different potential in the dark, (a) low potential; (b) intermediate potential; (c) high potential<sup>168</sup>

At intermediate potential,  $\text{TiO}_2$  contributes to the spectrum with its full resistance and chemical capacitance, and a whole transmission-line-equivalent circuit should be used for the fitting. For an efficient DSSC,  $R_t$  should be less than  $R_r$ . A slope close to 1 will be observed at high frequency, and this feature is like Warburg diffusion feature. This Warburg feature can be

interpreted as the diffusion of electrons in  $\text{TiO}_2$ . The large semicircle in the medium frequency comes from the  $R_r$  and  $C_\mu$ . The  $Z_d$  shows up only slightly at low frequencies. In the cases where  $R_t$  is larger than  $R_r$ , the impedance of semiconductor would behave like Gerischer impedance element.

At higher potential, normally near or higher than open circuit voltage,  $\text{TiO}_2$  will be highly conductive. A high concentration of electrons in the conduction band forms due to the lift of the Fermi level under high potential. The transmission line equivalent circuit could be simplified to simple R-C circuit as shown in Figure 4-9 (c). Typically there are three arcs in the spectrum. The high frequency arc at the left side comes from the  $R_{pt}$  and  $C_{pt}$  in the counter electrode, the second arc represents the recombination resistance and chemical capacitance at the  $\text{TiO}_2$  - electrolyte interface, and the last arc at low frequency is the result of the impedance of diffusion in the electrolyte. The width of the three arcs corresponds to  $R_{pt}$ ,  $R_r$  and  $R_d$  respectively, and the initial displacement of the arcs from the origin indicates the  $R_s$  in the system.

### 4.1.3 Mott-Schottky Plot

A Mott-Schottky plot is an effective approach to determine the flat band potential in a semiconductor-electrolyte system.<sup>169-172</sup> As shown in Figure 4-10, there is a band energy change after contact.<sup>169</sup> The energy level in the electrolyte is determined by redox-active species in solution. Due to molecule exchange and dynamic processing in a bulk electrolyte, the density of the redox state normally has Gaussian distribution.  $\lambda$  is the solvent-sheath energy. When the semiconductor and electrolyte reach each other, an equilibrium state is reached and band bending occurs as shown in Figure 4-10 (b). If you apply a particular potential, which is called flat band potential, the semiconductor band could remain flat without band bending or charge depletion.

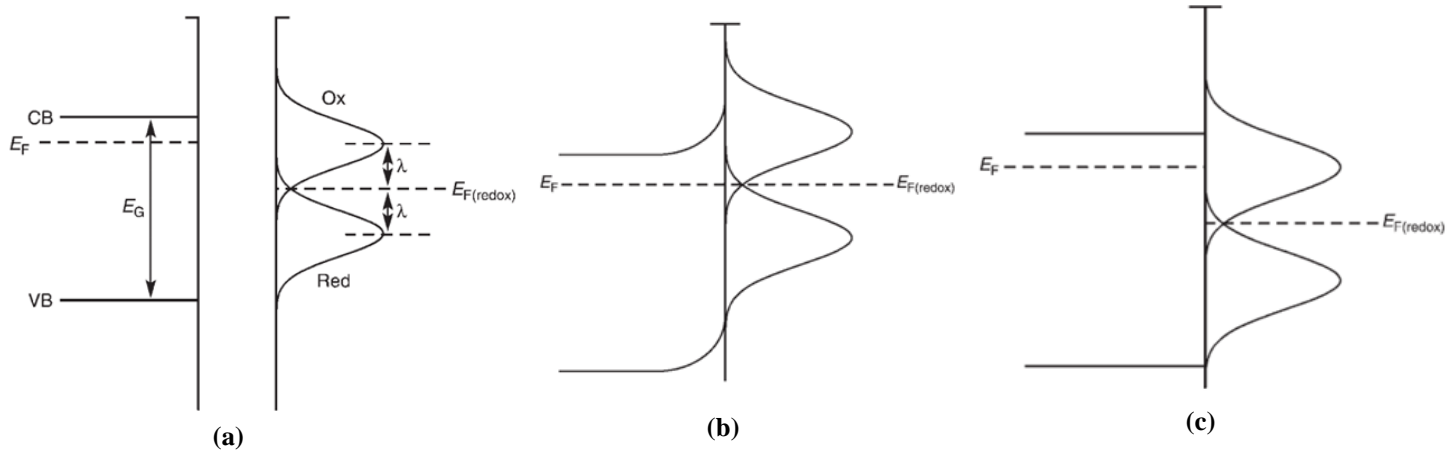


**Figure 4-10 Band diagram of n-type semiconductor and electrolyte before contact (a), after contact (b), and at its flat band potential  $V_{fb}$  <sup>169</sup>**

Theoretically, the Mott-Schottky equation as shown in Eqn. 4-21 can be obtained through solving Poisson's equation.

$$\frac{1}{C^2} = \frac{2}{\epsilon\epsilon_0 A^2 q N_D} \left( V - V_{fb} - \frac{k_B T}{q} \right) \quad (4-21)$$

where  $C$  is the interfacial capacitance,  $A$  is its area,  $\epsilon$  is the dielectric constant of the semiconductor,  $\epsilon_0$  is the permittivity of free space,  $V$  is the applied voltage,  $V_{fb}$  is the flat-band potential,  $N_D$  is the number of donors,  $k_B$  is Boltzmann's constant, and  $q$  is the electronic charge.

Based on this equation, we can plot  $1/C^2$  vs potential as shown in Figure 4-11. If we know the area, and the dielectric constant of semiconductor, we can obtain the donor number and flat-band potential through slope and x-axis intercept respectively.

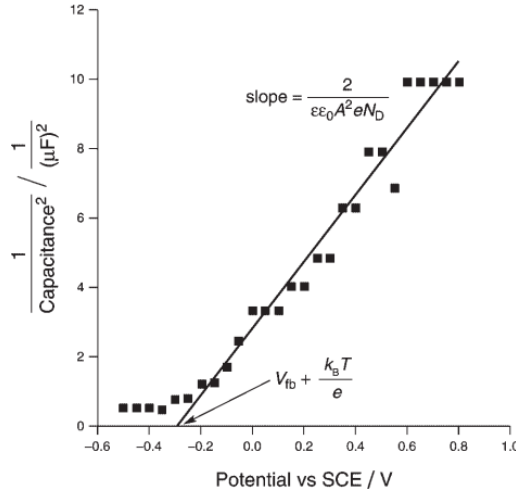


**Figure 4-11 Mott-Schottky plot of ZnO, slope and intercept can be used to determine donor concentration and flat band respectively <sup>169</sup>**

Capacitance can be determined using the impedance method summarized in the previous section. Through a set of small oscillations with various frequencies, an equivalent circuit can be established and fitted as talked in EIS section. A simplified measurement of capacitance has been proposed by Oliva et al.<sup>172,173</sup> The equivalent circuit is constructed as R(CR) as shown in the inset of Figure 4-12. The impedance of the equivalent circuit is,

$$Z(\omega) = R_S + \frac{R_{ox}}{1+R_{ox}^2 C^2 \omega^2} - i \frac{R_{ox}^2 C \omega}{1+R_{ox}^2 C^2 \omega^2} \quad (4-22)$$

where  $R_{ox}$  is the parallel resistance, and  $R_S$  is the series resistance.

If the angular frequency is large enough, the imaginary term of impedance can be reduced to  $1/(C\omega)$ . Therefore, capacitance can be represented by an imaginary component of impedance:

$$C = \frac{-1}{Z_{image}\omega} \quad (4-23)$$

What is more, it has been found that capacitance is almost a constant in the frequency region between 18Hz and 80Hz in 0.1M NaCl, pH=4.7, RT electrolyte for TiO<sub>2</sub> nanocrystalline

electrode as shown in Figure 4-12. Several groups have used this approach to measure Mott-Schottky plot.<sup>151,174</sup>

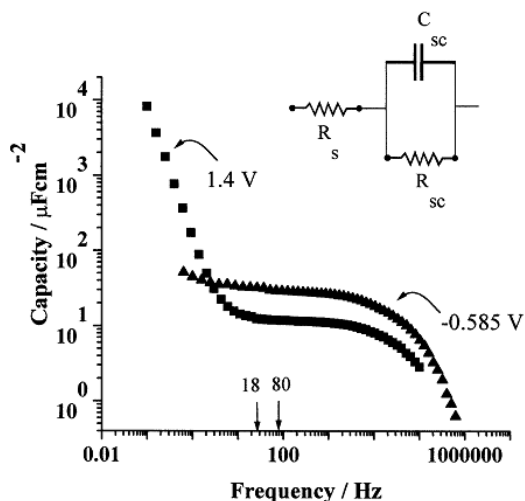


Figure 4-12 Electrode capacity vs. log frequency plot, in 0.1 M NaCl electrolyte at two potential values, pH 4.7 and room temperature<sup>172</sup>

## 4.2 NIOBIUM DOPING IN NANORODS

### 4.2.1 Experiment

The procedure to grow rutile nanorods with the assistance of microwave heating is slightly modified from previous reported method.<sup>159</sup> Briefly, a thin layer of TiO<sub>2</sub> was deposited via 8mM TiCl<sub>4</sub> 50 °C water bath for two hours onto FTO film coated glass to suppress the back reaction on top of FTO substrate. For pure TiO<sub>2</sub> nanorods, 1.7ml titanium tetraisopropoxide (TTIP) was dripped into the mixture of 53ml de-ionized water and 67ml concentrated hydrochloric acid. For Nb-doped TiO<sub>2</sub> nanorods, NbCl<sub>5</sub> (Sigma-Aldrich) was added into HCl

acid mixture at designed doping levels (0.1%, 0.25%, 0.5%, and 1%) and the mixture was stirred for 12 hours. A TiO<sub>2</sub> layer deposited substrate and a mixture solution of precursors were placed in a Teflon vessel and reacted at 180 °C for 50min under microwave irradiation (MARS, CEM).

After as-grown nanorods on the substrates were cleaned to remove residual organics, they were immersed into 0.27 mM N719 dye (ruthenium 535-bis TBA solaronix) for 24 hours. Dye-anchored nanorods on FTO glass were capped by a Pt-coated FTO glass. Two plates were separated by hot-melt sealing foil (SX1170-25, solaronix) and the space between the plates was filled with the iodide based electrolyte (Iodolyte AN-50, solarnix). External electrodes were coated with silver paste.

Morphology of the grown nanorod was measured by field emission scanning electron microscope (XL-30, Philips). To measure the amount of dye adsorbed on the surface of the nanorods, a dye-anchored photoanode was immersed into 1mM NaOH of ethanol/H<sub>2</sub>O (vol 50/50) solution for 2 hrs and desorbed dye in the solution was analyzed by UV/Vis spectrophotometer (Lambda 35, Perkin Elmer). Photoelectrochemical tests were carried out with the aid of a potentiostat (CHI 660, CH Instrument). Specifically, electrochemical impedance spectroscopy (EIS) was tested from 100kHz to 0.1Hz with 0.05V amplitude at open circuit voltage bias under simulated light exposure. Mott-Schottky measurement were performed using a three electrodes system, namely, photoanode (working electrode), Pt wire (counter electrode), and Ag/AgCl standard electrode (reference electrode). In Mott-Schottky measurement, the electrolyte was 0.1M NaCl aqueous solution, and a sinusoidal electric field with a frequency of 80Hz and an amplitude of 10mV.

Electron diffusion coefficient and lifetime were characterized by a stepped light-induced transient measurement of photocurrent and voltage (SLIM-PCV) method.

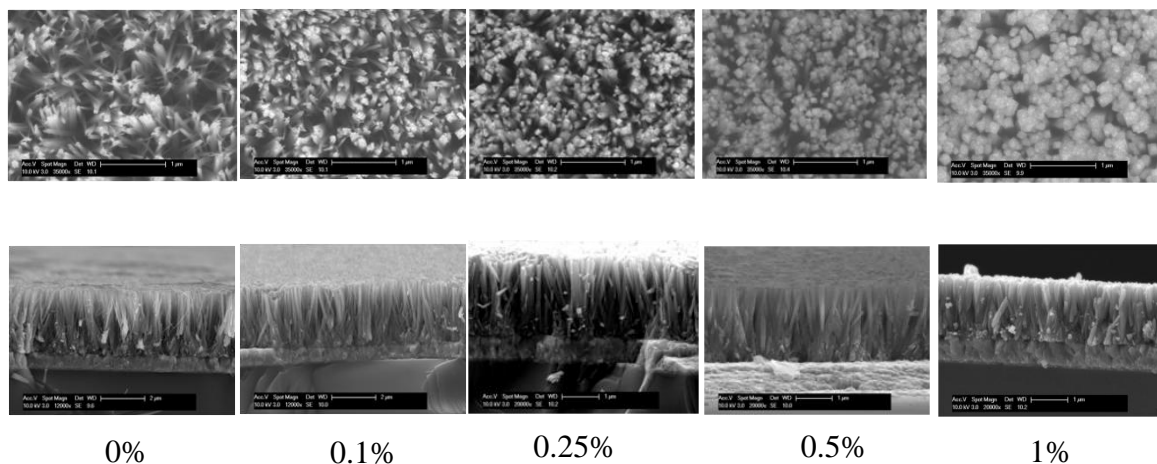


Conductivity of nanorod was measured by conductive-atomic force microscopy (c-AFM, Multiview-1000, Nanonics). To estimate work function of nanorods, a Pt wire probe and a boron-doped diamond probe were used. In c-AFM measurement, electric current was converted to voltage signal by a current amplifier (DLPCA-200, Femto). C-AFM measurement was firstly undertook with a raster scan with 2 $\mu$ m by 2 $\mu$ m at bias -4 V at probe tip with respect to substrate, and then current-voltage measurement was carried out from 0V to -5 V and 0V to +5 V with a scan rate of 0.03V/s (3ms as a step). For repeatable test, a script was made to control the bias from 0V to -5V, to 5 V, and to 0V for 6 cycles continuously. Several spots at different places have been measured and most of them gave rise to comparable results.

#### **4.2.2 Results and Analysis**

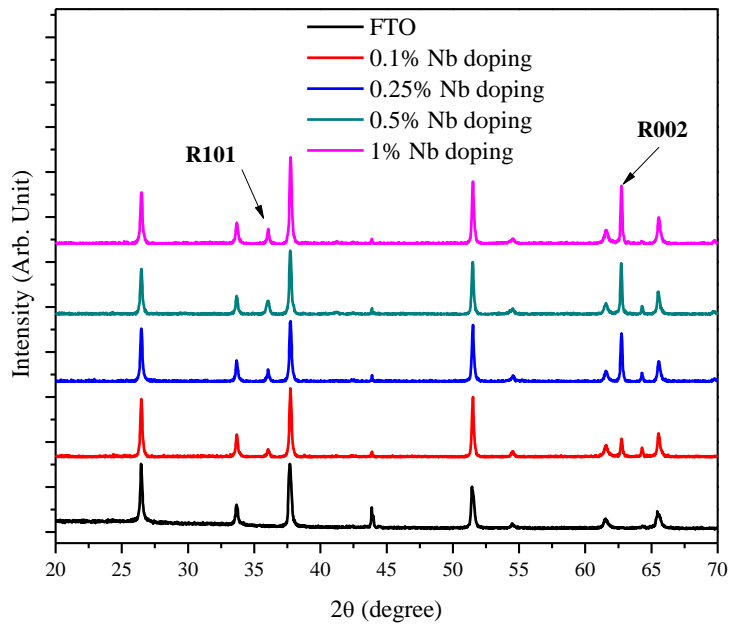
Figure 4-13 shows SEM micrographs of TiO<sub>2</sub> nanorods with different Nb content. Nb doping influences the size and density of the rutile nanorods. Specifically, an increase in the doping concentration widens the diameter of the nanorods; the diameter of the 0.5% Nb doped rutile nanorods was 100 nm which is 1.7 times larger than that of pure rutile nanorods. This increase in diameter tends to decrease the surface area of the nanorod arrays. On the other hand, a small amount of doping, such as 0.1% and 0.25%, not only increased the diameter of the nanorods, but also increased the density of the nanorods, as shown in the top view SEM images. With the smaller amount of doping, the increased width of the nanorods balances with the increased density of the nanorod so that the surface area of the nanorod arrays does not change significantly. In addition, an increase in the width of nanrods and a decrease in the open space

between the nanorods caused the vertical growth of Nb doped rutile nanorods. This factor may at least partially compensate for the loss of interface due to increases in nanorod width.



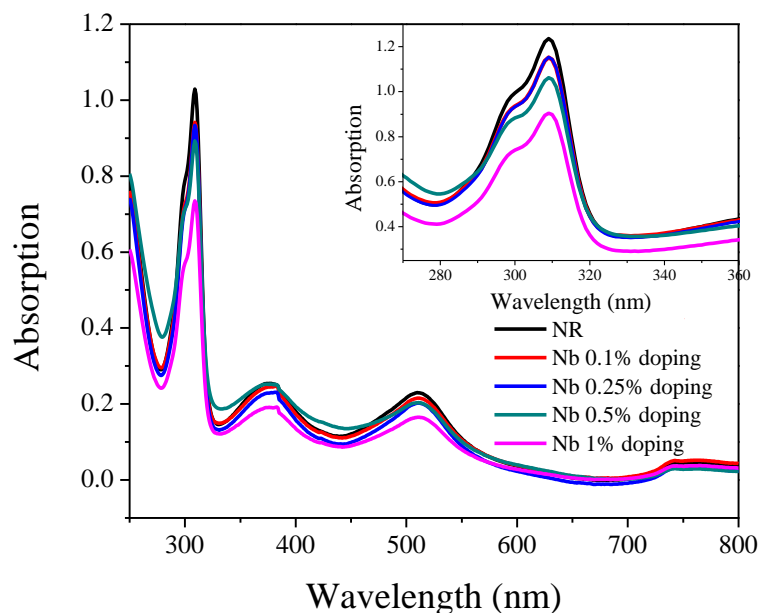
**Figure 4-13 SEM morphology evolution at different Nb doping level**

The effect of Nb doping on the width of rutile nanorods can be understood by looking into the growth mechanism of nanorods. It has been reported that the significance of chloride ions, which could be preferentially adsorbed on the surface of (110) and retard the growth along [110] direction.<sup>110,134</sup> This anisotropic adsorption of  $\text{Cl}^-$  ion could be affected by Nb doping since the energy of (110) face will be lowered after Nb doping.<sup>175</sup> Given that a driving force for the growth of the nanorods is the preferential adsorption of  $\text{Cl}^-$  ion onto (110) face of rutile, the decrease in the aspect ratio of the nanorods indicates that Nb decreases the difference in the surface energy between (110) plane and (001) plane. Nb doping lowers the surface energy of (110) face in rutile and suppresses the preferential adsorption of  $\text{Cl}^-$  ion, which result in higher growth rate along [110] direction and smaller aspect ratio in Nb doped nanorods.



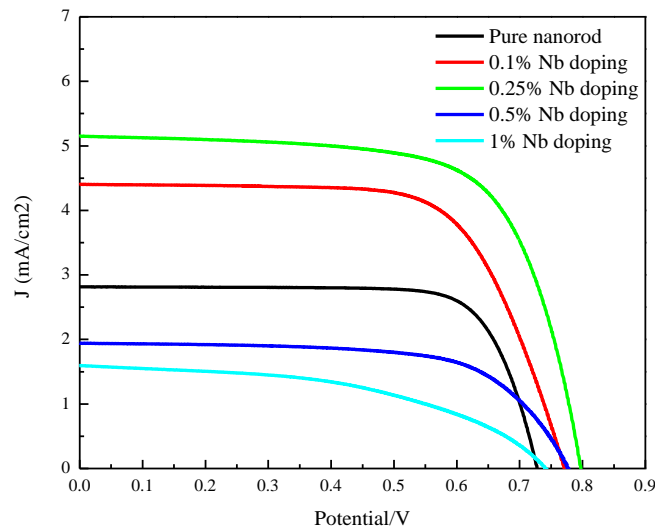
**Figure 4-14 XRD pattern of Nb doped samples, rutile phase without Nb precipitate**

Figure 4-14 shows the XRD pattern of Nb doped nanorod. Rutile (101) and (002) peak shows up among peaks from FTO substrate. Nb doped nanorod shows in rutile phase as pure nanorod, and there is no additional phase related to Nb doping. This result indicates the doping is quite effective without any macroscale aggregate. The ratio of (002) to (101) gets larger as Nb doping increases, and it can be interpreted through the change of morphology of nanorods after Nb doping. As discussed previously in morphology evolution in Figure 4-13, after Nb doping, nanorods will be much denser with larger nanorod width, and nanorods are more vertically aligned. The change of morphology will give rise to higher amount of crystalline plane (002), paralleling FTO substrate, and lower amount of (101) plane. Therefore, intensity of (002) peak gets stronger and (101) peak gets weaker as Nb doping increases.



**Figure 4-15 UV-Visible spectroscopy measurement of dye-desorption for pure and doped nanorod**

Changes in the morphology of nanorods also alter the surface area and porosity of the nanorod array film, which influences the anchoring of dye sensitizers. To evaluate the dye anchoring behavior, the dye on the surface nanorods was desorbed and analyzed as a function of the Nb doping concentration. The amount of the adsorbed dye continuously decreased as the doping concentration increased, as shown in inset of Figure 4-15. These results agree very well with the morphology change observed in SEM. As the doping concentration increased, the amount of the adsorbed dye correspondingly decreased. However, the change was not significant for the nanorods doped with a small amount of Nb. As Nb doping exceeds 0.5%, the drop of adsorbed dye became more obvious. The significant reduction of the adsorbed dye in 1% Nb doped rutile nanorods indicates that the surface area of the nanorod arrays is dramatically decreased.



**Figure 4-16 Current-voltage curves of Nb-doped nanorod**

J-V curves of DSSC made from the nanorods with different Nb concentration are shown in Figure 4-16. A length of the nanorod was about 2 $\mu$ m. The efficiency of the DSSCs using lightly doped nanorod (0.1% Nb) gains significant improvement, and short circuit current bumps to 4.4 mA/cm<sup>2</sup> from 2.7 mA/cm<sup>2</sup> in pure nanorod. In DSSCs of 0.25% Nb doped nanorods, both short circuit current and open circuit voltage were increased to 5.1 mA/cm<sup>2</sup> and 0.79 V, respectively. Compared with pure nanorods, 0.25% Nb doped nanorods increased the efficiency of DSSCs by 80%. This cannot be ascribed to the change in the morphology of Nb doped nanorods. In fact, the adverse effect of a smaller surface area on the photon-electron conversion manifested in the DSSCs built on 0.5 and 1% Nb doped rutile nanorods. In addition to the change of short circuit current after high Nb doping level (>0.5%), fill factor degrades as Nb doping increases, which may due to change of shunt resistance and/or increase of trapping probability of carriers.

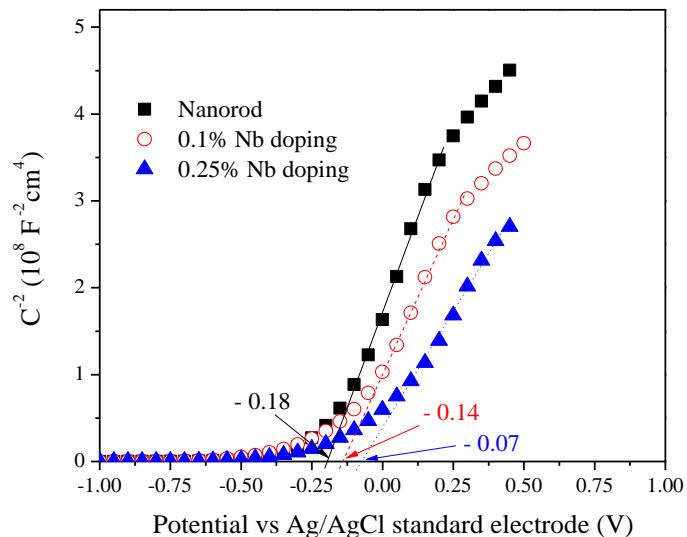


**Figure 4-17 Mott-Schottky Plot of pure and Nb doped nanorod, showing a positive shift of flat band**

If there is a change in the surface state of the nanorod, the open circuit voltage and the driving force for the carrier injection are modified. To examine the effect of Nb doping on the surface electrochemical properties of rutile nanorods, the flat band of Nb doped rutile nanorods were measured. A Mott-Schottky plot is shown in Figure 4-17. The slope of tangent line in a Mott-Schottky plot is proportional to  $1/N_D$ , where  $N_D$  is the number of donor. It is shown in that the slope of Nb doped nanorod decreases, indicating that Nb incorporation increases the carrier concentration of the nanorods. When 0.25% Nb was incorporated, the flat band of the rutile nanorods corresponding to the zero surface charge shifted from -0.18 V to -0.07 V. This positive shift of Nb doped rutile is consistent with prior study on Nb doped anatase particles<sup>151</sup>. Due to the surface charge of Nb doped nanorods, a energy difference between lowest unoccupied molecular orbital (LUMO) of dye sensitizer and Fermi energy level of  $TiO_2$  increases and electron injection between two levels is facilitated.<sup>171</sup> Therefore, the change of the flat band contributes to increasing the short circuit current. However, the positive shift of the flat band does not lead to a decrease in the open circuit voltage, which disagrees with the prediction of the

previous report<sup>151</sup>. This implies that Nb doping reduces the carrier recombination by modifying a carrier transport mechanism. This additional effect from lightly Nb doping should be explored further through other carrier transport measurements.

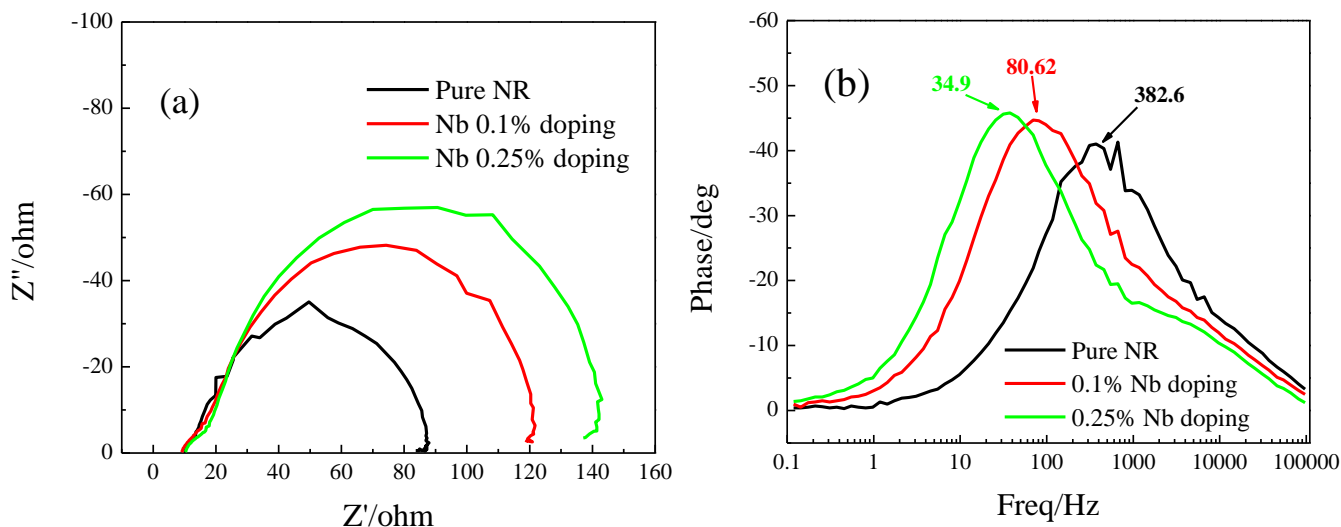


**Figure 4-18 Nyquist (a) and Bode Plot (b) of lightly doped nanorod, larger recombination resistance and longer lifetime after Nb doping**

To study the carrier transport mechanism, electrochemical impedance spectroscopy (EIS) analysis was carried out to measure the charge-transport process of DSSCs. An equivalent circuit model is commonly employed to simulate Nyquist plot as discussed the background section. Normally, there are three characteristic components in Nyquist plot: A semi-circle at a low frequency regime (large  $Z'$ ) comes from the capacitance and charge-transfer (recombination) between  $\text{TiO}_2$  and electrolyte; linear regime at medium frequency is responsible for the characteristics of transmission line model with transport resistance; a small semi-circle at high frequency represents the TCO/Pt/electrolyte interface or TCO/ $\text{TiO}_2$ /electrolyte.<sup>176</sup> The information of different component will be extracted by tuning applied DC bias, which will change the Fermi level. For example, recombination resistance and chemical capacitance

between  $\text{TiO}_2$  and electrolyte become dominant at the bias around open circuit voltage.<sup>123</sup> A radius of the semi-circle at the low frequency regime increases as Nb concentration increases, as shown in Figure 4-18 (a). This increased impedance can be interpreted as the enhancement of recombination resistance by Nb doping. Higher recombination resistance is expected to elongate carrier lifetime. In the bode plot, the frequency of the maximum phase is inversely proportional to the electron life time.<sup>177</sup> As shown Figure 4-18 (b), Nb doping shifts the resonance frequency to lower values, or longer life time. The improved life time demonstrated in EIS indicates the suppressed recombination especially at nanorod/electrolyte interfaces.

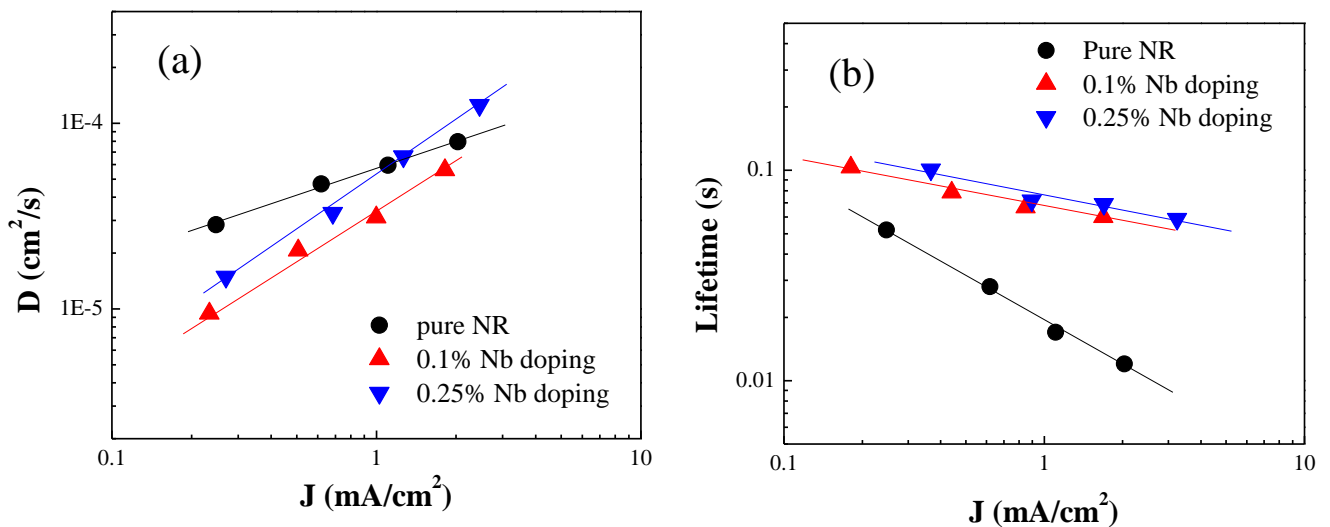


Figure 4-19 SLIM-PCV measurement, (a) diffusion coefficient, (b) lifetime

Photovoltage and photocurrent response under stepped light was measured to examine the change in the carrier transport and recombination by Nb doping in a more quantitative way with respect to different light flux conditions. Figure 4-19 (a) presents the carrier diffusion coefficient of pure and Nb doped nanorods. The diffusion coefficient of Nb doped nanorods is not much different from that of pure nanorods. However, the Nb doping clearly changes a slope



in the plot of the diffusion coefficient vs. short circuit current. In 0.1% and 0.25% Nb doped rutile nanorods its slope is 0.98 which is larger than 0.48 in pure nanorods. This implies that Nb doping modifies a dominant carrier trapping mechanism, which results in higher conductivity for Nb doped nanorod. It has been proposed that a high conductivity coming from small effective mass and high ionization efficiency of Nb is responsible for the improved transport.<sup>153,178</sup> Figure 4-19 (b) shows the lifetime of Nb doped samples. 0.1% and 0.25% doped nanorods exhibit a longer lifetime. As the short circuit current was increased (i.e. at higher incoming light intensity), the difference in the lifetimes of the Nb doped samples and pure sample increased. Specifically, at a short circuit current of  $2 \text{ mA/cm}^2$ , the lifetime of the Nb doped nanorods was 4 to 5 times larger than that of the pure nanorods. This improved lifetime is consistent with the results of EIS analysis, suggesting suppressed carrier recombination at the  $\text{TiO}_2$  – electrolyte interface and during transport.

The above measurements show that Nb doping changes the carrier injection at the dye -  $\text{TiO}_2$  interface and the carrier transport behavior through the nanorods. One more step we examined in the electron transport from the dye to the external electrode is the electron collection at the rutile nanorod - FTO interface. The approach we took is to measure the conductivity of nanorods locally using conductive-AFM. Figure 4-20 shows the morphology and current image of pure nanorods and 0.25% Nb-doped nanorods with a boron-doped diamond probe at a -4V bias. A large gain ratio of  $10^6 \text{ A/V}$  was used to accurately detect electric current. The morphology in AFM as shown in Figure 4-20 (a) and (c) is very close to SEM top-view, and Nb doped sample shows denser nanorod although width of nanorod is very similar. Electric current of the nanorods under electric bias is measured at nanoscale and electric current images are also

shown in Figure 4-20. Electric current signal images exhibit local fluctuation which is consistent with the nanorod distribution in AFM images.

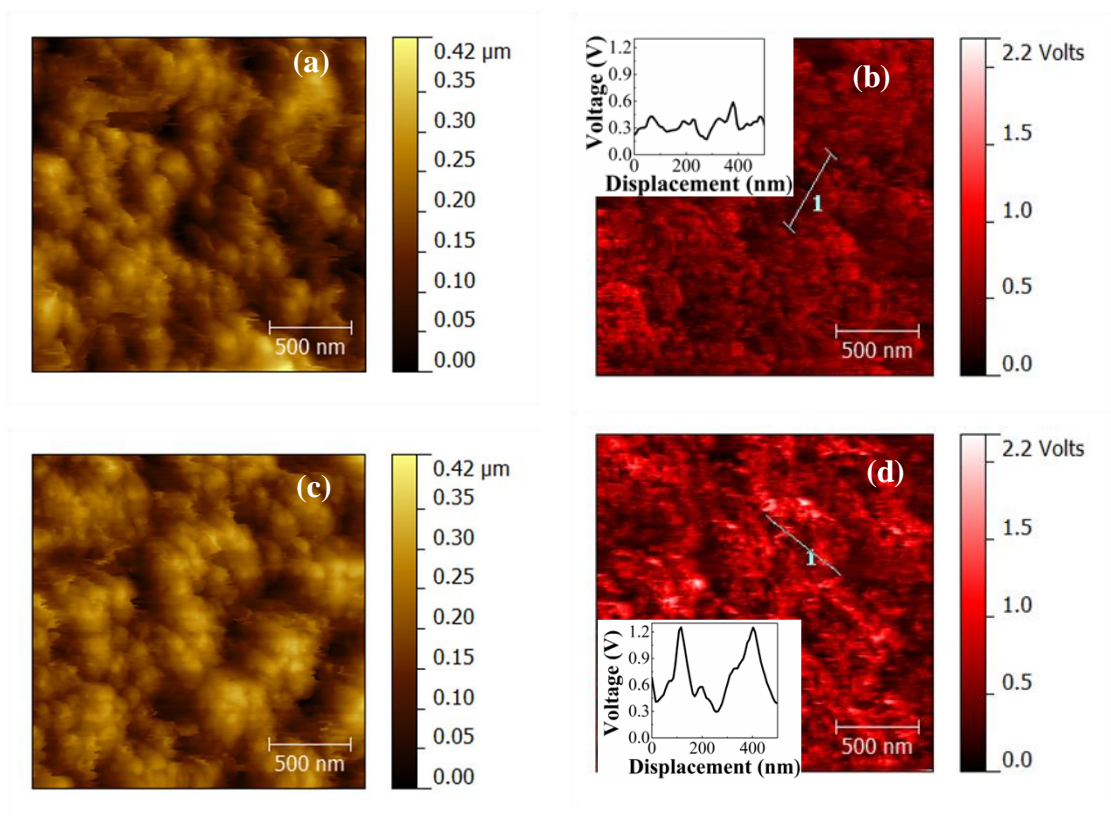


**Figure 4-20 C-AFM measurement of Nb doped nanorod on top of FTO using boron-doped diamond probe (a) morphology and (b) current of pure nanorod, (c) morphology and (d) current of 0.25% Nb doped nanorod, current profiles of marked areas are illustrated in the insets (current signal has been multiplied by - 1 so that larger the number indicates stronger current).**

A comparison of pure and Nb-doped rutile nanorods show a clear contrast in the electric current intensity. In general, current image of Nb-doped nanorod shows higher current, or is brighter. From the profiles of two typical peaks as shown in the insets of Figure 4-20 (b) and (d), current has been improved from 0.5V to 1.2V after Nb doping. These C-AFM results show that Nb-doping enhances electron transfer from nanorods to FTO at the same electric bias.

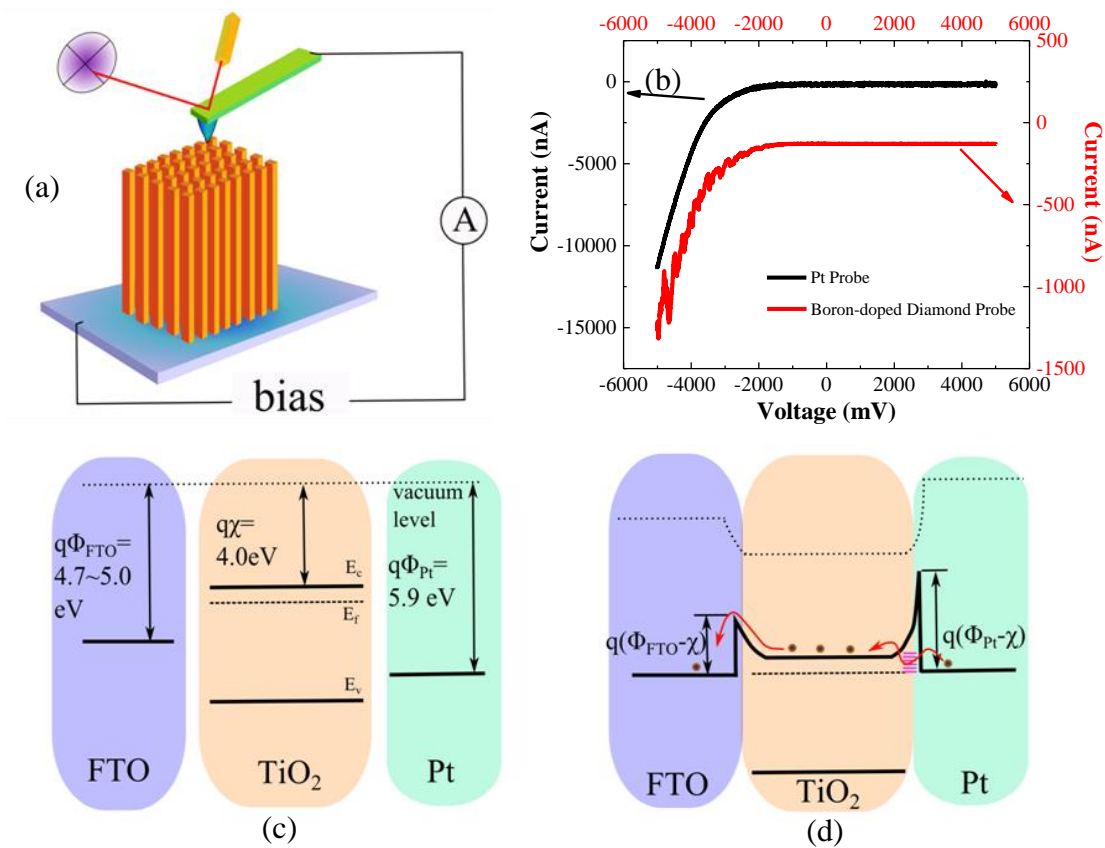


**Figure 4-21 C-AFM measurement of Nb doped nanorod on top of FTO, (a) schematics of measurement configuration; (b) I-V curve with Pt probe and Boron doped diamond probe; energy level alignment before contact (c) and after contact (d)**

A detailed carrier transport mechanism at the nanorod-FTO junction was found when the c-AFM measurement was performed using both a Pt probe and a boron-doped diamond probe. Electric current at negative bias is much stronger with Pt probe as shown in Figure 4-21. This difference may come from the different contact area of the probe since Pt wire probe is larger (~200nm) and more conductive. One interesting thing is that the current-voltage (I-V) curve is very similar on both the negative bias and the positive bias side. The work function of FTO has been reported to be 5.0 eV<sup>179</sup> if it is properly cleaned, and it is degenerated due to Fluorine doping<sup>180</sup>. The work function of Pt is around 5.9 eV, and work function of boron-doped diamond

is similar to Al<sup>161</sup>, which is 4.08 eV. Since rutile nanorod is a single crystal, its electronic property is anisotropic, and it is reported that work function is dependent on surface slightly (from 4.05 eV to 4.13eV).<sup>181</sup> In our case, we use work function of rutile as 4.0 eV as reported in previous study.<sup>182</sup> Therefore, the contact between conductive diamond and rutile is an Ohmic contact and Pt/rutile forms a Schottky barrier in theory. However, the similarity of I-V curve indicates that the FTO/rutile junction plays a main role and tip/rutile junction is almost negligible. The first question is why electron from Pt to rutile could be very easy? In ideal situation, the breakdown of rutile/Pt is very large since the barrier height is around 1.9 eV. The experimental result shows an abnormal breakdown. This abnormal breakdown may be due to the assistance of intraband states either surface state or defect level<sup>183</sup>. What is more, it has been reported that a fairly Ohmic contact would be formed relatively easily at Pt/rutile (001) junction.<sup>182</sup> As shown in Figure 4-21 (d), electrons will go through the Pt/rutile barrier via intraband states easily, and the transition voltage becomes lower than the breakdown voltage at this interface. The next question why FTO/nanorod will form a Schottky-like barrier? In the conventional nanoparticle based DSSC, barrier between FTO and particle is so narrow that it is possible to have electron tunneling.<sup>154</sup> In nanorod/nanowire case, 1D dimensional structure is relative large and it can be analogical to compact film, where Schottky barrier may take place.<sup>184</sup>

Since stronger current signal from Pt probe is much stronger and more stable comparing with boron doped diamond probe as shown in Figure 4-21 (b), the following quantitative I-V curve measurement of different doped nanorod is undertaken using Pt probe.

In this study, we found that the Schottky junction barrier at the FTO-TiO<sub>2</sub> interface can be nullified by doping Nb into TiO<sub>2</sub>. I-V curves of Nb-doped rutile nanorods are shown in Figure 4-22 (a). In this experiment, Nb doping significantly increased electric current in the nanorod grown on FTO. A few cycles has been tested as shown in Figure 4-22 (b), it implies that the I-V curve is very repeatable. The shape of I-V curve looks like a Schottky barrier diode, and it commonly could be interpreted by thermionic emission<sup>163</sup>. Considering series resistance in circuit, current and voltage can be described in Eqn. 4-7.

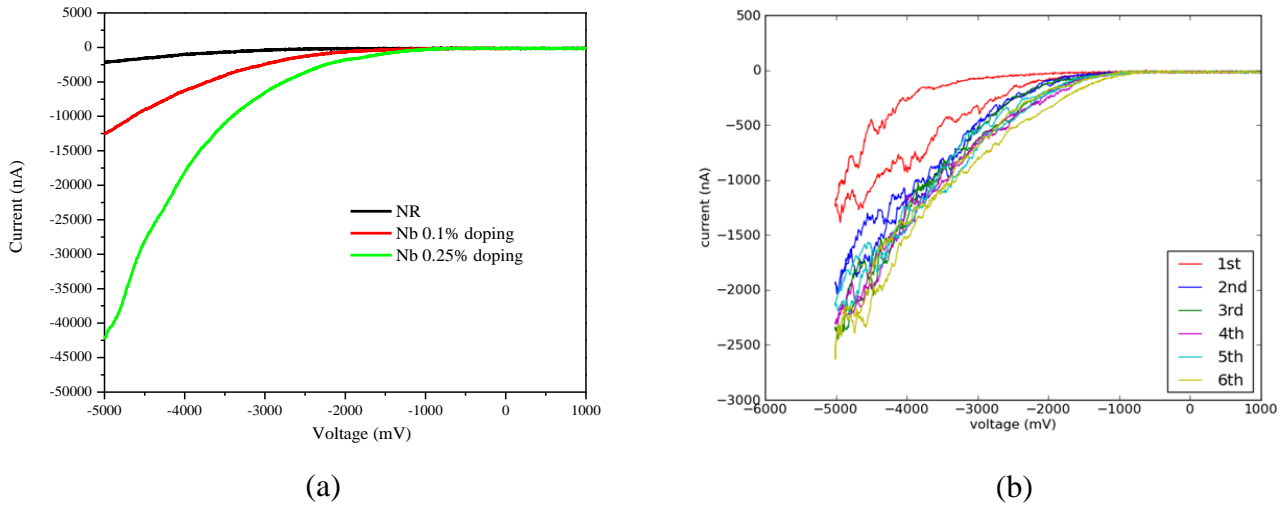


**Figure 4-22 I-V curve comparison of pure nanorod and Nb doped nanorod (a) and its repeatability test after 6 repeat cycles(b)**

Series resistances can be extracted through  $I dV/dI$  vs  $I$  plot as shown in Figure 4-23 (a). Pure nanorod in the Figure 4-23 (a) shows  $0.406 \text{ M}\Omega$  resistance. When Nb was doped, the series resistance dramatically decreased. The series resistance of the 0.1% Nb and 0.25% Nb doped rutile nanorods was  $0.082 \text{ M}\Omega$  and  $0.009 \text{ M}\Omega$ , respectively. This result attests to the high electric conductivity of Nb doped nanorods, which confirms the discussion above. Based on Eqn.4-7, we can replot  $I$  (in log scale) vs effective  $V$  (for convenience, current and voltage have been multiplied by -1 to get a conventional I-V curve) as shown in Figure 4-23 (b). Effective voltage is derived by subtracting series resistance component. A linear relation is obtained at higher voltage region. One interesting result is the onset voltage has been lowered dramatically with Nb doping. The decrease of the onset voltage indicates that electrons in the Nb doped rutile nanorods are more easily collected by FTO film.

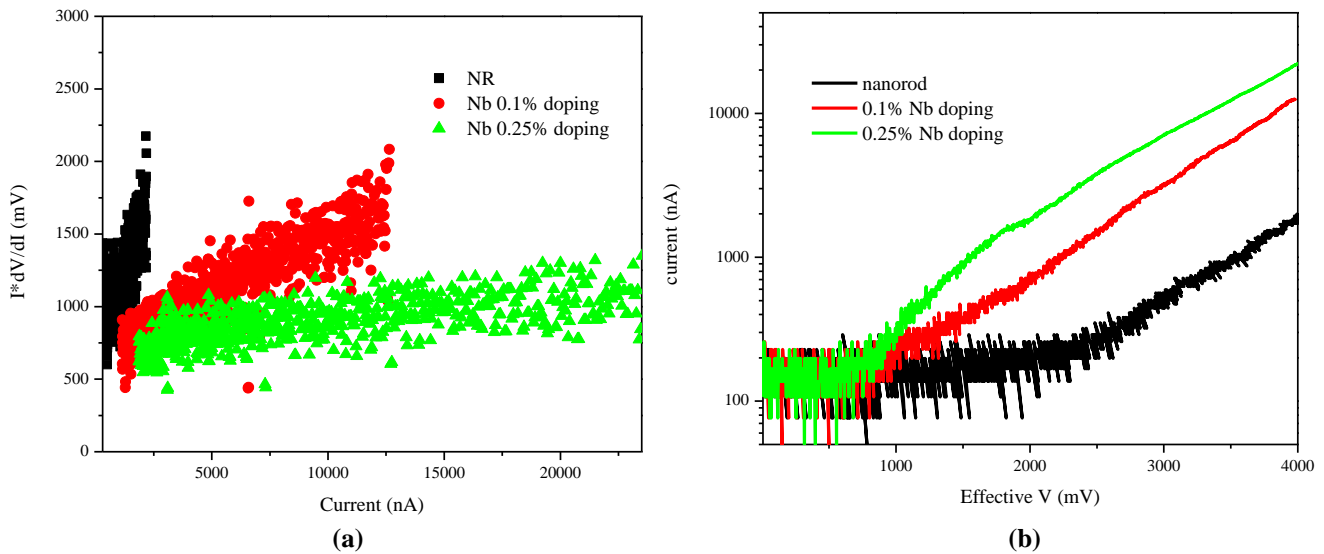


**Figure 4-23 Series resistance derivation (slope) of Nb doped nanorod (a) and I-V curve after subtracting series resistance (b)**

Another obvious difference in I-V curve for different Nb doped nanorods is the absolute value of the current and intercept of the linear line. The intercept of line represents  $I_s$ , which is supposed to be the same for pure nanorod and doped samples according to Eqn. 4-8. However, higher  $I_s$  value after doping has been observed in the results, which contradicts to thermoionic emission model. The deviation from thermionic model is more pronounced after higher Nb doping. Increased  $I_s$  shows lower barrier height after Nb doping, which is not true. The barrier height is the difference between work function of FTO and electron affinity of rutile, which is independent of doping in most cases. This discrepancy may be due to the occurrence of different transport path, such as thermionic field emission after doping. The barrier width ( $W_D$ ) is dependent on doping concentration ( $W_D$  is proportional to  $N_D^{-1/2}$ ), and  $W_D$  could get so narrow after doping that electron may tunnel through barrier with only a small amount of thermal energy which may be a fraction of original barrier height. This tunneling will make an easier electron transport.

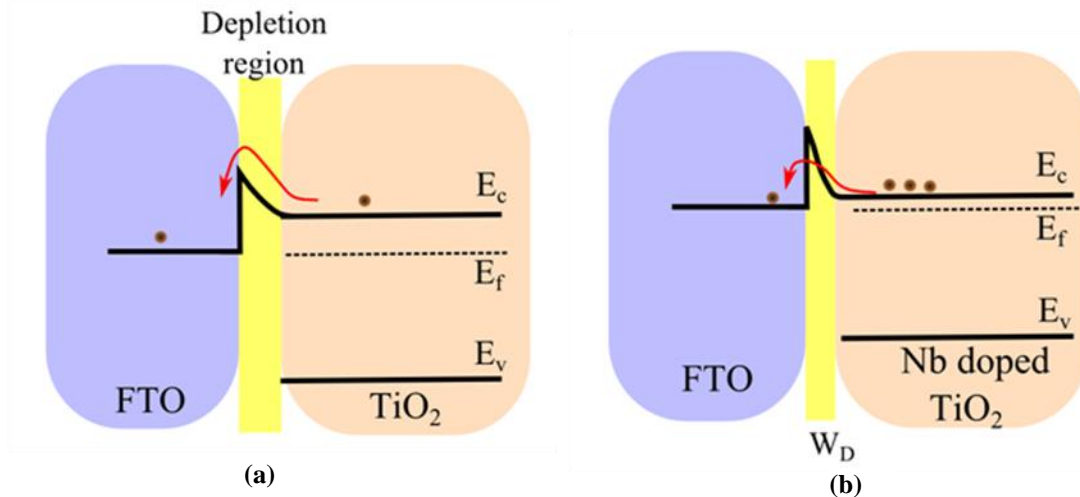


**Figure 4-24 Proposed charge transport model in FTO and nanorod contact, thermoionic emission (a) and thermoionic field emission after Nb doping (b)**

This thermionic-field emission could happen with intermediate doping range ( $10^{17} < N_D < 10^{19} \text{cm}^{-3}$ ), and 0.1% doping, which will be converted  $10^{19}$  per cubic centimeters doping level, falls to this category. Similar increased tunneling current after doping has been reported in NiSi/n-Si contacts.<sup>185</sup> The change of transport path after doping would affect the transport from nanorod to FTO as shown in Figure 4-24, and consequently, it will enhance the charge collection efficiency, which accounts for one reason of the improved efficiency with Nb doping.

#### **4.2.3 Charge transport observation in nanorod via c-AFM**

Advanced atomic force microscope (AFM) analyses such as photo-conductive AFM are effective approach to disclose subtle but critical information in nanoscale. These techniques have been exploited in revealing the charge transport behavior in bulk heterojunction (BHJ) organic solar cells<sup>161,186,187</sup>. Charge, surface potential of active layer, lateral and vertical distribution, and correlation between local information and device performance were carefully explored due to the nanoscale resolution of AFM. However, this advanced AFM technique has not been used in DSSC system partially because of liquid electrolyte. Hence, it would be exciting if advanced AFM research can be extended to DSSC systems.



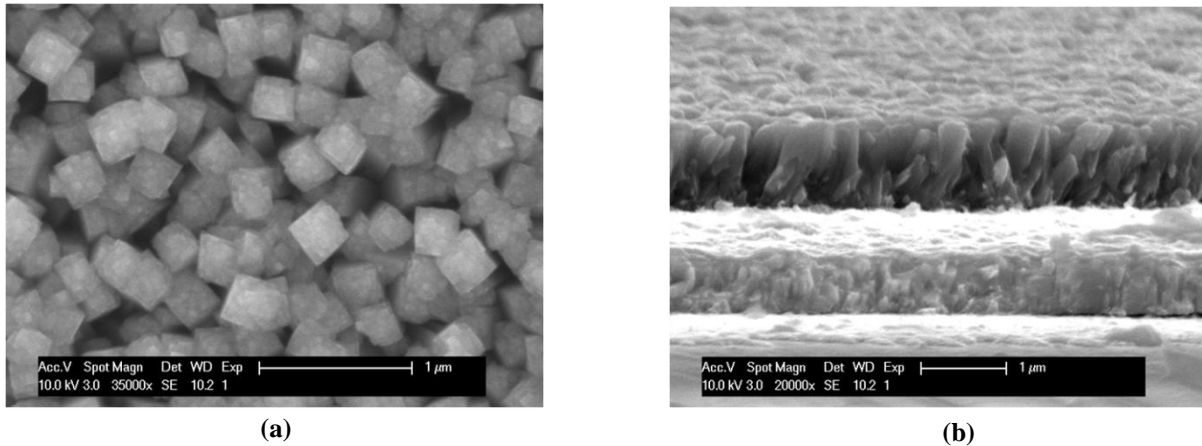


**Figure 4-25 SEM microgram of 2% Nb doped nanorods, (a) top view; (b) cross-section view.**

In order to capture detailed information, high resolution of mapping is necessary. The adopt of boron doped diamond could go down to sub 100 nm resolution, which is good but still exceed the desirable resolution for regular nanorod possessing the width of 80nm. Thanks to the morphology effect of Nb doping, it is possible to increase the width of nanorod in purpose by adding more loading of Nb doping. Figure 4-26 (a) and (b) shows the top view and cross-section view of 2% Nb doped nanorod. As shown in the top view, the width of individual nanorod has increased to scale of 300~400nm, which could be exploited with c-AFM relatively easily.

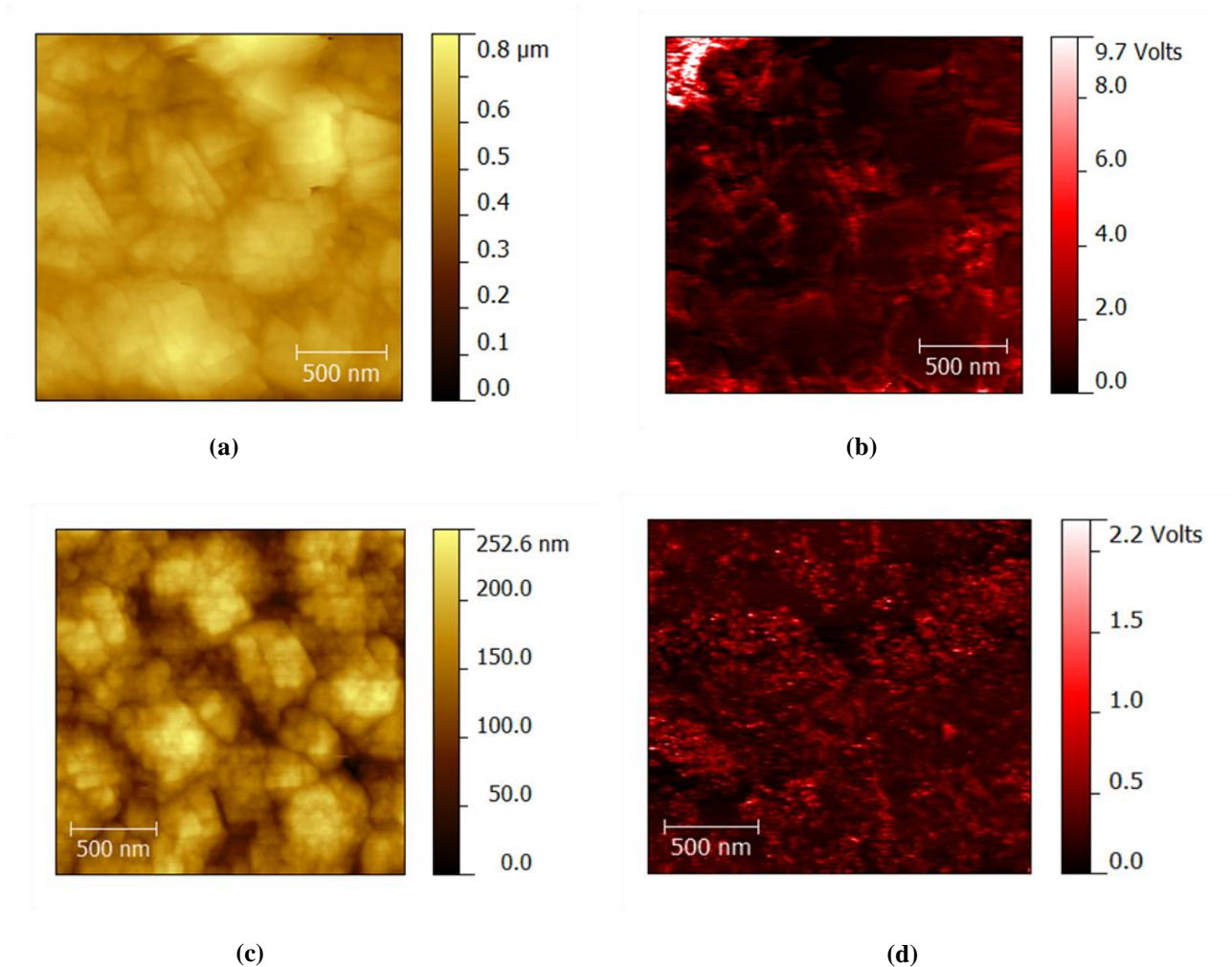


**Figure 4-26 C-AFM measurement of 2% Nb doped nanorod after annealing at air (a), (b),  $10^9$  gain; at forming gas (5%  $H_2$ ) (c), (d),  $10^6$  gain**

Figure 4-26 presents the c-AFM results of 2% Nb doped nanorods at different annealing atmospheres, air and forming gas respectively. The morphology has been changed slightly, and a gigantic change shows up at current maps. First of all, current has been a two or three order difference in air annealing and reducing atmosphere annealing. Such a dramatic change of conductivity at different annealing atmosphere may be related to the existence of defects, such as vacancies, in the nanorod. Another intriguing phenomenon was that the distribution of current path was totally different. As shown in Figure 4-26 (b), basic current shape was in rectangle, and

much stronger current is found at the edge of rectangles. For forming gas (5% H<sub>2</sub>) annealing, the current was more uniform, and much smaller current feature size, which was close to individual nanorod size (~30nm). Since TiCl<sub>4</sub> treated nanorod is annealed at air, the surface diffusion dominated observation could be served as a direct support to the proposed surface diffusion model proposed in Chap. 3. What is more, revolutionary change of current path pattern after forming gas annealing suggests a novel method to circumvent the surface diffusion limit, expected to have better performance.

### **4.3 NITROGEN DOPING IN NANOROD**

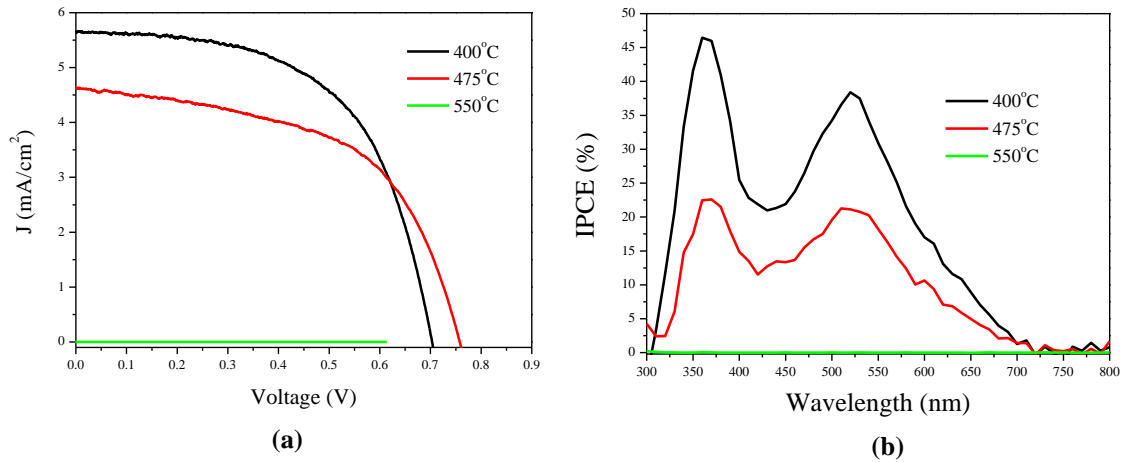
#### **4.3.1 Experiment**

Nanorod sample preparation on top FTO is same as the procedure used in section 4.2.1 without adding niobium. A typical nanorod length is around 2.8 $\mu$ m. Nitrogen doping was implemented through ammonia gas post-treatment. Specifically, NH<sub>3</sub> gas is continuously flowing into the tubing when it is heated to setup temperature. 400°C, 475°C, and 550°C have been explored for the optimum temperature, while other parameters, such as treatment time (2hrs), flow rate (500cc), are kept the constant.

After the N doping, nanorod was assembled to solar cell device as mentioned in the chapter 3. I-V curve and IPCE spectrum were measured to determine the performance of device and its underlying effect of N doping.

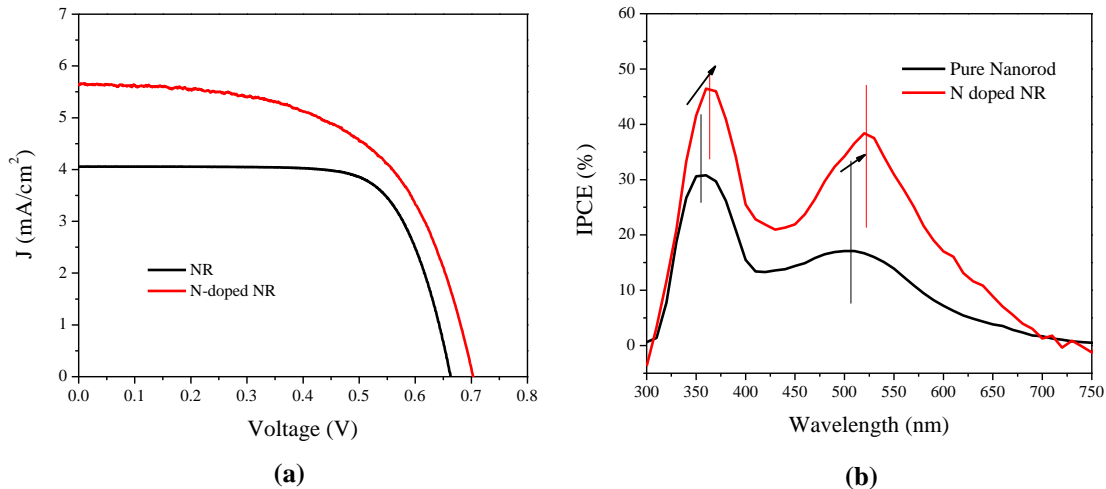
### 4.3.2 Results and Discussion

Figure 4-27 shows the relation between device performance and post-treatment temperature. At 400°C, device shows the highest short circuit current and the best overall conversion efficiency. As temperature is elevated to 475°C, open circuit voltage increases at the cost of decrease of short circuit current. When nanorod is treated at 550°C, short circuit current plunges to almost zero. IPCE gives similar trends in terms of performance after N doping. It has been reported that rutile crystal or anatase particles can sustain more than 600°C ammonia treatment without phase transformation.<sup>188,189</sup> The decrease of performance as the rising temperature may come from the deterioration of FTO substrate.



**Figure 4-27 Effect of temperature on DSSC performance after NH<sub>3</sub> post-treatment (a) I-V curve, (b)**

**IPCE**



**Figure 4-28 Comparison between NR and N-doped NR in I-V curve and IPCE, the enhancement comes from increased absorption of nanorod as well as efficient electron injection**

If we compare N doped sample and pure nanorod as shown in Figure 4-28, the enhancement of device performance is quite obvious. This enhancement is expected since N doped will have its synergetic effect. This postulation could be experimentally verified in IPCE diagram. It is interesting to realize that there are two peak-shifts in addition to the change of intensity after N doping. The first peak around 365nm is contributed from both dye sensitizer (N179 this case) and TiO<sub>2</sub>. The band gap narrowing of TiO<sub>2</sub> after N-doping would have a red shift. Another shift at around 535nm is very intriguing. N doping simply increases the dye adsorption, the change of IPCE around 535nm would only be the increase of IPCE value. However this red shift indicates the electron injection from dye has been facilitated. One of absorption peaks of N719 dye in acetonitrile solvent is around 540nm as shown in Figure 4-29. The N doping could make oxygen vacancies much easier to form inside the rutile as discussed in Chapter 2. The oxygen vacancies are located below conduction band, and their existence extends the conduction band edge to lower energy level to some degree. Electrons excited from N719

dye have a wide energy distribution as shown in absorption spectrum of N719, and only the electrons with a higher energy than  $\text{TiO}_2$  conduction band edge could be thermodynamically favored to inject into  $\text{TiO}_2$ . The lowering of band edge coming from N doping will result in more electron injections from dye sensitizers. This enhanced injection is responsible the second peak shift in IPCE measurement. In addition to the position shift, intensity of the second peak in Figure 4-28 (b) is also increased significantly, which manifests the enhanced electron injections. Both self-absorption and the enhanced electron injection contribute to the boost of short circuit current and overall efficiency. The drawback of N doping is the fill factor is worse compared to pure nanorods. The degradation may associated with introduced oxygen vacancies, which could act as trapping sites.

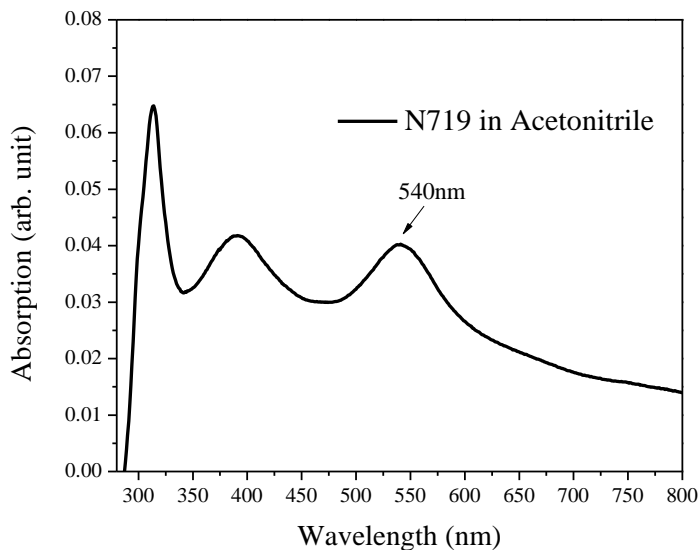


**Figure 4-29 Absorption spectrum of N719 in acetonitrile solvent**

## 5.0 CONCLUSIONS AND FUTURE WORK

### 5.1 CONCLUSIONS

The research topics discussed in this dissertation cover the application of TiO<sub>2</sub> in photocatalysis and photovoltaics. The underlying mechanism and performance by tuning the band gap and modifying morphology of TiO<sub>2</sub> were explored systematically, and their conclusions are summarized as following.

The approach of doping (N, Fe, and codoping) shows its effectiveness of band gap narrowing. The photocatalytical performance is examined using degradation of Rhodamine B, and a novel method, employing terephthalic acid fluorescence probe to monitor hydroxyl radicals, shows comparable results as the direct measurement. Doped N atoms reside the interstitial state of anatase particles, and presents superior performance under simulated solar light irradiation due to its band gap narrowing. For iron related doping (~ 3% nominal doping), photocatalysis performance is worse compared with pure nanoparticles despite its significant narrowing of bandgap. The low temperature (10 K) fluorescence spectra indicate that the considerable increase of the radiative recombination makes poor photocatalytic performance after Fe related doping.

Next, single crystalline nanorod has been synthesized directly on top of FTO substrate in order to tackle the slow transport issue in particle-based sensitized solar cell. The adoption of microwave reaction achieves a superb faster growth rate of nanorod compared to the methods

using conventional hydrothermal reaction. In addition, a thin layer of  $\text{TiO}_2$  seed is introduced to increase the nanorods density and decrease widths of nanorods at the same time, giving rise to a higher surface area. The carrier transport in rutile nanorod is compared to that in rutile nanoparticle. This controlled comparison indicates there is more than an order enhancement in terms of diffusion coefficient. The effect of  $\text{TiCl}_4$  surface treatment on carrier transport is also exploited systematically. It is found that diffusion coefficient is very sensitive to the surface treatment condition, while the lifetime keeps similar value. A surface diffusion model is proposed to interpret the observed experimental phenomena. This surface diffusion model may arise from the homogeneous contact between rutile particles and rutile nanorods.

The combination of the doping and nanorods is explored further. At 0.25% Nb doping, the overall efficiency of DSSCs composed of Nb doped nanorods increases close to 80% comparing to devices made of pristine nanorods. Further investigations show that both energy band alignment and transport behavior contribute to this significant enhancement. The positive shift of flatband facilitates the electron injection from dye sensitizer to conduction band of  $\text{TiO}_2$ , while less recombination makes a higher open-circuit voltage. Furthermore, the recombination is ascribed to both the nanorods/electrolyte interfaces and FTO/nanorods interfaces. Especially for FTO/nanorod, the results from c-AFM measurement imply that enhanced electron collection comes from the increased probability of tunneling after Nb doping. N doped nanorods are also showed increased short-circuit current because synergic effect of self-absorption and facilitated electron injection.

Lastly, the c-AFM technique is employed to heavily Nb doped nanorod (2% Nb doping) to observe the current transport path in nanorod. The preliminary results show the current path is not uniform when nanorods are annealed in air, which is a routine process for  $\text{TiCl}_4$  treatment.



The stronger current is from the edge of nanorods, which may be used as an evidence of the proposed surface diffusion model. What is more, the change of current transport under reducing atmosphere as observed in c-AFM, may shed a light on overcoming the limit of surface diffusion and make most use of nanorod architecture.

## 5.2 FUTURE WORK

Our investigation of carrier transport in surface coated nanorod shows surface diffusion in homogenous coated nanorod. The dominance of surface diffusion may come from two different factors. The first one is the abundance of surface state at surface of nanorod. Another one may be related to the homogeneous coating. The future work can be proposed in two directions: (1) disclose the origin of surface diffusion; (2) well engineering surface treatment to achieve high performance in nanorod based DSSC.

The first approach will employ the powerful tool of c-AFM as presented in Chap. 4. The c-AFM could provide unprecedented resolution to obtain detailed carrier transport path. In order to investigate the influence of surface state, different post-treatment will be carried out. For example, annealing atmosphere, oxygen plasma treatment, and addition of thin layer will be carefully investigated. Figure 5-1 shows the Raman spectrum of anatase thin layer on top of nanorod. Clearly, anatase phase thin film has been incorporated into the rutile nanorod. This heterojunction contact may change the carrier transport behavior. Any breakthrough in this fundamental research could lead to a jump to device performance in the future.

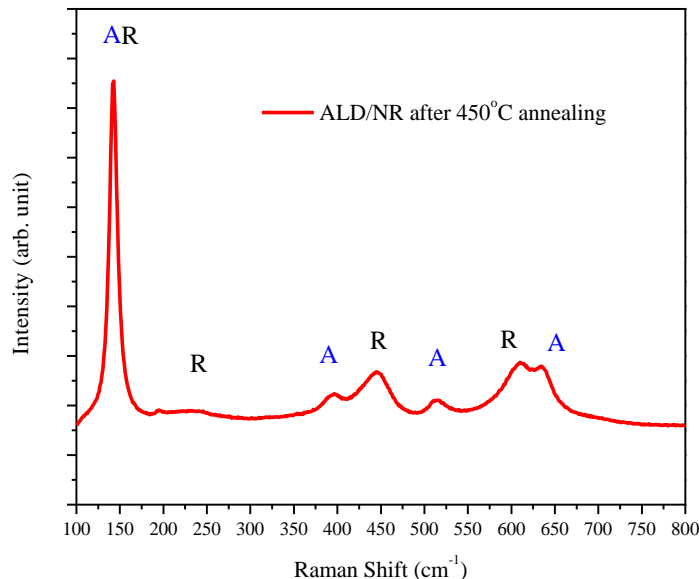


**Figure 5-1 Raman spectrum of anatase layer (~20nm) coated nanorod, and both rutile (marked in R) and anatase (marked in A) are observed**

Furthermore, high efficient DSSC based on nanorod will be explored. The strength of nanorod is its better transport behavior, stability, and good light scattering. The drawback for nanorod based DSSC is also very obvious: decrease of interface area. The key issue to obtain high efficiency is tackle light absorption through various approaches.

The first approach is to synthesize hierarchical structure without compromise of carrier transport strength. Engineered hierarchical structure could increase the surface area dramatically.  $\text{TiCl}_4$  treated nanorod has higher dye loading but results in dominance of surface diffusion. One potential candidate beyond  $\text{TiCl}_4$  treatment is anatase nanoparticle coated rutile nanorod. Recently, Lin et al have reported higher performance using hydrothermal treatment in nanotube.<sup>190</sup> The hydrothermal treatment uses the reaction of 0.01 M  $(\text{NH}_4)_2\text{TiF}_6$  aqueous solution in  $120^\circ\text{C}$  for 15-20min, generating anatase phase nanoparticles with further air

annealing. Their result shows higher efficiency compared with  $\text{TiCl}_4$  treatment method. This approach can be easily transferred to nanorod system because of its mild reaction condition.

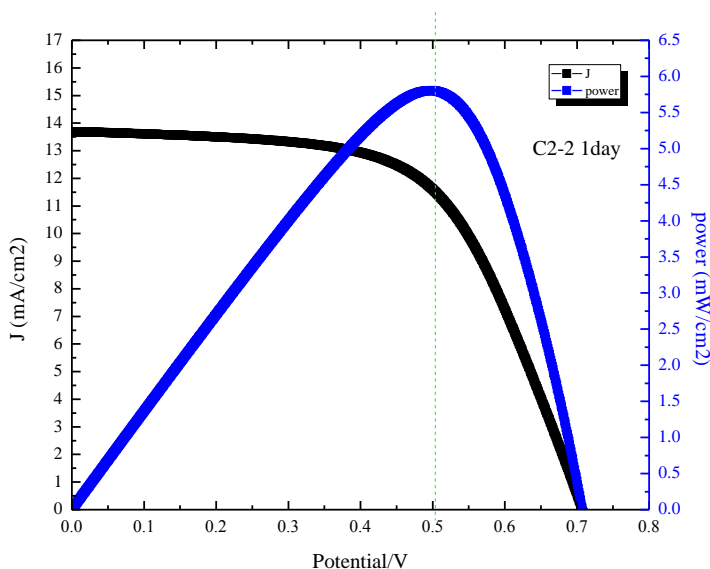


**Figure 5-2 J-V curve and export power diagram of pure nanorod (with  $\text{TiCl}_4$  treatment) based DSSC using high extinction dye C218**

Another approach to achieve high efficiency nanorod based DSSC is to utilize high extinction dye. The dye loading is relatively limited in nanorod structure compared with same thickness nanoparticle photoanode. This inefficiency could be made up by the introduction of high extinction dye, which has large extinction number implying stronger absorption of light. For example, C218 is one type of high extinction dye reported by Wang et al.<sup>191</sup> The maximum absorption coefficient of C218 is  $62.7 \times 10^3 \text{ M}^{-1} \text{ cm}^{-1}$  at 555nm. The simple combination of C218 with  $\text{TiCl}_4$  treated pure nanorod gives rise to  $13.6 \text{ mA/cm}^2$  short circuit current and 5.8% total conversion efficiency as shown in Figure 5-2.

Third approach to enhance performance is to manipulate light path in DSSC. Anti-reflection layer in front of FTO substrate, back-scattering layer right after the nanorod structure, and well

dispersed metal nanoparticles with strong plasmonic effect would potentially be integrated to nanorods based DSSC system. Light could go through FTO without a reflection loss, or be bounced back and forth, or trapped near surface of metals. In any case, the interaction between light and dye sensitizer would be enhanced so that the photocurrent is expected to be boosted.

What I have to emphasize is the above mentioned methods are stackable, which could generate a very appreciable enhancement in total. From the Nb doped nanorod, the road to harvest more solar light is just starting.

## BIBLIOGRAPHY

- (1) Kavan, L.; Gratzel, M.; Gilbert, S. E.; Klemenz, C.; Scheel, H. J. *J. Am. Chem. Soc.* **1996**, *118*, 6716.
- (2) Bokhimi, X.; Morales, A.; Aguilar, M.; Toledo-Antonio, J. A.; Pedraza, F. *Int. J. Hydrogen Energy* **2001**, *26*, 1279.
- (3) Jose, R.; Thavasi, V.; Ramakrishna, S. *J. Am. Ceram. Soc.* **2009**, *92*, 289.
- (4) Zheng, Y. Q.; Shi, E. R.; Chen, Z. Z.; Li, W. J.; Hu, X. F. *J. Mater. Chem.* **2001**, *11*, 1547.
- (5) Fujishima, A.; Honda, K. *Nature* **1972**, *238*, 37.
- (6) Litter, M. I. *Applied Catalysis B-Environmental* **1999**, *23*, 89.
- (7) Ni, M.; Leung, M. K. H.; Leung, D. Y. C.; Sumathy, K. *Renewable Sustainable Energy Rev.* **2007**, *11*, 401.
- (8) Wang, C. J.; Thompson, R. L.; Baltrus, J.; Matranga, C. *J. Phys. Chem. Lett.* **2010**, *1*, 48.
- (9) Osterloh, F. E.; Parkinson, B. A. *MRS Bull.* **2011**, *36*, 17.
- (10) Maeda, K.; Domen, K. *J. Phys. Chem. Lett.* **2010**, *1*, 2655.
- (11) Shockley, W.; Queisser, H. J. *J. Appl. Phys.* **1961**, *32*, 510.
- (12) Gratzel, M. *Nature* **2001**, *414*, 338.
- (13) Moser, J. *Chemical Monthly* **1887**, *8*, 373.
- (14) Namba, S.; Hishiki, Y. *J. Phys. Chem.* **1965**, *69*, 774.
- (15) Gerischer, H.; Tributsch, H. *Ber. Bunsenges. Phys. Chem.* **1968**, *72*, 437.
- (16) Hauffe, K.; Danzmann, H. J.; Pusch, H.; Range, J.; Volz, H. *J. Electrochem. Soc.* **1970**, *117*, 993.

- (17) Kalyanasundaram, K. *Solar Cells* **1985**, *15*, 93.
- (18) O'Regan, B.; Gratzel, M. *Nature* **1991**, *353*, 737.
- (19) Cahen, D.; Hodes, G.; Gratzel, M.; Guillemoles, J. F.; Riess, I. *J. Phys. Chem. B* **2000**, *104*, 2053.
- (20) Kong, F. T.; Dai, S. Y.; Wang, K. J. *Advances in OptoElectronics* **2007**, *2007*, 13.
- (21) Peter, L. M. *PCCP* **2007**, *9*, 2630.
- (22) Law, M.; Greene, L. E.; Johnson, J. C.; Saykally, R.; Yang, P. D. *Nat. Mater.* **2005**, *4*, 455.
- (23) Bisquert, J.; Mora-Sero, I. *J. Phys. Chem. Lett.* **2010**, *1*, 450.
- (24) Nakade, S.; Kanzaki, T.; Wada, Y.; Yanagida, S. *Langmuir* **2005**, *21*, 10803.
- (25) Halme, J.; Vahermaa, P.; Miettunen, K.; Lund, P. *Adv. Mater.* **2010**, *22*, E210.
- (26) Wei, D. *Int. J. Mol. Sci.* **2010**, *11*, 1103.
- (27) Gratzel, M. *Acc. Chem. Res.* **2009**, *42*, 1788.
- (28) Hagfeldt, A.; Boschloo, G.; Sun, L. C.; Kloo, L.; Pettersson, H. *Chem. Rev.* **2010**, *110*, 6595.
- (29) Green, M. A.; Emery, K.; Hishikawa, Y.; Warta, W. *Prog Photovoltaics* **2010**, *18*, 346.
- (30) Chiba, Y.; Islam, A.; Watanabe, Y.; Komiya, R.; Koide, N.; Han, L. *Jpn J Appl Phys* **2006**, *45*, L638.
- (31) Gratzel, M. *J Photoch Photobio A* **2004**, *164*, 3.
- (32) Nazeeruddin, M. K.; De Angelis, F.; Fantacci, S.; Selloni, A.; Viscardi, G.; Liska, P.; Ito, S.; Bessho, T.; Gratzel, M. *J. Am. Chem. Soc.* **2005**, *127*, 16835.
- (33) Gao, F.; Wang, Y.; Shi, D.; Zhang, J.; Wang, M. K.; Jing, X. Y.; Humphry-Baker, R.; Wang, P.; Zakeeruddin, S. M.; Gratzel, M. *J. Am. Chem. Soc.* **2008**, *130*, 10720.
- (34) Long, J. W.; Dunn, B.; Rolison, D. R.; White, H. S. *Chem. Rev.* **2004**, *104*, 4463.
- (35) Kavan, L.; Rathousky, J.; Gratzel, M.; Shklover, V.; Zupal, A. *Microporous Mesoporous Mater.* **2001**, *44*, 653.
- (36) Wagemaker, M.; Kentgens, A. P. M.; Mulder, F. M. *Nature* **2002**, *418*, 397.
- (37) Croce, F.; Appetecchi, G. B.; Persi, L.; Scrosati, B. *Nature* **1998**, *394*, 456.

- (38) Matsumoto, Y.; Murakami, M.; Shono, T.; Hasegawa, T.; Fukumura, T.; Kawasaki, M.; Ahmet, P.; Chikyow, T.; Koshihara, S.; Koinuma, H. *Science* **2001**, *291*, 854.
- (39) Ogale, S. B. *Adv. Mater.* **2010**, *22*, 3125.
- (40) Strukov, D. B.; Snider, G. S.; Stewart, D. R.; Williams, R. S. *Nature* **2008**, *453*, 80.
- (41) Gratzel, M. *Inorg. Chem.* **2005**, *44*, 6841.
- (42) Yu, K. H.; Chen, J. H. *Nanoscale Res. Lett.* **2009**, *4*, 1.
- (43) Capasso, F. *Science* **1987**, *235*, 172.
- (44) Smith, A. M.; Nie, S. M. *Acc. Chem. Res.* **2010**, *43*, 190.
- (45) Nah, Y. C.; Paramasivam, I.; Schmuki, P. *ChemPhysChem* **2010**, *11*, 2698.
- (46) Hurum, D. C.; Agrios, A. G.; Gray, K. A.; Rajh, T.; Thurnauer, M. C. *J. Phys. Chem. B* **2003**, *107*, 4545.
- (47) Spanhel, L.; Weller, H.; Henglein, A. *J. Am. Chem. Soc.* **1987**, *109*, 6632.
- (48) Wu, L.; Yu, J. C.; Fu, X. Z. *J. Mol. Catal. A: Chem.* **2006**, *244*, 25.
- (49) Choi, W.; Termin, A.; Hoffmann, M. R. *J. Phys. Chem.* **1994**, *98*, 13669.
- (50) Nagaveni, K.; Hegde, M. S.; Madras, G. *J. Phys. Chem. B* **2004**, *108*, 20204.
- (51) Anpo, M.; Takeuchi, M. *J. Catal.* **2003**, *216*, 505.
- (52) Zhu, J. F.; Deng, Z. G.; Chen, F.; Zhang, J. L.; Chen, H. J.; Anpo, M.; Huang, J. Z.; Zhang, L. Z. *Appl. Catal., B* **2006**, *62*, 329.
- (53) Tsai, C.-C.; Teng, H. *Appl. Surf. Sci.* **2008**, *254*, 4912.
- (54) Yang, Y.; Li, X. J.; Chen, J. T.; Wang, L. Y. *J. Photochem. Photobiol., A* **2004**, *163*, 517.
- (55) Zhu, J. F.; Zheng, W.; Bin, H. E.; Zhang, J. L.; Anpo, M. *J. Mol. Catal. A: Chem.* **2004**, *216*, 35.
- (56) Klosek, S.; Raftery, D. *J. Phys. Chem. B* **2001**, *105*, 2815.
- (57) Zhao, W.; Chen, C. C.; Li, X. Z.; Zhao, J. C.; Hidaka, H.; Serpone, N. *J. Phys. Chem. B* **2002**, *106*, 5022.
- (58) Kato, H.; Kudo, A. *J. Phys. Chem. B* **2002**, *106*, 5029.
- (59) Ranjit, K. T.; Willner, I.; Bossmann, S. H.; Braun, A. M. *Environ. Sci. Technol.* **2001**, *35*, 1544.

- (60) Asilturk, M.; Sayilkan, F.; Arpac, E. *J. Photochem. Photobiol., A* **2009**, *203*, 64.
- (61) Shah, S. I.; Li, W.; Huang, C. P.; Jung, O.; Ni, C. *PNAS* **2002**, *99*, 6482.
- (62) Asahi, R.; Morikawa, T.; Ohwaki, T.; Aoki, K.; Taga, Y. *Science* **2001**, *293*, 269.
- (63) Burda, C.; Lou, Y. B.; Chen, X. B.; Samia, A. C. S.; Stout, J.; Gole, J. L. *Nano Lett.* **2003**, *3*, 1049.
- (64) Gole, J. L.; Stout, J. D.; Burda, C.; Lou, Y. B.; Chen, X. B. *J. Phys. Chem. B* **2004**, *108*, 1230.
- (65) Sakthivel, S.; Kisch, H. *Angew. Chem. Int. Ed.* **2003**, *42*, 4908.
- (66) Ohno, T.; Mitsui, T.; Matsumura, M. *Chem. Lett.* **2003**, *32*, 364.
- (67) Yu, J. C.; Yu, J. G.; Ho, W. K.; Jiang, Z. T.; Zhang, L. Z. *Chem. Mater.* **2002**, *14*, 3808.
- (68) Zhou, J. K.; Lv, L.; Yu, J. Q.; Li, H. L.; Guo, P. Z.; Sun, H.; Zhao, X. S. *J. Phys. Chem. C* **2008**, *112*, 5316.
- (69) Luo, H. M.; Takata, T.; Lee, Y. G.; Zhao, J. F.; Domen, K.; Yan, Y. S. *Chem. Mater.* **2004**, *16*, 846.
- (70) Periyat, P.; McCormack, D. E.; Hinder, S. J.; Pillai, S. C. *J. Phys. Chem. C* **2009**, *113*, 3246.
- (71) Ozaki, H.; Iwamoto, S.; Inoue, M. *J. Phys. Chem. C* **2007**, *111*, 17061.
- (72) Rane, K. S.; Mhalsiker, R.; Yin, S.; Sato, T.; Cho, K.; Dunbar, E.; Biswas, P. *J. Solid State Chem.* **2006**, *179*, 3033.
- (73) Cong, Y.; Zhang, J. L.; Chen, F.; Anpo, M.; He, D. N. *J. Phys. Chem. C* **2007**, *111*, 10618.
- (74) Hao, H. Y.; Zhang, J. L. *Microporous Mesoporous Mater.* **2009**, *121*, 52.
- (75) Lakowicz, J. R. *Principles of Fluorescence Spectroscopy*; Springer, 2006.
- (76) Albani, J. R. *Principles and applications of fluorescence spectroscopy*; Wiley Online Library, 2007.
- (77) Watts, J. F.; Wolstenholme, J.; Wiley, J. *An introduction to surface analysis by XPS and AES*; Wiley Online Library, 2003.
- (78) Veal, B. W.; Paulikas, A. P. *Phys Rev B* **1985**, *31*, 5399.
- (79) Mason, T. J.; Lorimer, J. P.; Bates, D. M.; Zhao, Y. *Ultrason. Sonochem.* **1994**, *1*, S91.



- (80) Hirakawa, T.; Nosaka, Y. *Langmuir* **2002**, *18*, 3247.
- (81) Ohsaka, T.; Izumi, F.; Fujiki, Y. *J. Raman Spectrosc.* **1978**, *7*, 321.
- (82) Zhang, Z. B.; Wang, C. C.; Zakaria, R.; Ying, J. Y. *J. Phys. Chem. B* **1998**, *102*, 10871.
- (83) Fujishima, A.; Zhang, X. T.; Tryk, D. A. *Surf. Sci. Rep.* **2008**, *63*, 515.
- (84) Zhao, Z.; Liu, Q. *J. Phys. D: Appl. Phys.* **2008**, *41*.
- (85) Cronmeyer, D. C. *Phys. Rev.* **1959**, *113*, 1222.
- (86) Di Valentin, C.; Pacchioni, G.; Selloni, A.; Livraghi, S.; Giamello, E. *J. Phys. Chem. B* **2005**, *109*, 11414.
- (87) Saha, N. C.; Tompkins, H. G. *J. Appl. Phys.* **1992**, *72*, 3072.
- (88) Maeda, M.; Watanabe, T. *J. Electrochem. Soc.* **2006**, *153*, C186.
- (89) Torres, J.; Perry, C. C.; Bransfield, S. J.; Fairbrother, A. H. *J. Phys. Chem. B* **2003**, *107*, 5558.
- (90) Grafoute, M.; Petitjean, C.; Rousselot, C.; Pierson, J. F.; Greneche, J. M. *Scr. Mater.* **2007**, *56*, 153.
- (91) Yamashita, H.; Harada, M.; Misaka, J.; Takeuchi, M.; Ikeue, K.; Anpo, M. *J. Photochem. Photobiol., A* **2002**, *148*, 257.
- (92) Moser, J.; Grazel, M.; Gallay, R. *Helv. Chim. Acta* **1987**, *70*, 1596.
- (93) Mizushima, K.; Tanaka, M.; Iida, S. *J. Phys. Soc. Jpn.* **1972**, *32*, 1519.
- (94) Umebayashi, T.; Yamaki, T.; Itoh, H.; Asai, K. *J. Phys. Chem. Solids* **2002**, *63*, 1909.
- (95) Solbrand, A.; Lindstrom, H.; Rensmo, H.; Hagfeldt, A.; Lindquist, S. E.; Sodergren, S. *J. Phys. Chem. B* **1997**, *101*, 2514.
- (96) Yang, X. F.; Zhuang, J. L.; Li, X. Y.; Chen, D. H.; Ouyang, G. F.; Mao, Z. Q.; Han, Y. X.; He, Z. H.; Liang, C. L.; Wu, M. M.; Yu, J. C. *Acs Nano* **2009**, *3*, 1212.
- (97) Zhu, K.; Neale, N. R.; Miedaner, A.; Frank, A. J. *Nano Lett.* **2007**, *7*, 69.
- (98) Jiu, J. T.; Isoda, S.; Wang, F. M.; Adachi, M. *J. Phys. Chem. B* **2006**, *110*, 2087.
- (99) Kang, S. H.; Choi, S. H.; Kang, M. S.; Kim, J. Y.; Kim, H. S.; Hyeon, T.; Sung, Y. E. *Adv. Mater.* **2008**, *20*, 54.
- (100) Penn, R. L.; Banfield, J. F. *Geochim. Cosmochim. Acta* **1999**, *63*, 1549.

- (101) Adachi, M.; Murata, Y.; Takao, J.; Jiu, J. T.; Sakamoto, M.; Wang, F. M. *J. Am. Chem. Soc.* **2004**, *126*, 14943.
- (102) Enache-Pommer, E. Electron transport and recombination in nanowire dye-sensitized solar cells. 3396925, University of Minnesota, 2010.
- (103) Enache-Pommer, E.; Liu, B.; Aydil, E. S. *PCCP* **2009**, *11*, 9648.
- (104) Lee, J. C.; Kim, T. G.; Choi, H. J.; Sung, Y. M. *Cryst. Growth Des.* **2007**, *7*, 2588.
- (105) Xiang, B.; Zhang, Y.; Wang, Z.; Luo, X. H.; Zhu, Y. W.; Zhang, H. Z.; Yu, D. P. *J. Phys. D: Appl. Phys.* **2005**, *38*, 1152.
- (106) Wolcott, A.; Smith, W. A.; Kuykendall, T. R.; Zhao, Y. P.; Zhang, J. Z. *Small* **2009**, *5*, 104.
- (107) Lee, J. C.; Park, K. S.; Kim, T. G.; Choi, H. J.; Sung, Y. M. *Nanotechnol.* **2006**, *17*, 4317.
- (108) Lei, Y.; Zhang, L. D.; Meng, G. W.; Li, G. H.; Zhang, X. Y.; Liang, C. H.; Chen, W.; Wang, S. X. *Appl. Phys. Lett.* **2001**, *78*, 1125.
- (109) Feng, X. J.; Shankar, K.; Varghese, O. K.; Paulose, M.; Latempa, T. J.; Grimes, C. A. *Nano Lett.* **2008**, *8*, 3781.
- (110) Liu, B.; Aydil, E. S. *J. Am. Chem. Soc.* **2009**, *131*, 3985.
- (111) Komarneni, S.; Rajha, R. K.; Katsuki, H. *Mater. Chem. Phys.* **1999**, *61*, 50.
- (112) Wilson, G. J.; Will, G. D.; Frost, R. L.; Montgomery, S. A. *J. Mater. Chem.* **2002**, *12*, 1787.
- (113) Ding, K. L.; Miao, Z. J.; Liu, Z. M.; Zhang, Z. F.; Han, B. X.; An, G. M.; Miao, S. D.; Xie, Y. *J. Am. Chem. Soc.* **2007**, *129*, 6362.
- (114) Kopidakis, N.; Schiff, E. A.; Park, N. G.; van de Lagemaat, J.; Frank, A. J. *J. Phys. Chem. B* **2000**, *104*, 3930.
- (115) Dloczik, L.; Ileperuma, O.; Lauermann, I.; Peter, L. M.; Ponomarev, E. A.; Redmond, G.; Shaw, N. J.; Uhlendorf, I. *J. Phys. Chem. B* **1997**, *101*, 10281.
- (116) van de Lagemaat, J.; Frank, A. J. *J. Phys. Chem. B* **2000**, *104*, 4292.
- (117) Bisquert, J. *J. Phys. Chem. C* **2007**, *111*, 17163.
- (118) Bisquert, J. *PCCP* **2008**, *10*, 3175.
- (119) Zaban, A.; Greenshtein, M.; Bisquert, J. *ChemPhysChem* **2003**, *4*, 859.

- (120) Bisquert, J.; Zaban, A.; Greenshtein, M.; Mora-Sero, I. *J. Am. Chem. Soc.* **2004**, *126*, 13550.
- (121) Schlichthorl, G.; Park, N. G.; Frank, A. J. *J. Phys. Chem. B* **1999**, *103*, 782.
- (122) Liang, L. Y.; Dai, S. Y.; Hu, L. H.; Kong, F. T.; Xu, W. W.; Wang, K. J. *J. Phys. Chem. B* **2006**, *110*, 12404.
- (123) Fabregat-Santiago, F.; Garcia-Belmonte, G.; Bisquert, J.; Zaban, A.; Salvador, P. *J. Phys. Chem. B* **2002**, *106*, 334.
- (124) Liberatore, M.; Decker, F.; Burtone, L.; Zardetto, V.; Brown, T. M.; Reale, A.; Di Carlo, A. *J. Appl. Electrochem.* **2009**, *39*, 2291.
- (125) Nakade, S.; Kanzaki, T.; Kambe, S.; Wada, Y. J.; Yanagida, S. *Langmuir* **2005**, *21*, 11414.
- (126) Wagner, K.; Griffith, M. J.; James, M.; Mozer, A. J.; Wagner, P.; Triani, G.; Officer, D. L.; Wallace, G. G. *J. Phys. Chem. C* **2011**, *115*, 317.
- (127) Ahn, K. S.; Kang, M. S.; Lee, J. K.; Shin, B. C.; Lee, J. W. *Appl. Phys. Lett.* **2006**, *89*, 013103.
- (128) Ahn, K. S.; Kang, M. S.; Lee, J. W.; Kang, Y. S. *J. Appl. Phys.* **2007**, *101*.
- (129) Kang, M. S.; Ahn, K. S.; Lee, J. W.; Kang, Y. S. *J. Photochem. Photobiol., A* **2008**, *195*, 198.
- (130) Neale, N. R.; Kopidakis, N.; van de Lagemaat, J.; Gratzel, M.; Frank, A. J. *J. Phys. Chem. B* **2005**, *109*, 23183.
- (131) Tsoukleris, D. S.; Arabatzis, I. M.; Chatzivasilogioui, E.; Kontos, A. I.; Belessi, V.; Bernard, M. C.; Falaras, P. *Sol. Energy* **2005**, *79*, 422.
- (132) Thostenson, E. T.; Chou, T. W. *Compos. Part A-Appl. S.* **1999**, *30*, 1055.
- (133) Booske, J. H.; Cooper, R. F.; Freeman, S. A. *Mater. Res. Innovations* **1997**, *1*, 77.
- (134) Hosono, E.; Fujihara, S.; Kakiuchi, K.; Imai, H. *J. Am. Chem. Soc.* **2004**, *126*, 7790.
- (135) Huang, C. Y.; Hsu, Y. C.; Chen, J. G.; Suryanarayanan, V.; Lee, K. M.; Ho, K. C. *Sol. Energy Mater. Sol. Cells* **2006**, *90*, 2391.
- (136) Kang, M. G.; Ryu, K. S.; Chang, S. H.; Park, N. G.; Hong, J. S.; Kim, K. J. *Bull. Korean Chem. Soc.* **2004**, *25*, 742.
- (137) Wang, C. C.; Yu, C. Y.; Kei, C. C.; Lee, C. T.; Perng, T. P. *Nanotechnol.* **2009**, *20*, 285601.

- (138) Mor, G. K.; Shankar, K.; Paulose, M.; Varghese, O. K.; Grimes, C. A. *Nano Lett.* **2006**, *6*, 215.
- (139) Sommeling, P. M.; O'Regan, B. C.; Haswell, R. R.; Smit, H. J. P.; Bakker, N. J.; Smits, J. J. T.; Kroon, J. M.; van Roosmalen, J. A. M. *J. Phys. Chem. B* **2006**, *110*, 19191.
- (140) O'Regan, B. C.; Durrant, J. R.; Sommeling, P. M.; Bakker, N. J. *J. Phys. Chem. C* **2007**, *111*, 14001.
- (141) Nazeeruddin, M. K.; Kay, A.; Rodicio, I.; Humphry-Baker, R.; Mueller, E.; Liska, P.; Vlachopoulos, N.; Graetzel, M. *J. Am. Chem. Soc.* **1993**, *115*, 6382.
- (142) Kim, K. J.; Benkstein, K. D.; van de Lagemaat, J.; Frank, A. J. *Chem. Mater.* **2002**, *14*, 1042.
- (143) Hart, J. N.; Menzies, D.; Cheng, Y. B.; Simon, G. P.; Spiccia, L. *C.R. Chim.* **2006**, *9*, 622.
- (144) Charoensirithavorn, P.; Ogomi, Y.; Sagawa, T.; Hayase, S.; Yoshikawaa, S. *J. Electrochem. Soc.* **2010**, *157*, B354.
- (145) Hong, K. S.; Lee, S.; Cho, I. S.; Lee, D. K.; Kim, D. W.; Noh, T. H.; Kwak, C. H.; Park, S.; Lee, J. K.; Jung, H. S. *J Photoch Photobio A* **2010**, *213*, 129.
- (146) Ou, H.-H.; Lo, S.-L.; Liao, C.-H. *J. Phys. Chem. C* **2011**, *115*, 4000.
- (147) Baumard, J.; Tani, E. *J. Chem. Phys.* **1977**, *67*, 857.
- (148) Carotta, M. C.; Ferroni, M.; Gnani, D.; Guidi, V.; Merli, M.; Martinelli, G.; Casale, M. C.; Notaro, M. *Sensor Actuat B-Chem* **1999**, *58*, 310.
- (149) Furubayashi, Y.; Hitosugi, T.; Yamamoto, Y.; Inaba, K.; Kinoda, G.; Hirose, Y.; Shimada, T.; Hasegawa, T. *Appl. Phys. Lett.* **2005**, *86*, 252101.
- (150) Sharma, R. K.; Bhatnagar, M. C.; Sharma, G. L. *Sens. Actuators, B* **1998**, *46*, 194.
- (151) Lu, X. J.; Mou, X. L.; Wu, J. J.; Zhang, D. W.; Zhang, L. L.; Huang, F. Q.; Xu, F. F.; Huang, S. M. *Adv. Funct. Mater.* **2010**, *20*, 509.
- (152) Archana, P. S.; Jose, R.; Jin, T. M.; Vijila, C.; Yusoff, M. M.; Ramakrishna, S. *J. Am. Ceram. Soc.* **2010**, *93*, 4096.
- (153) Yang, M.; Kim, D.; Jha, H.; Lee, K.; Paul, J.; Schmuki, P. *Chem. Commun.* **2011**, *47*, 2032.
- (154) Ruhle, S.; Cahen, D. *J. Phys. Chem. B* **2004**, *108*, 17946.
- (155) Yoshida, Y.; Tokashiki, S.; Kubota, K.; Shiratuchi, R.; Yamaguchi, Y.; Kono, M.; Hayase, S. *Sol. Energy Mater. Sol. Cells* **2008**, *92*, 646.

- (156) Lee, S.; Noh, J. H.; Han, H. S.; Yim, D. K.; Kim, D. H.; Lee, J. K.; Kim, J. Y.; Jung, H. S.; Hong, K. S. *J. Phys. Chem. C* **2009**, *113*, 6878.
- (157) Kumar, A.; Madaria, A. R.; Zhou, C. W. *J. Phys. Chem. C* **2010**, *114*, 7787.
- (158) Huang, Q. L.; Zhou, G.; Fang, L.; Hu, L. P.; Wang, Z. S. *Energy Environ. Sci.* **2011**, *4*, 2145.
- (159) Yang, M. J.; Ding, B.; Lee, S.; Lee, J. K. *J. Phys. Chem. C* **2011**, *115*, 14534.
- (160) Coffey, D. C.; Reid, O. G.; Rodovsky, D. B.; Bartholomew, G. P.; Ginger, D. S. *Nano Lett.* **2007**, *7*, 738.
- (161) Hamadani, B. H.; Jung, S. Y.; Haney, P. M.; Richter, L. J.; Zhitenev, N. B. *Nano Lett.* **2010**, *10*, 1611.
- (162) Cheng, K.; Cheng, G.; Wang, S. J.; Li, L. S.; Dai, S. X.; Zhang, X. T.; Zou, B. S.; Du, Z. L. *New J. Phys.* **2007**, *9*.
- (163) Schroder, D. K. *Semiconductor material and device characterization*; Wiley-IEEE Press, 2006.
- (164) Neamen, D. A. *Semiconductor physics and devices: basic principles*, 2nd ed.; Irwin, 1997.
- (165) Sze, S.; Ng, K. K. *Physics of Semiconductor Devices*, third ed.; John Wiley & Sons: Hoboken, 2007.
- (166) Cheung, S. K.; Cheung, N. W. *Appl. Phys. Lett.* **1986**, *49*, 85.
- (167) Escher, J. S.; Berg, H. M.; Lewis, G. L.; Moyer, C. D.; Robertson, T. U.; Wey, H. A. *Electron Devices, IEEE Transactions on* **1982**, *29*, 1463.
- (168) *Dye-sensitized solar cells*; Kalyanasundaram, K., Ed.; EPFL Press, 2010.
- (169) Gelderman, K.; Lee, L.; Donne, S. W. *J. Chem. Educ.* **2007**, *84*, 685.
- (170) Fabregat-Santiago, F.; Garcia-Belmonte, G.; Bisquert, J.; Bogdanoff, P.; Zaban, A. *J. Electrochem. Soc.* **2003**, *150*, E293.
- (171) Liu, J.; Yang, H. T.; Tan, W. W.; Zhou, X. W.; Lin, Y. A. *Electrochim. Acta* **2010**, *56*, 396.
- (172) Oliva, F. Y.; Avalle, L. B.; Macagno, V. A.; De Pauli, C. P. *Biophys. Chem.* **2001**, *91*, 141.
- (173) Oliva, F. Y.; Avalle, L. B.; Santos, E.; Camara, O. R. *J Photoch Photobio A* **2002**, *146*, 175.

- (174) Jung, H. S.; Lee, J. K.; Lee, S.; Hong, K. S.; Shin, H. *J. Phys. Chem. C* **2008**, *112*, 8476.
- (175) Pang, Y.; Wynblatt, P. *J. Am. Ceram. Soc.* **2006**, *89*, 666.
- (176) Zhu, K.; Jang, S. R.; Frank, A. J. *J. Phys. Chem. Lett.* **2011**, *2*, 1070.
- (177) Lee, K. M.; Suryanarayanan, V.; Ho, K. C. *J. Power Sources* **2009**, *188*, 635.
- (178) Furubayashi, Y.; Yamada, N.; Hirose, Y.; Yamamoto, Y.; Otani, M.; Hitosugi, T.; Shimada, T.; Hasegawa, T. *J. Appl. Phys.* **2007**, *101*.
- (179) Helander, M. G.; Greiner, M. T.; Wang, Z. B.; Tang, W. M.; Lu, Z. H. *J Vac Sci Technol A* **2011**, *29*.
- (180) Levy, B.; Liu, W.; Gilbert, S. E. *J. Phys. Chem. B* **1997**, *101*, 1810.
- (181) Imanishi, A.; Tsuji, E.; Nakato, Y. *J. Phys. Chem. C* **2007**, *111*, 2128.
- (182) Hope, G. A.; Bard, A. J. *J. Phys. Chem.* **1983**, *87*, 1979.
- (183) Hensel, J.; Wang, G. M.; Li, Y.; Zhang, J. Z. *Nano Lett.* **2010**, *10*, 478.
- (184) Ruhle, S.; Dittrich, T. *J. Phys. Chem. B* **2005**, *109*, 9522.
- (185) Chan, J.; Martinez, N. Y.; Fitzgerald, J. J. D.; Walker, A. V.; Chapman, R. A.; Riley, D.; Jain, A.; Hinkle, C. L.; Vogel, E. M. *Appl. Phys. Lett.* **2011**, *99*.
- (186) Coffey, D. C.; Ginger, D. S. *Nat. Mater.* **2006**, *5*, 735.
- (187) Pingree, L. S. C.; Reid, O. G.; Ginger, D. S. *Nano Lett.* **2009**, *9*, 2946.
- (188) Diwald, O.; Thompson, T. L.; Zubkov, T.; Goralski, E. G.; Walck, S. D.; Yates, J. T. *J. Phys. Chem. B* **2004**, *108*, 6004.
- (189) Chen, H.; Nambu, A.; Wen, W.; Graciani, J.; Zhong, Z.; Hanson, J. C.; Fujita, E.; Rodriguez, J. A. *J. Phys. Chem. C* **2007**, *111*, 1366.
- (190) Ye, M. D.; Xin, X. K.; Lin, C. J.; Lin, Z. Q. *Nano Lett.* **2011**, *11*, 3214.
- (191) Li, R. Z.; Liu, J. Y.; Cai, N.; Zhang, M.; Wang, P. *J. Phys. Chem. B* **2010**, *114*, 4461.